

Integration of Patient-specific Myocardial Perfusion in CT-based FFR Computations

Ernest Lo

Dissertation Submitted in Fulfilment of the
Requirements for the Degree of
Doctor of Philosophy

in the
Department of Medical Physics and Biomedical Engineering
University College London

June 7th, 2021

Declaration

I, Ernest Lo, confirm that the work presented in this thesis is my own.
Where information has been derived from other sources, I confirm that this
had been indicated in the thesis.

Acknowledgements

I would like to express my gratitude to my academic supervisor Dr. Ryo Torii for his guidance and insights throughout this project. His patience and encouragement have allowed me to develop fully in my academic life. I would also like to thank my clinical supervisor Dr. Leon Menezes for his clinical expertise and continued support of my studies, providing the necessary clinical perspective to keep my work grounded in clinical application. I would like to thank Raymond Endozo and Dr. Francesca Pugliese for supporting my work and providing crucial clinical data and advice. I would also like to thank the EPSRC and the UCL CDT in Medical Imaging for funding this project and providing the necessary multidisciplinary environment for my studies to flourish. Lastly, I want to thank my family for their undying support and love.

Abstract

Computed Tomography based Fractional Flow Reserve (FFRCT) is a non-invasive simulation based measure for diagnosing ischaemia causing arterial stenoses. One drawback of simulation based measures are the assumptions made that are usually based on population studies that may not apply to all patients.

This study describes the fundamental characteristics to FFRCT simulations and how the simulations can be simplified where it can and where assumptions break down. The investigation starts with assessing whether the simulations can be simplified to a steady flow, whilst uncharacteristic of typical coronary blood flow, it was demonstrated that with regards to the diagnostic measures of FFR, and its variants dFFR or iFR, that steady flow was applicable, which reduces the complexity of the simulation, saving computational time and resources as well as removing uncertainty in the input assumptions.[1]

The next phase of the study explored the downstream conditions of the FFRCT simulation scheme. The microvasculature is too small to resolve in CT imaging and therefore assumptions are made regarding its form and function. Whilst form function relationships of the microvasculature are well established in the literature for the structure of microvessels at rest, assumptions regarding stress or hyperaemia are used for FFRCT to simulate maximal blood flow through the coronary arteries. The investigation utilised perfusion imaging to assess the validity of this assumption and showed how variable the microvascular response to hyperaemia is, and the effect that has on FFRCT.[2][3]

The last part of the study produced a novel method of estimating the microvascular response using patient metrics such as age, sex, diabetes, smoker status etc, from a training dataset of 101 patients. By using the patient-specific microvascular response, FFRCT simulations better represent the coronary artery health of the patient. On a separate dataset of 10 patients, the FFRCT measurements using this novel method was also

validated against the gold standard invasive FFR and has demonstrated a better diagnostic performance (94% accuracy) than the conventional method (82% accuracy). Secondly the novel method also created a probabilistic spread of FFRCT values that may provide better utility than a strict binary measure. Whilst this novel method will require further validation with larger studies, it nevertheless has potential to address some of the current drawbacks of FFRCT methods when applied to a varied patient demographic.

Impact Statement

Coronary artery disease (CAD) is the number one cause of premature death globally. As imaging modalities improve over time, minimally invasive and non-invasive diagnostic measures are becoming ever more popular in diagnosing the severity of suspected CAD. Fractional flow reserve, the ratio of pressures proximal and distal to a stenosis, has been demonstrated to be an effective indicator of the physiological severity of a stenotic (constricted) artery, and currently is the gold standard for functional diagnosis of CAD. Standard FFR is measured invasively using a pressure wire with the patient under induced hyperaemia. As imaging technologies improve, the medical community has been increasingly drawn to non-invasive alternatives such as Computed Tomography FFR (FFRCT), which uses CT angiography and computational fluid dynamics to simulate flow conditions such that FFR can be calculated directly. This popularity has coincided with the widespread adoption of CT coronary angiography as the first line test for CAD. However, conventional FFRCT protocols make strong assumptions based upon morphological predictions, many of which are based on population-wide studies which may not be suited to individual patients.

This study tackled assumptions, especially those related to outflow boundary conditions in computational fluid dynamic modelling (CFD), by developing a contrasting FFRCT model that uses perfusion imaging data from PET perfusion and CT Perfusion to compliment the simulation parameters as well providing validation of downstream flow conditions. Sensitivity of the predicted FFR values to the outflow boundary conditions (BC) was first examined using a novel outflow BC based on PET images. Then, using patient demographic statistics of 101 patients, a novel FFRCT method was developed and validated using a sample of 10 patients with invasive FFR to produce an FFRCT measure that more accurately represents the functional severity of a patient's stenosis. Ultimately the goal is to produce an FFRCT system that is more reliable and representative for all patients.

The importance of the accurately characterising the microvascular response has clinical ramifications, if incorrectly estimated, it can overestimate the severity of a coronary artery stenosis, leading to unnecessary procedures that serve little patient benefit. In particular, patient demographics such as women, the elderly, smokers, and diabetics tend not to be suited to the conventional assumptions.

On the engineering and computational modelling side, various simulation and physical assumptions were tested and validated, demonstrating that coronary blood flow simulations can in some aspects be simplified for specific purposes such as FFRCT. These findings will further demonstrate the possibility of devising computationally fast and reduced order models for FFRCT and similar simulations.

Publications

- Lo EW, Menezes LJ, Torii R. On outflow boundary conditions for CT-based computation of FFR: Examination using PET images. *Med Eng Phys.* 2020 Feb;76:79-87. doi: 10.1016/j.medengphy.2019.10.007. Epub 2019 Dec 20. PMID: 31866119.
- Lo EWC, Menezes LJ, Torii R. Impact of Inflow Boundary Conditions on the Calculation of CT-Based FFR. *Fluids.* 2019; 4(2):60. <https://doi.org/10.3390/fluids4020060>

Presentations

- Lo E, Menezes LJ, Torii R. (2018) 'Use of PET-based boundary conditions in coronary artery blood flow computations to estimate clinically important hemodynamic indicators' , 8th World Congress of Biomechanics 2018, Dublin (Oral presentation)
- Lo E, Menezes LJ, Torii R. (2018) "Integrating PET into the computation of CT-FFR" VPH-CaSE Conference 2018, London (Oral presentation)
- Lo E, Menezes LJ, Torii R. (2018) "Integrating PET into the computation of CT-FFR" SCCT London 2018 Winter Meeting, London (Poster presentation)
- Lo E, Kolossvary M, Patel K, Drobni Z, Kitslaar P, Reiber J, Menezes L, Pugliese F, Westwood M, Tarnoki AD, Karady J, Voros S, Merkely B, Bourantas CV, Torii R, Maurovich-Horvat P. (2017) "Genetics or Environment - The First Twin Study of Coronary Endothelial Shear Stress", AHA Circulation 2017 (Oral presentation presented by collaborator)

Contents

Declaration	2
Acknowledgements	3
Abstract	4
Impact Statement	6
Publications	8
Chapter 1. Introduction.....	24
1.1. Problem overview	24
1.2. Aims and objectives	26
1.3. Thesis structure	27
Chapter 2. Background.....	28
2.1. Clinical background	28
2.1.1. Heart anatomy	28
2.1.2. Coronary Microvascular Disease	30
2.1.3. Hyperaemia	30
2.2. CAD diagnosis and care	32
2.2.1. Typical care pathway.....	32
2.2.2. Invasive Coronary Angiography (ICA).....	34
2.2.3. CT Coronary Angiography (CTCA).....	35
2.2.4. CTCA Limitations	36
2.2.5. Alternative CTCA techniques.....	36
2.2.6. Percutaneous coronary intervention (PCI) and treatment guidance.....	37
2.2.7. Comparing various diagnostic measures	38
2.3. Functional measures of severity	40
2.3.1. Fractional flow reserve (FFR).....	40
2.3.2. Invasive FFR	42
2.3.3. FFR derived from Coronary Angiography (FFR-Angio)	43
2.3.4. Coronary Flow Reserve (CFR)	43
2.3.5. Index of Microvascular Resistance (IMR)	44
2.3.6. Instantaneous wave-free ratio (IFR).....	44
2.3.7. Discordance between functional measures	45
2.3.8. Hyperaemia	46
2.3.9. PET perfusion imaging.....	47
2.3.10. CFD based FFRCT	48
2.3.11. Abnormal Resistance in Atherosclerotic Coronary Arteries.....	49
Chapter 3. General Methodology	51

3.1.	Aim	51
3.2.	Theoretical framework.....	51
3.2.1.	Coronary Artery system	51
3.2.2.	Electrical circuit analogy.....	51
3.3.	Computational Fluid Dynamics Simulations.....	55
3.3.1.	Navier Stokes equation	55
3.3.2.	Solution to NS equations.....	55
3.3.3.	Boundary conditions	57
3.4.	Lumped parameter models.....	57
3.4.1.	Murrays Law	58
3.4.2.	Structured tree model.....	59
3.4.3.	Windkessel model	61
3.4.4.	Blood properties.....	62
3.5.	Anatomic reconstruction of Coronary Arteries.....	63
3.5.1.	Mesh sensitivity test.....	70
3.6.	Olufsen model implementation	71
3.6.1.	Structured tree model implementation.....	71
3.6.2.	Resistance calculation.	72
3.7.	Concluding Remarks.....	73
Chapter 4.	Examining the Effect of Inflow Conditions in Computational Fluid Dynamics simulation for FFRCT Computations.....	74
4.1.	Aim	74
4.2.	Introduction	74
4.2.1.	Pulsatile flow vs Steady flow	75
4.2.2.	Patient specific input variables	76
4.3.	Methods	77
4.3.1.	Patients.....	79
4.3.2.	Image Segmentation and Meshing	79
4.3.3.	Patient Specific Inflow Boundary Conditions.....	79
4.3.4.	Coronary Outflow Boundary Condition.....	80
4.3.5.	Aortic Outflow Boundary Condition.....	82
4.3.6.	Modelling the Effect of Adenosine.....	83
4.3.7.	Modelling Intramyocardial Pressure	83
4.3.8.	Computational Schemes and Parameters.....	84
4.3.9.	FFR quantification position and interpretation.....	85
4.3.10.	Instantaneous Wave-Free Ratio measurement	86

4.3.11.	Comparison of Patient-Specific Parameters and Population Average-Based Inflow Parameters	87
4.4.	Results	89
4.5.	Discussion	94
4.5.1.	Effect of Flow Pulsatility on FFR	94
4.5.2.	Importance of Patient Specificity in Inflow Parameters	95
4.5.3.	Various Definitions of Flow Reserve Parameters	97
4.5.4.	Limitations and Further Work	98
4.5.5.	Concluding Remarks	99
Chapter 5.	The variability of FFRCT due to outflow boundary conditions and assumptions	100
5.1.	Aim	100
5.2.	Introduction	100
5.3.	Methods	102
5.3.1.	Patients	102
5.3.2.	82-Rb PET Perfusion and flow reserve	102
5.3.3.	PET/CT registration	105
5.3.4.	Variability quantification of PET-CT registration	108
5.3.5.	PET-based perfusion sampling for PET model implementation	109
5.3.6.	Inflow boundary conditions	114
5.3.7.	Implementation of outflow boundary conditions	114
5.3.8.	Vasodilatory response model with structured tree	115
5.3.9.	Computational methods	116
5.3.10.	Examination of results to investigate the effect of outflow BC	116
5.4.	Results	118
5.4.1.	Perfusion based boundary conditions versus conventional boundary conditions	118
5.4.2.	Multi-vessel disease case	124
5.5.	Discussion	125
5.5.1.	FFR analysis	125
5.5.2.	PET Perfusion and coronary flow reserve comparison to verify the computed FFR values	128
5.5.3.	Resting Pd/Pa and CT-based iFR comparison	131
5.5.4.	Final comments	131
5.6.	Limitations	132
5.6.1.	82-Rb PET and PET perfusion cut-offs	133
5.7.	Summary	134

Chapter 6.	Optimising accuracy of FFRCT without the use of perfusion-based imaging methods	135
6.1.	Introduction	135
6.1.1.	Purpose.....	135
6.1.2.	Difference between CFR and response to hyperaemia in outlet boundary conditions.....	137
6.1.3.	CT Perfusion	138
6.2.	Method.....	138
6.2.1.	Patient dataset	138
6.2.2.	Perfusion estimation from CT perfusion	140
6.2.3.	Inflow conditions.....	141
6.2.4.	Outflow conditions.....	142
6.2.5.	Outflow BC with response to hyperaemia based on general population average (conventional FFRCT assumption).....	143
6.2.6.	Outflow BC with adjusted response to hyperaemia based on patient-specific CT perfusion imaging – target branch:.....	144
6.2.7.	Outflow BC with adjusted response to hyperaemia based on patient-specific CT perfusion imaging – regional.....	145
6.2.8.	Outflow BC with adjusted response to hyperaemia based on patient-specific CT perfusion imaging – global	146
6.2.9.	Outflow BC with adjusted response to hyperaemia based on patient population average	148
6.2.10.	Outflow BC with adjusted response to hyperaemia based on patient-specific demographic metrics	149
6.2.11.	Patient specific flow response and patient metrics.....	150
6.2.12.	Age.....	152
6.2.13.	Sex	153
6.2.14.	Diabetes.....	153
6.2.15.	Smoking	154
6.2.16.	Other metrics	155
6.2.17.	Patient specific estimate for hyperaemic flow response formula	156
6.3.	Results	159
6.3.1.	Response to hyperaemia population estimates.....	168
6.3.2.	Efficacy of demographically derived perfusion model of FFR prediction ..	171
6.3.3.	Effect of uncertainty in flow response estimate based on demographic parameters.....	172
6.3.4.	Quantitative accuracy of the FFRCT calculation.....	175
6.3.5.	CT-based computational prediction of iFR (CT-iFR)	176

6.3.6.	Development of probabilistic model.....	176
6.3.7.	Relationship between hyperaemia and FFR.....	177
6.4.	Concluding remarks.....	178
6.5.	Limitations.....	179
6.5.1.	Anatomical model reconstruction.....	179
6.5.2.	CFR measurement for CT perfusion dataset	180
6.5.3.	Patient metrics	180
6.5.4.	Implementation of new scheme	180
Chapter 7.	Conclusions.....	182
7.1.	Limitations.....	184
7.2.	Future work and recommendations	185

Figures

Figure 1-1 Diagram showing a pressure wire measuring the pressure proximal P_a and pressure distal P_d to the obstruction. Note that this pressure wire is inserted using a catheter with the patient under the effects of adenosine induced hyperaemia. FFR is the ratio of P_d and P_a [7]. 25

Figure 2-1 Anatomical diagram of the human heart displaying the coronary arteries and major blood vessels. Of particular importance is the Right Coronary Artery (RCA), Left Anterior Descending (LAD) and Left Circumflex (LCX) which wraps around the back of the heart. Diagram from [8]..... 29

Figure 2-2 Typical diagnostic and care pathway for patients with suspected angina (chest pain). This diagram is from the NICE guidelines 2017 for patients presenting with chest pain [11]..... 33

Figure 2-3 An example of a coronary angiogram obtained under Invasive Coronary Angiography (ICA). Image from [18]..... 34

Figure 2-4 Diagram of stenting procedure, taken from [35]..... 38

Figure 2-5 The regions of interest in the coronary artery tree that each functional measure can be used to determine the relative "health" of. Diagram from [53] 46

Figure 3-1 Electrical analogue model diagram of a simplified coronary artery system using Simulink. The values P_a and P_d are defined as the proximal coronary pressure and distal coronary pressure, shown in Figure 1-1..... 52

Figure 3-2 (Top) Simulated "pressure" proximal (P_a) and distal (P_d) using electrical analogue model. (Bottom) The relationship between FFR and response to hyperaemia, see equation 7..... 54

Figure 3-3 Diagram from Olufsen et al[93] showing a structured tree diagram of a root vessel of unit radius, and the radii of subsequent branches..... 59

Figure 3-4 2-element Windkessel model in electrical terms. $I(t)$ represent the current, $P(t)$ is the potential difference across the two points, C is the capacitance and R is the electrical resistance. 62

Figure 3-5 (Top Panel) 3D rendering of the segmented Chest CT images, the rib and spine are shown in a bone colour whilst the heart and blood vessels are shown in red. (Bottom Panel) Ribcage and Spine removed leaving just the heart and its blood vessels, e.g aorta, vena cava, pulmonary artery and veins etc. 65

Figure 3-6 User interface of ScanIP software, used in Step 1 of anatomical model reconstruction..... 66

Figure 3-7 (Top) The Aorta and coronary arteries connected to the myocardial cavity. The myocardium is not visible as its HU is outside the range that is being filtered here. (Bottom) Coronary artery segmented from the myocardium..... 67

Figure 3-8 Segmented aortic root and coronary arteries with boundaries defined for CFD simulations 68

Figure 3-9 (Top) Example of a completed mesh. (Bottom) Completed mesh zoomed in and oriented to view the cross section of the coronary artery opening. Note the prism layers at the edge..... 69

Figure 3-10 A comparison of pressure differences across the same stenotic artery, at different mesh sizes..... 70

Figure 4-1 Workflow of computational procedure to calculate FFR..... 78

Figure 4-2 Red line indicates the aortic flow rate across the cardiac cycle, derived from the changing volume of the left ventricular cavity contracting and relaxing across the cardiac cycle, shown by the green line..... 80

Figure 4-3 Schematic showing various outlet boundary conditions. All the boundary conditions are two-element Windkessel models represented in the circuit diagram. In this patient, both the left anterior descending artery (LAD) and left circumflex artery (LCx) supply the left ventricle, which is susceptible to higher levels of intramyocardial pressure. A pressure term is applied to the boundary condition to mimic the contraction of the left ventricle causing the embedded coronary arteries to be compressed and reduced flow[106]. RCA, right coronary artery. 81

Figure 4-4 FFR values measured across various distances from the locus of the stenoses..... 85

Figure 4-5 Pressure waveform of a patient under induced hyperaemia, showing the pressure at the coronary ostium (P_a) and pressure distal to an obstruction (P_d) across the cardiac cycle. Fractional flow reserve (FFR) is measured as the lowest ratio P_d/P_a measured. Note that there is a region in diastole known as the wave-free region, where the gradient of both pressure and flow are aligned and peripheral resistance is minimized. This is when the pressure drop is usually the most prominent across an obstruction. Instantaneous wave-free ratio (iFR) is measured in that region if the patient is at rest[122]...... 87

Figure 4-6 Pressure profile of patient 2 with an obstruction in the LAD. At 0.8 FFR, this patient is in the borderline area where stenting is only marginally better than optimal medical therapy. This pressure profile is obtained from the steady inflow simulation..... 90

Figure 4-7 Pressure profile of the same patient as Figure 4-6 for a pulsatile flow simulation. The stenosis is located on the LAD. In the time history of pressure, result from the last 3 cycles is shown..... 90

Figure 4-8 Flow rates of the various coronary branches across the cardiac cycle. In the left coronary arteries, flow is the highest during diastole due to high intramyocardial pressure during systole inhibiting flow. Note that there is a stenosis in LAD of this patient. The highlighted region (Blue) shows the diastolic wave-free region, where flow and pressure decline together [55,123]..... 91

Figure 5-1 Example of Siemens Syngo software outputs that accompanies Siemens PET/CT scanners (image courtesy of UCLH). The bullseye plots show the estimated blood flow based on tracer uptake of each myocardial region. The program requires minimal manual segmentation by the operator to identify the approximate shape of the myocardium. The table on the bottom left shows the stress and rest flow (though perfusion and flow here are used interchangeably, as the value is divided per unit tissue mass), and the ratio, the flow reserve for each macro-region supplied by each major coronary artery: LAD, LCX, RCA..... 104

Figure 5-2 A pair of CT (left) and PET (right) images of the patient's chest. The coordinates shown indicate the pixels of the images..... 107

Figure 5-3 PET image is resized, and five corresponding points on each image are identified by the user. An ICP algorithm manipulates the images through translation and rotation so that they are fully aligned. The example is a transversal image across the chest cavity, and the same process is followed for the sagittal plane to get the co-registration done in 3D..... 107

Figure 5-4 An example of a co-registered transverse slice of CT (left) and PET (right)..... 107

Figure 5-5 An example of a co-registered sagittal slice of CT (left) and PET (right)..... 108

Figure 5-6 Example of a composite PET/CT image of Subject 3. Transverse slice of the heart (left). Sagittal slice of the heart (right)..... 108

Figure 5-7 Diagram showing a good placement of the PET perfusion measurement sphere. The coronary artery mesh is terminated right next to its

contact point with the myocardium. By projecting the sphere forwards, it can easily quantify the perfusion supplied by this branch..... 110

Figure 5-8 Diagram showing the problem with an early terminated mesh, where the coronary artery branch ends far away from the myocardium. The PET measurement sphere will just average the portion of that sphere that is within the myocardium ignoring the space outside the myocardium. While that will work, it is still recommend placing the sampling sphere closer to the myocardium as it is more representative of the coronary flow. 111

Figure 5-9 Diagram showing an obviously early terminated mesh. Because the coronary artery points away from the myocardium, it is easily identifiable by eye, when looking at the mesh, that the PET values measured within the sphere is meaningless. The PET sampling will know through the CT image that it is outside the myocardium and therefore return a 0 value. This happens because of poor registration, but also because CT and PET scans are taken at different times, different orientations and different stages of the cardiac cycle. When a large misalignment occurs, it is easier to just manually input the perfusion sphere coordinates based on inspection of the mesh geometry, rather than re-registering the two images..... 111

Figure 5-10 Depiction of the placement of PET perfusion measurement spheres (green circles). Note that they are projected forward from the terminal end of the artery, to approximate the myocardial region that is being supplied. The example here is the 10mm diameter measurement sphere. 112

Figure 5-11 Depiction of the placement of PET perfusion measurement spheres (blue circles). Note that they are projected forward from the terminal end of the artery, to approximate the myocardial region that is being supplied. The example here is the 20mm diameter measurement sphere. 113

Figure 5-12 (Left) Illustration of downstream microvascular trees. (Right) Diagram of structured tree downstream microvascular structure. r represents the radius of the terminal vessel, and the daughter branches split asymmetrically in a repeated way, with fractions a and b , with values of 0.9 and 0.6 respectively.[93] This branching occurs indefinitely until it reaches the minimum radius..... 115

Figure 5-13 Schematic showing the outflow boundary conditions. All the boundary conditions are two-element Windkessel models represented in the circuit diagram. 116

Figure 5-14 Comparison of pressure profiles obtained from PET-based boundary conditions (left of pairs) versus conventional morphology-based boundary conditions (right of pairs). Patient 1-10 from top left to the bottom right. Arrows indicate focal stenosis..... 119

Figure 5-15 The FFRs of patients, reordered in reference to the value of FFR calculated with MBC 30%. The bars indicate the range of FFRs obtained using the various MBCs, with the conventional (MBC 30%) marked as a blue diamond, and the PBC marked as orange cross. Patient numbers are shown on the plot as reference..... 121

Figure 6-1 (Top left) 3D rendering of CTCA, (Top right) CT myocardial perfusion, (Bottom left) CTCA slice, (Bottom right) CT dynamic perfusion chart) from [181]140

Figure 6-2 The ratio of flow during hyperaemia and rest, the Coronary Flow Reserve (CFR) of each branch outlet as measured. The values shown are just an example and does not represent any particular patient case..... 142

Figure 6-3 The conventional assumption of flow magnitude increase during hyperaemia is applied to the downstream resistance boundary condition. The resistance boundary condition is decreased by this value..... 143

Figure 6-4 The measured (from perfusion imaging) flow magnitude increase during hyperaemia is applied to the corresponding resistance boundary condition. The resistance boundary condition is decreased by this value..... 144

Figure 6-5 The measured (from perfusion imaging) flow magnitude increase during hyperaemia is applied to the corresponding resistance boundary condition. The resistance boundary condition is decreased by this value. However, the branches downstream of the suspected lesion will use the average flow increase of the other branches in the artery, in this case, the LAD, where the other branches show an increase of 3.02 and 2.95, averaging 2.99..... 145

Figure 6-6 The measured (from perfusion imaging) flow magnitude increase during hyperaemia is averaged before being applied to the corresponding resistance boundary condition. The resistance boundary condition is decreased by this value. The measured flow increases of the branches downstream of the suspected lesion are excluded from the average..... 146

Figure 6-7 The patient population average CFR is applied to all branches. The resistance boundary condition is decreased by this value..... 148

Figure 6-8 The patient specific estimate of hyperaemic flow increase is applied to all branches. The resistance boundary condition is decreased by this value. The estimate uses patient metrics and patient population data to calculate a patient specific value..... 149

Figure 6-9 Bland Altman plot showing the performance of Patient specific CFR estimation versus CFR obtained from directly measured CT perfusion. 159

Figure 6-10 Bland-Altman plot comparing the conventional FFRCT method with Invasive FFR. Note the particularly strong negative bias of the conventional method, i.e., FFR values are lower in the conventional FFRCT than that measured invasively 164

Figure 6-11 Bland-Altman chart comparing the patient population average assumption FFRCT with Invasive FFR. Note the slight positive bias of this method, i.e., this FFRCT method produces slightly higher FFR values on average..... 164

Figure 6-12 Bland-Altman chart comparing the FFRCT using a directly measured CFR value with Invasive FFR..... 165

Figure 6-13 Bland-Altman chart comparing the FFRCT using an estimated CFR assumption based on patient specific metrics, with Invasive FFR. 165

Figure 6-14 Relationship between FFR and Hyperaemic Response..... 175

Tables

Table 2-1 Diagnostic performance of various coronary artery stenosis severity tests. Diagnostic accuracy is based on comparison with reference standard FFR < 0.80 for per-vessel ischaemia..... 39

Table 3-1 The difference in pressure values calculated in the CFD simulation using various mesh sizes..... 71

Table 4-1 Patient-specific and population average inflow parameters during hyperaemia. Note: the heart rate is elevated due to adenosine administration. 88

Table 4-2 Comparison of pressure ratio/FFR values obtained using various types of simulation. 91

Table 4-3 Comparison of pulsatile FFR, iFR, resting Pd/Pa, steady-state FFR and resting Pd/Pa. Simulations were done using patient-specific inflows..... 93

Table 4-4 Comparison of flow rates out of stenosed and healthy branches, pulsatile versus steady. Simulations were done using patient-specific inflows..... 93

Table 5-1 Patient data table..... 102

Table 5-2 Perfusion and coronary flow reserve obtained from PET imaging. *Vessel specific flow reserve and absolute perfusion (during stress) was obtained by sampling the region supplied by the stenosed vessel. **LAD, LCX, RCA regional flow reserves and absolute perfusion are obtained by Siemens Syngo software package. Yellow shaded cells indicate the vessel that has the suspected stenosis. 105

Table 5-3 Pixel deviation (variability) between two attempts of co-registration. Note that the value is absolute, i.e., strictly positive. Error is the result of manual selection of corresponding landmarks..... 109

Table 5-4 CT-based FFR values obtained using various outflow boundary conditions. PBC: PET-based boundary condition, MBC: morphology-based boundary condition. The percentage values indicate reduced resistance level to account for hyperaemic flow increase and reduction to 30% (MBC 30%) is the conventional assumption. *This is technically not FFR as it is in the rest state, but rather Pd/Pa. 122

Table 5-5 Flow rates through stenosed branch and proportion of that to the overall coronary flow (%), obtained using various outflow boundary conditions. 123

Table 5-6 CT-based FFR values for Patient 10 when each diseased vessel's hyperaemic condition was varied individually and in combination.....	124
Table 6-1 Regression coefficients, error, and significance of various patient metrics on the overall CFR (excluding suspected branch) of a patient. This was calculated using the PET perfusion data set (n = 101), performing univariate regression on each data point individually. Coloured cells indicate the statistically significant coefficients (P value \sim <0.1).	151
Table 6-2 Multiple regression of the variables that were statistically significant in Table 6-1. The least significant variable is removed to perform the following step in Table 6-3..	151
Table 6-3 Multiple regression of the remaining variables, hypertension's influence on the patient's CFR is not significant and is further knocked out to produce the final model in Table 6-4.....	152
Table 6-4 Regression coefficients, Standard Error and P-value of a reduced model that utilises only variables have a significance of $P < 0.05$	152
Table 6-5 Patient specific predicted CFR based on patient metrics compared to measured CFR.....	157
Table 6-6 The various CFR/hyperaemic flow response values used in FFRCT simulations.....	158
Table 6-7 FFR values obtained by various hyperaemic flow response values applied to the downstream outlet boundary condition. The increase in flow is shown unless it is patient specific (they are shown in Table 6-4)	161
Table 6-8 Sensitivity, Specificity, Positive Predictive value, Negative Predictive value, Accuracy and Balanced Accuracy for various FFRCT methods compared to the Invasive FFR method. Note that this is referring to diagnostic accuracy.....	162
Table 6-9 Mean error in FFR measurement of various methods relative to the invasive FFR measurement. *Note that Invasive FFR itself has a retest variability and has been included here for reference.....	166
Table 6-10 The probability that a FFRCT result disagrees (misdiagnoses) with the diagnostic result of the Invasive FFR measurement based on the distribution of CFR values for each patient (or average over all patients).	167

Nomenclature

BC	Boundary Condition
CAD	Coronary Artery Disease
CFD	Computational Fluid Dynamics
CFR	Coronary Flow Reserve
CT	Computed Tomography
CTCA	CT Coronary Angiography
FFR	Fractional Flow Reserve
FFRCT	CT-based FFR
IFR	Instantaneous Wave-Free Ratio
IMR	Index of Microvascular Resistance
LAD	Left Anterior Descending Artery
LCX	Left Circumflex Artery
LP	Lumped Parameter
mmHg	Millimetres of Mercury
MPI	Myocardial Perfusion Imaging
MVD	Microvascular Disease
NPV	Negative Predictive Value
Pd/Pa	Pressure distal to stenosis/Pressure proximal (Pressure at Aorta)
PET	Positron Emission Tomography
PPV	Positive Predictive Value
RCA	Right Coronary Artery

Chapter 1. Introduction

1.1. Problem overview

Coronary heart disease or ischaemic heart disease is the leading cause of death globally. In the UK alone deaths by coronary heart disease account for more than 12% of deaths by all causes across all ages [4]. Ischaemia occurs when the myocardial tissue does not receive enough glucose and oxygen, usually from a restriction in blood flow to muscle tissue. As myocardial cells die from the lack of oxygen, it can lead to myocardial infarction that is commonly known as a “heart attack”. This can lead to permanent heart muscle damage, scarring and even heart muscle death.

Generally, a restricted blood flow in the myocardium is caused by a stenosis or multiple stenoses in the coronary artery system; a narrowing of the lumen (the space for blood flow) caused by a lesion typically of atherosclerotic plaques. Chronic stenoses can lead to transient ischaemia which can eventually lead to ventricular arrhythmia and even fibrillation, also causing patient death [5]

Due to its preventable and treatable nature, there has been many techniques proposed, and continuously improved, to aid the prognosis and diagnosis of potential CAD patients. One such measure is Fractional Flow Reserve (FFR). FFR is the ratio of the blood pressure proximal to (upstream of) a suspected lesion, and the pressure distal to (downstream of) the lesion (shown in Figure 1-1). It has been shown that FFR is highly determinative of patient outcomes after treatment, and has become a quantifier to the significance of a stenotic artery, directly quantifying the severity of the ischaemia and producing an important indicator for physicians to plan an interventional strategy [6]. To calculate this value traditionally required catheterisation which is invasive/minimally invasive. However, non-invasive or catheterisation-free alternatives have been sought since angiography techniques have evolved and matured, most notable being Computed Tomography Coronary Angiography (CTCA). Non-invasive methods do not

expose the patient to the risk of complications that invasive and minimally invasive methods do.

$$\text{FFR} = \frac{\text{Distal Coronary Pressure (Pd)}}{\text{Proximal Coronary Pressure (Pa)}} \\ \text{(During Maximum Hyperemia)}$$

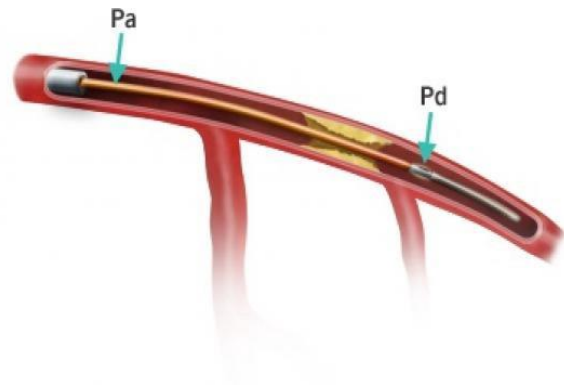


Figure 1-1 Diagram showing a pressure wire measuring the pressure proximal Pa and pressure distal Pd to the obstruction. Note that this pressure wire is inserted using a catheter with the patient under the effects of adenosine induced hyperaemia. FFR is the ratio of Pd and Pa [7].

Recently, clinically viable non-invasive FFR has been derived using FFRCT (Computed Tomography measured FFR) techniques. One of the most promising ways is to use computational fluid dynamics (CFD) to simulate blood flow in a 3D CT reconstructed coronary artery geometry. Blood flow simulation allows predictions on pressure changes across stenoses without the need of catheter-based measurements or other invasive physiological tests. However, there are many assumptions made in FFRCT CFD simulations that need to be addressed, and this study will investigate where these assumptions are valid and where it fails, using PET perfusion and CT perfusion data to supplement the conventional model.

1.2. Aims and objectives

The overarching aim of this project was to investigate CT-based FFR computation methods, understand their sensitivity to various input conditions and evaluate potential clinical implications. There are two main aims, each of which has specific objectives, as summarised below.

Aim 1: To examine the sensitivity of FFRCT to inflow and outflow conditions

Objectives:

- Investigate the effect of flow pulsatility on FFRCT.
- Investigate the impact of using population average metrics (heart rate, blood pressure, cardiac output etc) on FFRCT simulations, in comparison to patient specific metrics.
- Investigate the impact of outflow boundary conditions, in particular the vasodilatory response to hyperaemia, on FFRCT.
- Evaluate the differences between various functional measures (iFR, Resting Pd/Pa, CFR, etc.) in comparison to FFR.

Aim 2: To propose and examine a method to improve FFRCT

Objectives:

- Develop a method to define outflow boundary conditions based on perfusion images.
- Investigate the variability of hyperaemic response for different patient profiles (young, old, male, female, smoker, non smoker etc).
- Develop a method to define outflow boundary conditions that reflect patient-specific myocardial perfusion but without the need of perfusion images.
- Evaluate the proposed methods against invasive FFR and assess their potential clinical implications.

1.3. Thesis structure

Chapter 1 will set out the research problem and the questions that this project attempts to answer.

Chapter 2 will lay out some of the background information needed to understand the clinical problem, the diagnostic techniques currently in use, what FFRCT is and what are its strengths and weaknesses.

Chapter 3 will set out the broad methodology. Describing the clinical data used in this study, the anatomical model reconstruction, and the simulation scheme.

Chapter 4 explores primarily the inflow boundary conditions into the coronary tree, the effects of pulsatility of flow, blood pressure and stroke volume on the variability of FFRCT.

Chapter 5 explores primarily the outflow boundary conditions, the assumptions on coronary microvascular flow, the flow response to hyperaemia and whether perfusion imaging can provide insight into the variability of these assumptions.

Chapter 6 attempts to produce a clinically viable model of making assumptions based on more patient specific metrics like sex, smoker status and diabetes etc.

Chapter 7 will provide the conclusions to this project, identify broad limitations, and suggest the next step for future work.

Chapter 2. Background

2.1. Clinical background

2.1.1. Heart anatomy

The human circulatory system has four main vessels, the aorta, the vena cava, the pulmonary artery and the pulmonary vein. The Aorta carries oxygenated blood out of the heart to supply the body as well as the heart muscle (the myocardium), via the smaller coronary artery branches, which needs oxygen and nutrients to function. The pulmonary artery takes deoxygenated blood into the lungs to be oxygenated, and the pulmonary vein carries oxygenated blood back to the heart. The Vena Cava takes deoxygenated blood from the body back into the heart. In this study, the main region of interest in this study is the aorta, coronary arteries and the myocardium.

The cardiac cycle is divided into two parts, diastole and systole. Diastole is the expansion and relaxation of the heart, where deoxygenated blood from the body and oxygenated blood from the lungs travels into the heart. Systole is the contraction of the heart muscle, causing blood to be pumped out, deoxygenated blood into the lungs, and oxygenated blood around the body. As the heart muscle (or myocardium) itself requires nutrients and oxygen, and blood inside the ventricle does not perfuse into the myocardium, blood must be supplied externally via the aorta. The system of blood vessels coming out of the aorta to supply the myocardium, is known collectively as the coronary arteries.

Generally, there are two main coronary arteries coming off the aortic sinus which are referred to as the Left Main stem and right coronary arteries. Further in describing anatomy and in diagnoses, two prominent branches after the left main stem – Left Anterior Descending (LAD) and Left Circumflex (LCX) – and the Right Coronary Artery (RCA) are often referred to. These major coronary arteries are usually called epicardial vessels to distinguish them from the small branches at the terminal ends, the

microvasculature. The RCA supplies blood to the right atrium and right ventricle, as well as the sinoatrial node, which regulates heart rate and rhythm. The LAD supplies blood to the front (anterior side) of the left heart muscle and the LCX supplies around the side and back. The left heart muscle is much larger due to the pressure demands of pumping blood around the whole body versus just the lungs, which the right heart muscle is responsible for. A diagram of the heart and its coronary arteries are shown in Figure 2-1.

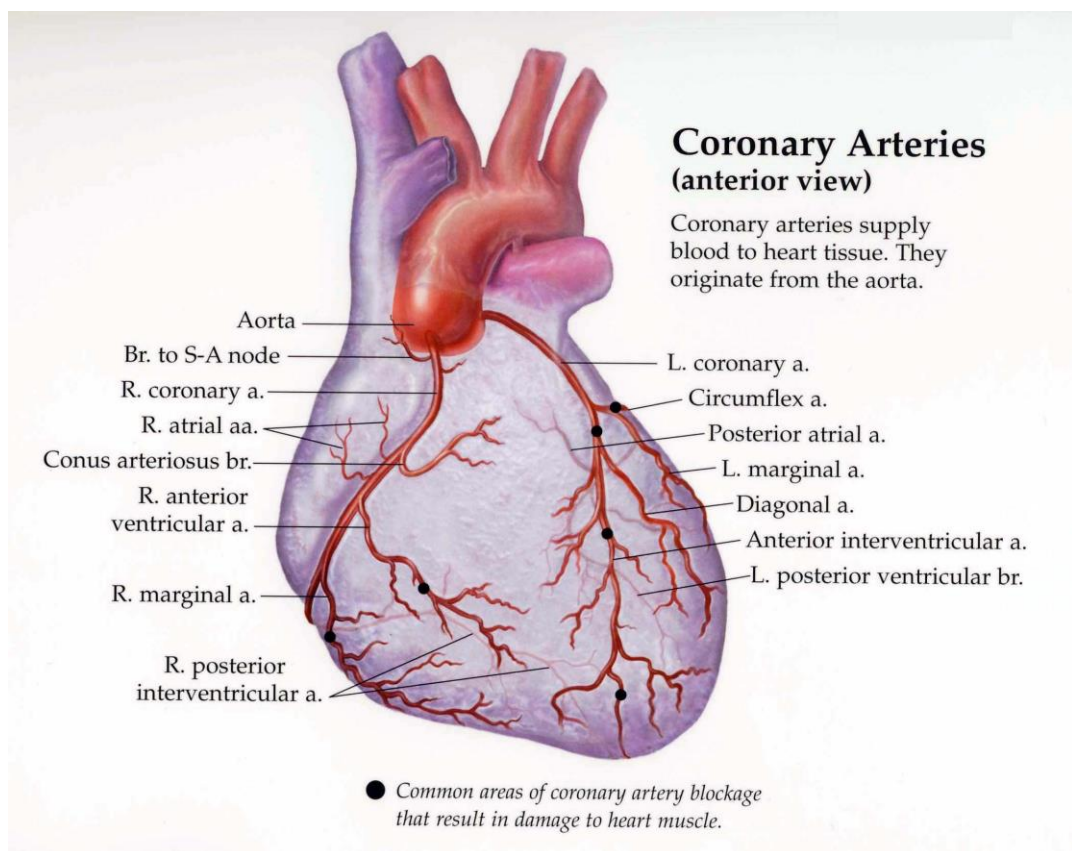


Figure 2-1 Anatomical diagram of the human heart displaying the coronary arteries and major blood vessels. Of particular importance is the Right Coronary Artery (RCA), Left Anterior Descending (LAD) and Left Circumflex (LCX) which wraps around the back of the heart. Diagram from [8]

2.1.2 Coronary Artery Disease

A build-up of plaque in the arteries can cause an obstruction or even a complete blockage, which is known as atherosclerosis [9,10]. It begins with deposits of white blood cells and the remains of dead cells such as cholesterols and fats, forming “fatty streaks” across the arterial wall. As they

build up, calcification occurs, significantly hardening the arterial wall. In the early and mid stages of this process, most individuals are asymptomatic, with some experiencing interference with their ability to perform intense physical exercise. The progression of the disease starts narrowing the vessel lumen (=stenosis) which limits the flow, and in response, the body will increase blood pressure beyond healthy levels to compensate for the restricted flow. Symptoms are more apparent in older men above the age of 50, where plaques obstruct coronary flow and cause momentary phases of ischaemia during physical stress, causing chest pain or angina when the oxygen supply to the myocardium is temporarily subdued. This is usually the starting point for patients to seek medical help [11].

However, mild to intermediate coronary artery stenosis often does not cause ischaemia, and there are other reasons behind myocardial ischaemia such as microvascular disease.

2.1.2. Coronary Microvascular Disease

Coronary microvascular disease also known as microvascular disease (MVD) is when instead of plaques or stenoses, the endothelial cells (inner wall) of the micro vessels are damaged and subsequently leads to reduced flow [12]. Female patients presenting with stable angina tend to have no obstructive disease 65% of the time versus 32% of men, this is mostly attributed to microvascular disease. As the symptoms for ischaemia are similar whether caused by an epicardial stenosis or microvascular disease, imaging modalities such as perfusion that can only identify the presence of ischaemia may fail to identify the cause of flow limitation.

2.1.3. Hyperaemia

A crucial aspect of coronary flow and the effects of coronary artery disease is to understand the physiological effect known as hyperaemia, also sometimes known as stress. In the stressed or hyperaemic state, blood vessels surrounding muscle tissues that require additional oxygen or nutrients will dilate causing an increase blood flow and perfusion into those

muscle tissues. To reach hyperaemia, it can be achieved via physical stress such as exercise, this is where “stress testing” comes in, or pharmacologically induced by adenosine. Adenosine induces direct coronary arteriolar vasodilation through specific activation of the A_{2A} receptor. This usually results in a 3.5- to 4-fold increase in myocardial blood flow[13]. Under such hyperaemic conditions, coronary blood flow is directly proportional to perfusion pressure and a reduction in perfusion pressure due to a coronary stenosis will thus proportionally decrease coronary flow during hyperaemia[14].

For most functional diagnostic tests of coronary function, reaching a state of hyperaemia is essential as that’s when flow limiting effects of a stenosis is maximised.

2.2. CAD diagnosis and care

2.2.1. Typical care pathway

The typical pathway for diagnosing and treating suspected CAD patients, shown in [Figure 2-2](#), starts when a person presents with stable angina (chest pain).

After initial management and ECG testing, following the NICE guidelines (latest update 2016), the first line assessment at diagnostic investigations has been to perform a 64-slice (or higher) CT coronary angiography [11]. If the CT coronary angiography returns with a non-diagnostic result or evidence of some coronary artery disease of uncertain functional significance, then a next phase of assessment is needed. The second line assessment is to offer a non-invasive functional test, such as Myocardial Perfusion scanning with SPECT, stress-echocardiography and Coronary Magnetic Resonance Imaging (CMR) [11].

Assessing and diagnosing suspected stable angina

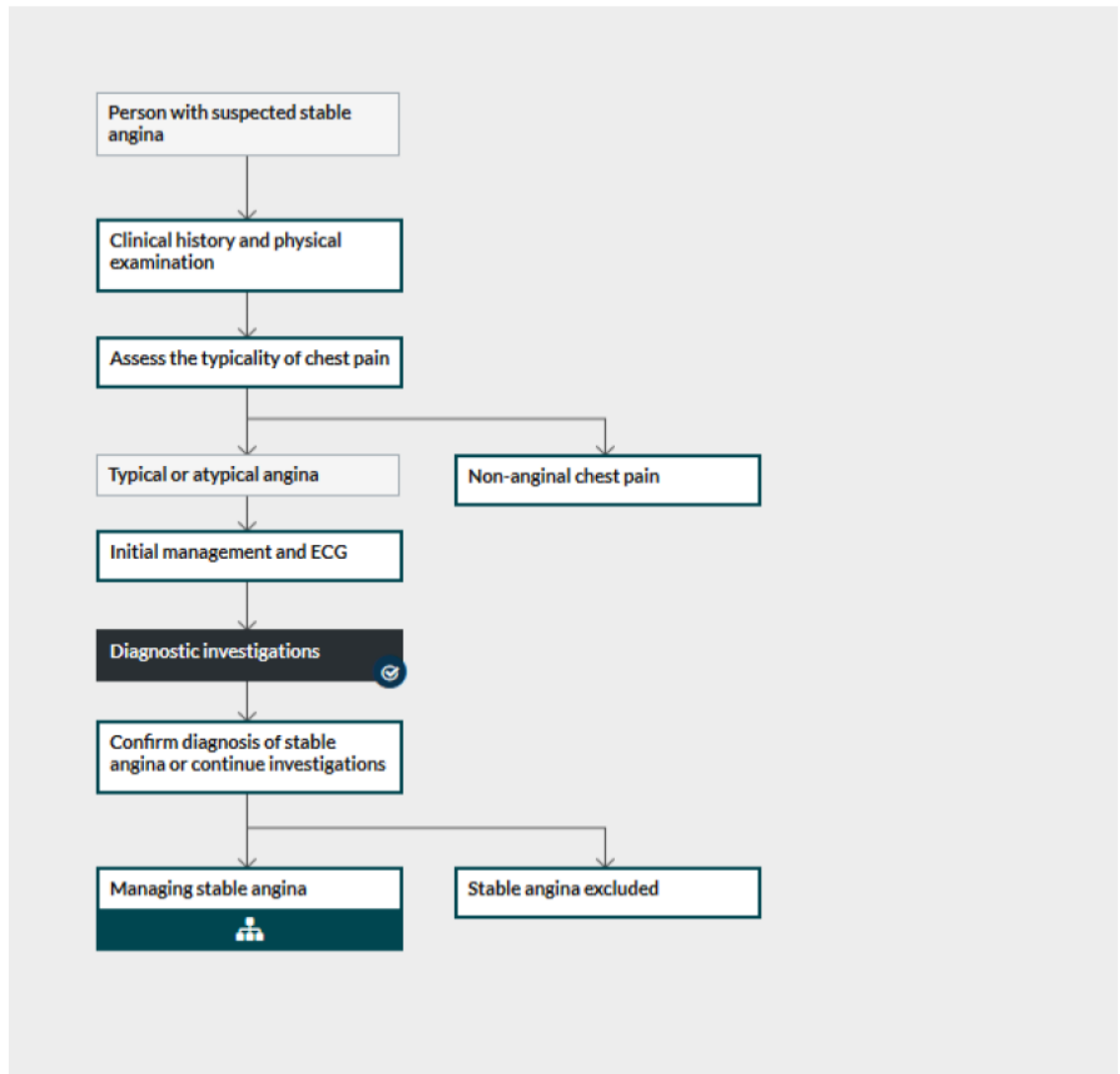


Figure 2-2 Typical diagnostic and care pathway for patients with suspected angina (chest pain). This diagram is from the NICE guidelines 2017 for patients presenting with chest pain [11]

Although the NICE guidelines (see Figure 2-2) are clear on the recommended procedure of treating potential CAD patients, which have been carefully decided by taking into account diagnostic accuracy, patient risk, comorbidity, cost etc, not all hospitals have the facilities to follow it through and therefore often skip or use alternative tests [11].

However, while the first line CTCA may not be readily available for every patient, there is strong evidence that it is the best single non-invasive test at the present, and the adoption of routine CTCA is growing rapidly [15].

2.2.2. Invasive Coronary Angiography (ICA)

The current standard method for detecting CAD is invasive coronary angiography (ICA), shown in Figure 2-3, often also known as just coronary angiography. It involves X-ray projection imaging of the chest with catheter-delivered contrast agent to highlight the blood vessels *Figure 2-3*. One of the main issues faced by ICA is the disparity between the angiographic observations (the anatomical measurement) of a stenosis, and the pathological severity, how likely it causes ischaemia as it progresses. Coronary physiology has been shown in large clinical studies to be a much better predictor of clinical outcomes [16,17]. Non-invasive functional tests are usually performed to detect ischaemia before any ICA or revascularisation procedures take place [16]. However, patients are still routinely recommended for ICAs, indicating the limited trust in the performance of standard non-invasive tests.

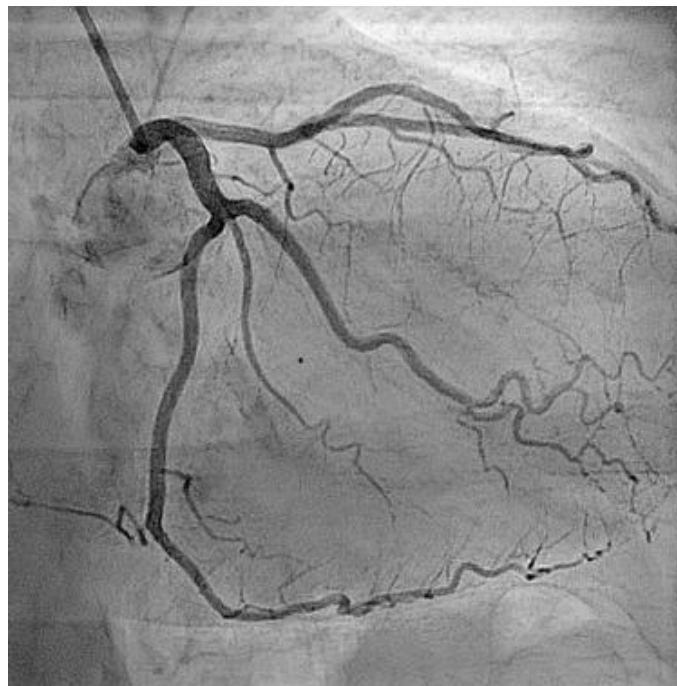


Figure 2-3 An example of a coronary angiogram obtained under Invasive Coronary Angiography (ICA). Image from [18]

2.2.3. CT Coronary Angiography (CTCA)

Non-invasive imaging based assessment such as Computed Tomography Coronary Angiography (CTCA) is being used more regularly to detect significant CAD or rule out non-significant CAD [19,20]. CTCA has a high specificity, when no coronary stenoses are detected, the prognosis is usually excellent, foregoing any need for further diagnostic evaluation [19], however the sensitivity, the correlation of detected stenoses and the likelihood of downstream myocardial ischaemia is poor, diagnostic accuracy for a hemodynamically significant lesion at 49%[20].

It has superior spatial and temporal resolution than other imaging modalities [21,22]. The limitation of CTCA is that it does not quantify anything further than geometry. CTCA is also split between visual CTCA and quantitative CTCA, the former requires the operator to visually identify and assess the severity of a stenosis whilst the latter uses computational techniques like automatic edge detection to quantify the % obstruction. Visual CTCA depends far more on operator skill and consistency and is falling out favour.

By combining CT imaging with CFD and models on coronary microvasculature, FFR values can be estimated, and the technique is called FFRCT.

FFRCT, instead of catheter based invasive FFR, has been reported by one of the teams that has worked on the FAME trials, that it leads to better patient outcomes as well as lower economic costs compared to invasive FFR. There was a caveat that patients had higher medical costs after undergoing FFRCT because FFRCT guided strategy was associated with more subsequent cardiac procedures, however it was also correlated with a far greater quality-of-life outcome [23]. Bamberg et al [24] conducted a meta-analysis of CTCA, looking at 11 studies, covering over 7000 patients, majority over 59, male and have suffered from one or more significant coronary stenosis. Follow-up assessments of these patients had a median of 20.4 months, with the maximum at 6 years [24]. Stenoses detected by CTCA showed a Hazard Ratio (HR) of 4.5 and a 95%

confidence interval of 2.2 and 9.3, than those without. Indicating that the event rate of a patient with a CTCA-detected stenosis was 4.5 times higher than a patient without a stenosis detected [24].

2.2.4. CTCA Limitations

Reliable and consistent segmentation of CT angiograms are essential for CFD. A poorly segmented 3D model will produce useless results with CFD.

The assumption that structural information is sufficient to determine the severity of coronary artery stenosis has been countered by the FAME studies that have shown volumetric narrowing of an artery is only weakly correlated with FFR. In other words, vessels with an identical degree of stenosis (as a radius or area constriction) could have vastly different FFRs and hence physiological significance.

Patients with a high Coronary Artery Calcium (CAC) score also limit the performance of CTCA. [25,26] While sensitivity for detecting a functionally significant stenosis is high at 95%+ for all CAC scores, specificity drops from 90% for CAC scores of <100 to 42% for CAC scores of >400. Otherwise physiologically healthy vessels may be misidentified as a significant stenosis due to the poor specificity at high calcium levels. A purely physiological measure like FFRCT is capable of overcoming these effects, and Norgaard et al using results from an FFRCT clinical trial (the NXT study) has shown that CAC values have no noticeable influence on both specificity and sensitivity of FFRCT detecting a significant stenosis [27].

2.2.5. Alternative CTCA techniques

With the emergence of Computed Tomography Coronary Angiography (CTCA), multiple techniques other than FFRCT have been proposed to address the disparity between angiographically significant stenoses and physiologically significant stenoses as indicators of ischaemia.

An alternative is Transluminal attenuation gradient (TAG) which looks at the intraluminal radiological attenuation in Hounsfield Units, measured in intervals (usually 5mm) [28,29].

Another measure to identify coronary arteries with abnormal flow is Corrected Coronary Opacification (CCO) [30]. Using CT, the technique looks at the mean intraluminal Hounsfield units (HU) across two slices that cover the stenosis. The method was developed precisely to compensate for the insufficient predictive power of a standard CTA, by looking also at functional significance of a stenosis. However, CCO has limited performance while the patient is under hyperaemia (stressed state - maximal flow), and as hyperaemic flow is the strongest indicator for coronary health, the functional predictive power of CCO is currently still low, and further work is being done to fully develop the method [30].

CCO and TAG were evaluated against invasively measured FFR, showing mediocre performance with moderate-high specificity but insufficient sensitivity. TAG reported sensitivity of 45% and specificity of 95%, while CCO reported those of 65% and 95%, respectively. The conclusion from this evaluation showed that classification of patients based on those techniques were less than desirable, and required technical improvements to become viable [31]. In contrast, other studies show that TAG and CCO has some utility despite its moderate performance as it is still supplementary information that may reduce the number of total invasive interventional procedures [32].

2.2.6. Percutaneous coronary intervention (PCI) and treatment guidance

Percutaneous Coronary Intervention (PCI) (diagram shown in *Figure 2-4*) is the standard treatment for coronary artery disease in the epicardial sites (the major branches). A catheter with a balloon and a stent is brought to the suspected stenosis and expanded to “open up” the artery to ideally restore normal flow.

However, up to half of all PCI procedures that were guided by angiography (ICA or CTCA) alone were found unnecessary and did not improve patient outcomes while exposing the patient to risks, albeit small, of catheterisation [33]. Despite this trend, interventionalists had a tendency to stent every stenosis that are observed on images of patients (this is called “Oculo-stenotic reflex”) and functional tests such as FFR were developed in order to better guide them [34].

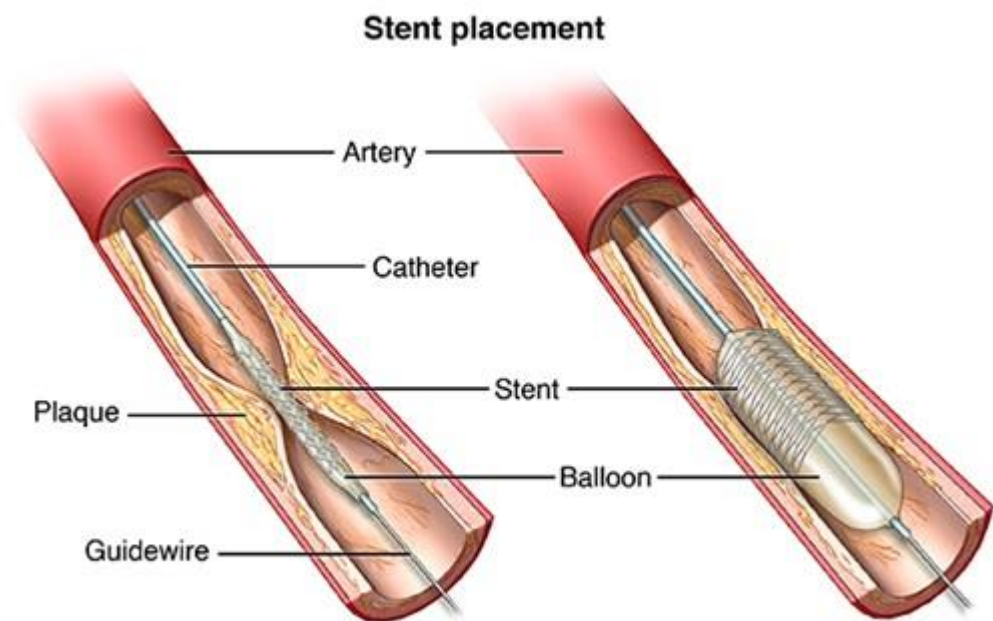


Figure 2-4 Diagram of stenting procedure, taken from [35]

2.2.7. Comparing various diagnostic measures

There are generally three types of tests presented in **Table 2-1**, anatomy based imaging, perfusion based imaging and imaging based FFR. Anatomic based imaging includes the various types of angiography; ICA and CTCA which essentially determines the severity of an obstruction based solely on the size of the obstruction. As these methods incorporate to a large extent the subjectivity of the operator, various CTCA visual studies have shown varied results (accuracy ranging from 59% to 91%) which are presented in **Table 2-1**. The common trend however is that these tests

have a high negative predictive value, i.e., it can be used reliably to rule out negative cases when the stenosis appears mild. However, they have modest positive predictive values, i.e., they are less accurate at determining whether an intermediate stenosis is likely ischaemia causing or not. The premise of FFR is to address this weakness.

Table 2-1 Diagnostic performance of various coronary artery stenosis severity tests. Diagnostic accuracy is based on comparison with reference standard FFR < 0.80 for per-vessel ischaemia.

Test	N vessels	Sensitivity	Specificity	PPV	NPV	Accuracy
ICA [36]	79	57%	69%	49%	76%	65%
FFR-Angio [37]	352	94%	91%	89%	95%	92%
CTCA (quantitative) [36]	79	45%	79%	54%	73%	67%
CTCA(visual) [36]	79	94%	48%	49%	43%	64%
CTCA(visual) [38]	107	75%	95%	76%	94%	91%
CTCA(visual) [39]	103	91%	40%	47%	89%	59%
MPI-SPECT [40]	72	73%	82%	52%	92%	80%
MPI-MR [41]	50	97%	60%	65%	96%	76%
MPI-PET [38]	195	95%	92%	78%	98%	92%
MPI-PET + CTCA [38]	107	93%	99%	96%	99%	98%
MPI-CT [42]	42	76%	84%	82%	79%	80%
MPI-CT + CTCA [42]	42	68%	98%	97%	77%	84%
CT-FFR [39]	103	88%	82%	74%	92%	84%
CT-FFR [43]	252	90%	54%	67%	84%	73%

Myocardial Perfusion Imaging (MPI) methods such as PET, MRI, CT perfusion etc. generally have higher PPVs and similarly high NPVs, as perfusion imaging directly samples the myocardial regions supplied by the coronary arteries and can confidently determine whether any region is under-perfused which is caused by a stenosis upstream. A hybrid approach that uses both anatomy and perfusion-based imaging also produces superior results to each method individually such as MPI-PET and CTCA reaching an accuracy of 98% versus 92% and 67% individually. Here, the direct measurement of perfusion that indicates presence of ischaemia and

the anatomical imaging that indicates the extent of an obstruction complement each other.

Imaging based FFR seeks to mitigate the weaknesses of purely anatomical imaging methods like CTCA or ICA, supplementing the anatomical information with functional information produced using CFD simulations without the use of additional imaging, adenosine or invasive methods. Its performance is similar to most of MPI methods but still inferior to the gold standard of MPI: MPI-PET (CT-FFR accuracy 73-84% vs MPI-PET accuracy of 92%). Similarly to CTCA, imaging-based FFR still relies substantially on anatomical features and does not take into account microvascular health hence often overestimates the functional significance of a stenosis, therefore resulting in a slightly weaker positive predictive value [44].

2.3. Functional measures of severity

2.3.1. Fractional flow reserve (FFR)

Fractional Flow Reserve (FFR) was a new physiological metric that improved the traditionally poor performance of non-invasive tests. FFR is defined by the ratio of maximal blood flow across the stenotic artery over the presumed maximal normal blood flow (as if the obstruction isn't there), realistically this is calculated using the ratio of blood pressure proximal to the stenotic section of the artery and the blood pressure distal to the stenotic section [45]. In a standard procedure, it is measured using invasive catheterisation techniques. FFR essentially represents the physiological significance of a coronary stenosis, with a high predictive value in determining the haemodynamic significance of the stenosis and subsequent treatments required. FFR has been shown superior to just observing the degree of a stenosis (fraction that is obstructed) in determining the likelihood of ischaemia. In the group of patients examined in this study, a significant portion of cases where the patient had a mild stenosis detected using ICA actually suffered from ischaemia. On the other hand, half of the

patients with stenoses that were determined as “high grade” in ICA did not suffer from ischaemia. These facts indicate that the potential of FFR to reduce unnecessary follow-up procedures, saving both costs and potential patient risk.

There were three main clinical studies that demonstrated the effectiveness of FFR in the clinical setting: DEFER, FAME1, FAME2. The first study, DEFER tested whether FFR guided treatment for potentially ischaemic coronary stenosis was appropriate [46,47]. The standard procedure for determining the prognosis of a stenotic artery at the time was based purely on anatomical measurements such as the volumetric narrowing of the arteries, symptoms such as angina and/or blood pressure during exercise. The DEFER study showed that FFR guided therapy provides far better outcomes and FFR is an excellent prognostic tool. It found that a stenosis with FFR > 0.75 is deemed non-ischaemic, requiring no further treatments but resulting in an excellent outcome: risk of death or acute myocardial infarction was less than 1% per year [46,47]. For the control group that were stented (stenotic section were opened up) even if FFR is higher than 0.75, it was shown that their event rates (i.e., risk of death or infarction) had not been reduced, indicating that further treatment was unnecessary [46,47].

The FAME1 and FAME2 trials were much larger and notable in the medical community, and set the new benchmark for coronary artery disease treatment in the US and the UK first [47]. The FAME trials were cross-centre trials involving hospitals in both countries. FAME1 focused on patients with multi-vessel diseases, and whether FFR was useful in guiding percutaneous coronary intervention (PCI) treatments. All the patients in this trial were recommended for stenting after an angiography. The patient was then separated into two groups, the FFR+Angiography (FFR+A) group and the Angiography Only (AO) group. Every patient in the AO group were stented whereas only those in the FFR+A group that had a measured FFR value <0.8 had a stent implanted. The FFR+A group received 33% fewer stents overall, however in comparison to the AO group, the patient outcomes of the group were significantly better. Here, the patient outcomes were defined as

the 1-year event rate (death, nonfatal MI, or repeat revascularization) which was significantly higher in the AO group (18.3%) in comparison to the FFR+A group (13.2%) [48]. This demonstrates that many stenting procedures were unnecessary, and not only does it not improve outcomes, in many cases it could work to its detriment.[48]

The second trial FAME 2 compared FFR guided PCI with Optimal Medical Therapy (OMT), as PCI without FFR was demonstrated to be equal to the OMT [49]. The 1-year event rate for the FFR guided PCI group was 4.3%, significantly lower than the OMT group which had 12.7%. The FFR guided PCI patients also showed better Quality of Life indicators.

Since the outcomes of the DEFER and FAME studies, FFR has established itself as the gold standard for coronary artery disease diagnosis and prognosis in interventional cardiology [49].

2.3.2. Invasive FFR

Measurement of FFR is an invasive/minimally invasive procedure involving a catheter with a pressure wire see figure Figure 1-1. In a standard diagnostic process, a patient first undergoes some form of angiography (intravascular or CT). If a significant stenosis, where the narrowing is 50% or greater (percentage obstructed), is identified, they are then recommended for an invasive FFR measurement prior to treatment decision [50–52]. Note that a stenosis that show greater than 70% obstruction also often skip FFR measurements due to the very high likelihood of it being an ischaemia inducing stenosis [50–52].

In the catheterisation lab, the patient undergoes both ICA and FFR measurement in one procedural session. The catheter is inserted into the arteries usually via an incision in the leg or the arm and leads up to the coronary artery branch in question. The pressure wire measures the pressure at locations between the start the of the coronary branch and the lesion, and between the lesion and the terminus of the coronary branch. The ratio of the two pressure values is the FFR. This procedure must be

performed with the patient in a “stressed” or hyperaemic state that is pharmacologically induced, typically by adenosine.

While catheter procedures are minimally invasive, it does not come without risk of complications such as perforating the arterial wall, MI, arrhythmia and small chance of stroke [33]. Considering that 40% of patients that undergo these procedures do not have a functionally significant stenoses and therefore do not require further treatment, cardiologists are looking at ways to quantify FFR with non-invasive imaging-based methods.

2.3.3. FFR derived from Coronary Angiography (FFR-Angio)

FFR derived from ICA (but not measured directly using a pressure wire) is a more recent development in comparison to FFRCT. It is also a computational method that uses the high-resolution ICA anatomy to produce an image based FFR value. As shown in the comparison of tests, **Table 2-1**, it provides some of the highest diagnostic accuracy of 91%, comparable to MPI-PET, with high sensitivity and specificity of 94% and 91% respectively [37]. The advantage of FFR-Angio over invasive FFR is the forgoing of vasodilators such as adenosine, however it is still fundamentally an invasive method and carries the risks of catheterisation.

2.3.4. Coronary Flow Reserve (CFR)

Coronary Flow Reserve (CFR) is another indicate often used to assess the functionality of myocardial circulation. CFR is defined as the ratio of flow into the myocardium between a patient in a rest (baseline flow) and stressed state (maximal flow). CFR is used both as a diagnostic measure and a gauge for vasodilator drug response as well as a patient's response to treatment. CFR can be measured invasively through catheterisation and through non-invasive means such as PET perfusion imaging and myocardial perfusion SPECT.

$$CFR = \frac{\text{Maximal (hyperaemic) Flow}}{\text{Rest Flow}} \quad (1)$$

The normal range for CFR is >2 (and usually between 2 and 4), whereas the diseased range is more loosely defined as somewhere less than 2 or less than 1.5, leaving a “gray zone” of 1.5 – 2. CFR is a strong indicator of disease-causing ischaemia in the coronary tree; however, it is unable to distinguish clearly between epicardial disease or microvascular disease.

2.3.5. Index of Microvascular Resistance (IMR)

Index of Microvascular Resistance (IMR) measures the resistance of the microvascular bed, the small vessels branching off from the epicardial vessels and feeding into the myocardium [53,54]. IMR is calculated as follows:

$$IMR = \frac{Distal\ pressure}{Coronary\ Flow} \quad (2)$$

Distal pressure is the blood pressure at the myocardial end of the epicardial vessels, and coronary flow is the flow into the coronary branch. IMR < 20 is generally considered to be in the normal range, and IMR > 30 is considered diseased.

While IMR is a good indicator of specifically microvascular disease, there is little evidence that IMR is correlated well with clinical outcomes [53,54]. In addition, there is a wide “grey zone” where IMR values between 20 and 30 are neither considered normal nor necessarily diseased [53,54]. Lastly it is generally an invasive measure that is not commonly performed and therefore IMR values are rarely ever recorded.

2.3.6. Instantaneous wave-free ratio (iFR)

Another metric used is the instantaneous wave-free ratio (iFR), an alternative to FFR, for which the pressures measured at the rest state (non-hyperaemic) are used. The primary advantage of iFR is that there is no administering of adenosine to induce hyperaemia, which results in the reduction of cost and adverse effects associated with the drug [55]. The rationale behind iFR lies in the nature of the cardiac cycle, where during the

period immediately following systole, both flow and pressure begin to decay, and the gradient at this time is most closely matched, making the analogous use of pressure drop to represent flow limitation most appropriately. It is currently debated whether resting state measurements can be used to determine CAD severity; however, it has been well demonstrated that iFR, and a similar ratio of baseline Pd/Pa, can be used to rule out the majority of patients before administering vasodilators for FFR measurements [56].

2.3.7. Discordance between functional measures

The three common measures of coronary pathophysiology – FFR, CFR and IMR shown in *Figure 2-5* – are only loosely correlated while each of those is effective for determining ischaemia [53]. A patient can have a poor CFR but healthy levels of FFR and vice versa. However, complimentary information can be gained by knowing both, a patient with poor CFR but healthy FFR and suffers from anginal pain, is likely suffering from microvascular disease for example, effectively ruling out the need for PCI. This becomes important when discussing the benefits of perfusion imaging vs FFR. Perfusion imaging can only inform the clinician whether or not there is some form of disease, it cannot distinguish between epicardial disease or microvascular disease, or a combination of both. FFR on the other hand can definitively measure the stenosis severity of epicardial

disease and therefore identify whether the stenosis needs to be revascularized.

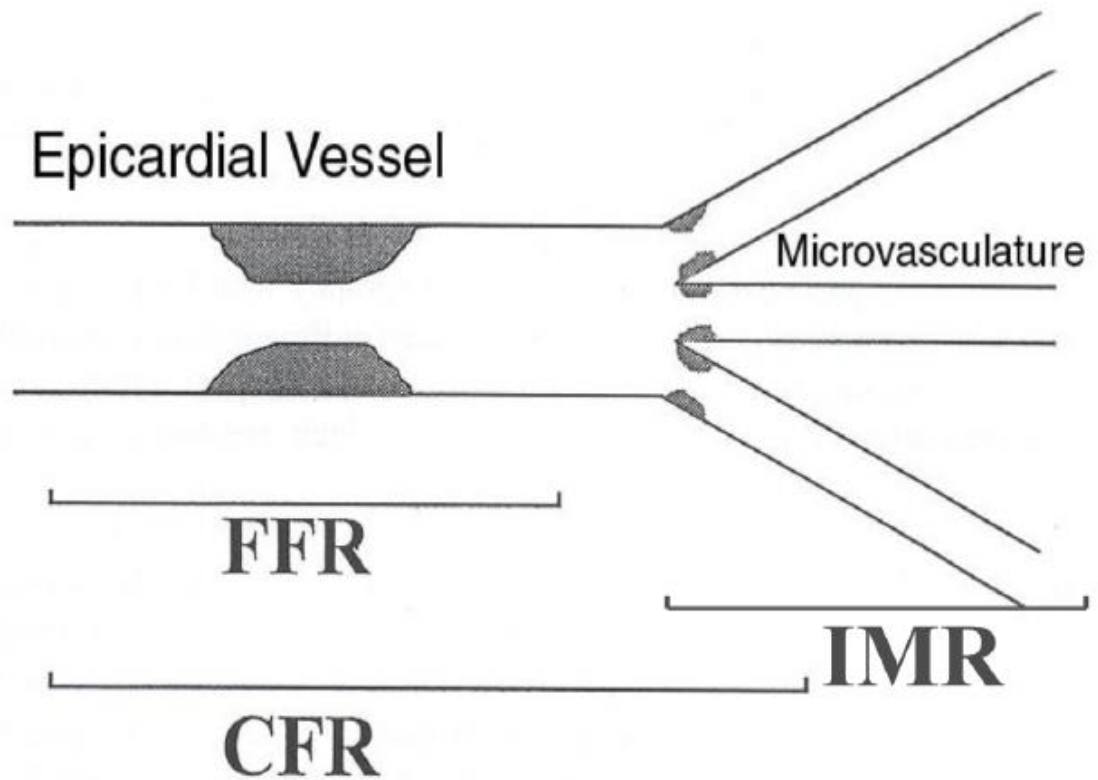


Figure 2-5 The regions of interest in the coronary artery tree that each functional measure can be used to determine the relative “health” of. Diagram from [53]

2.3.8. Hyperaemia

FFR is defined based on the physiological state under maximal coronary blood flow [57,58], which can be achieved during intense physical exercise, however much more consistently achieved in the clinic using pharmaceuticals such as adenosine [59,60].

The maximal blood flow state is known as hyperaemia, which is increased blood flow to specific regions of the body. There are two types: active and reactive hyperaemia [61]. The former is the body’s response to

an increased need for oxygen and nutrients such as physical stress on the muscular-skeletal system, increased brain activity and stress/hormone induced responses such as by adrenaline [61]. Reactive hyperaemia is the response to a region that is undersupplied due to experiencing hypoxia or ischaemia [61]. In the context of the heart, hyperaemia, or a “stressed state” is referring to the increase in coronary blood flow into the myocardium. In the context of diagnostic measurements, when the patient is not in hyperaemic state, the patient is said to be in a “rest state”. Perfusion imaging methods, such as PET, CT Perfusion, MR perfusion, usually take images of the heart in both states.

When performing FFR measurements with a catheter, adenosine is used to achieve hyperaemia. The drug mimics physiological stress and increases blood flow via vasodilation [62][63,64].

2.3.9. PET perfusion imaging

Whilst CTCA is the first line investigation method for potential coronary artery disease due to its relatively low cost and accessibility, Positron Emission Tomography (PET) imaging derives direct measurement of coronary flow and reported to provide superior diagnostic power due to its higher specificity and positive predictive value [65]. In PET imaging, radioactive tracers such as rubidium-82 are injected into the bloodstream and the radioactivity of the tracers allows blood flow to be tracked across the coronary system. This offers useful measures of blood flow in a dynamic view although spatial resolution is not as high as CT (2.5mm vs 0.35mm in CT)

PET myocardial perfusion is considered the current gold standard in myocardial blood flow measurements [66]. Nuclear Myocardial Perfusion scintigraphy (the best myocardial perfusion measure at the time) was the ground truth used in validating invasive FFR.

Combining PET with CT-based coronary images, the flow-based information superimposed on the structural model can be incredibly

powerful, reducing the number of assumptions in a fluid dynamics simulation, thus producing a far more realistic FFR estimation.

PET is not without its downsides. It is expensive, time-consuming and depending on the tracer it can carry a higher radioactive dose to the patient and surrounding technicians/operators [67]. Availability of PET scanners, tracers and qualified personnel is also inconsistent throughout the healthcare system, and therefore PET is rarely specified as a routine diagnostic in national guidelines. However, the additional information provided by PET can pay off, and similarly reduce the need for invasive coronary angiograms, as well as providing accurate diagnosis that can likewise prevent risks from unnecessary interventional procedures [68].

2.3.10. CFD based FFRCT

Computational Fluid Dynamics (CFD) applied to coronary CT images to obtain FFR estimates has found a place in routine clinical practice, as a service provided by industry. A private company in California, USA, HeartFlow performs CFD simulations based on coronary CT images taken in hospitals and returns with a FFRCT values that are used for clinical diagnosis. In the process of FFRCT, a 3D model of coronary arterial tree is first reconstructed from CT images. Due to the limited resolution of CT (~0.5 mm/pixel) being able to resolve the smallest coronary artery branches, the distal ends of the coronary arteries, the microcirculatory system that bridges between the major coronary arteries and the myocardium are not captured in the images hence the 3D arterial tree model only includes epicardial vessels, typically of diameter larger than 2 mm [69]. The effect of microcirculation downstream to the model is represented by boundary conditions at the distal ends of the coronary arterial model. These boundary conditions relies on mathematical models that define resistance of the microvasculature or myocardial blood flow, based on anatomical features at the scale captured in the CT images (e.g., myocardial mass, distal vessel diameter, etc.) [44]. In the HeartFlow's algorithm that can be found in the literature, the microvascular resistances are defined based on the terminal branch diameter. Three clinical studies were performed to demonstrate the

efficacy of Heartflow's FFRCT technique in clinical setting: HeartFlowNXT, DeFACTO and DISCOVER-FLOW[70,71][72].

There are some potential downsides to modelling approach that are currently accepted in the current FFRCT landscape. The most widely debated one is the hyperaemic boundary conditions relying on population-wide statistics to infer anatomy of the microcirculation system as opposed to patient specific data [44]. More specifically, the hyperaemic flow condition is currently modelled by decrease of vascular resistance (down to 30% or normal [44]) or homogenous increase of coronary flow (up to 4 times higher than normal flow across the coronary tree and constant in different individuals [44]). The effect of hyperaemia on the resistance of blood vessels, as appears in CFR, is not visible in CT images due to low spatial resolution and because the CT images are taken while the patient is at rest. This suggests that the boundary condition needs to be modelled but the assumptions to use-population averaged data are not ideal, especially in patients that suffer from microcirculatory disease. With any FFRCT technique, the performance is also hindered by the quality of CT images, artifacts, motion, calcification and misregistration etc [73].

2.3.11. Abnormal Resistance in Atherosclerotic Coronary Arteries

Chilian et al. has discussed the idea that atherosclerosis can cause myocardial ischaemia through various mechanisms that does not consist of a localised hemodynamically significant stenosis in the coronary arteries [74]. An important function of the coronary arteries is the ability to dilate during physiological stress (hyperaemia) or induced hyperaemia through pharmacological means. If the vasodilatory mechanism is impaired, it might be an indicator of atherosclerosis [75].

This problem is easily detected when pressure can be probed directly, such as using a pressure wire catheter. De Bruyne et al. presented a study showing that healthy coronary blood vessels preserve the flow pressure across its length, i.e., no significant pressure drop, when the blood vessel is maximally dilated via adenosine. This suggests that the

vasodilation under hyperaemia leads to increased flow due to an increased diameter, and induced hyperaemia has been reported to increase coronary blood flow up to 4 fold [75]. The study showed an interesting observation that, in more than half of the vessels the resistance to flow in atherosclerotic arteries was high even without a focal stenosis. More specifically, 8% of the patients without focal stenoses had FFR values below the threshold for healthy flow (0.75), suggesting a strong likelihood for a myocardial ischaemia. The study suggests up to 30% of total resistance to flow in diseased arteries can be accounted for by diffuse structural narrowing as opposed to a focal stenosis [75].

Chapter 3. **General Methodology**

3.1. Aim

In this chapter, the aim is to lay out the theory involved in CFD simulations of the coronary arteries and how they will be applied in the investigations. Starting with the electrical-hydraulic analogue and moving on to the theoretical underpinnings of form-function models that aid in estimating microvascular behaviour that is downstream of the main coronary arteries, and therefore used to set boundary conditions.

3.2. Theoretical framework

3.2.1. Coronary Artery system

The purpose of simulating blood flow within the coronary artery model is to replicate the flow and pressure within the coronary arteries as FFR requires fluid pressures to be known beyond just the anatomy of the artery. Essentially the coronary arteries can be treated as a set of resistive pipes receives an inflow from the left ventricle, the flow is distributed across its many outlets.

3.2.2. Electrical circuit analogy

A very useful way to look at the circulatory system is to use an electrical circuit analogue [76]. An electrical circuit's voltage or electromotive force, current, resistance and capacitance are analogous to blood pressure, volumetric flow rate, resistance or flow resistance and vessel compliance in blood vessels. An example of this applied to the coronary arteries can be seen in Figure 3-1. As Poiseuille flow is generally applicable to most blood flow, it is useful to compare Poiseuille resistance and electrical resistance (Ohm's law):

$$F = \frac{\Delta P}{R} (3)$$

Where F is the volumetric flow rate, ΔP is the change or drop in pressure across a resistive element and R is the flow resistance.

$$I = \frac{V}{R} \quad (4)$$

Where I is the current (the flow rate of charge), V is the voltage drop across a resistive element and R is the electrical resistance.

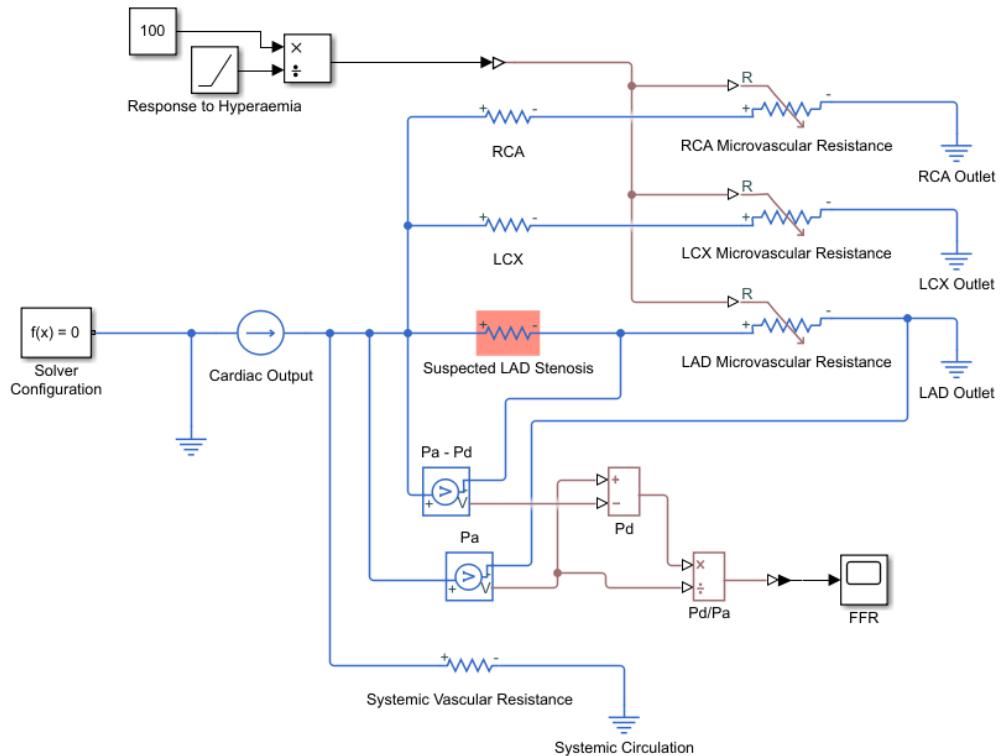


Figure 3-1 Electrical analogue model diagram of a simplified coronary artery system using Simulink. The values P_a and P_d are defined as the proximal coronary pressure and distal coronary pressure, shown in Figure 1-1

Kirchhoff's laws and other principles of electrical circuits similarly apply in an analogous manner: Pressure/Voltage does not change at a bifurcation, but a resistive element will decrease it. The blood vessels themselves act as resistors. Likewise with current/volumetric blood flow is divided at each bifurcation, while the sum flow of a tree/parallel circuit remains unchanged.

In the context of FFR calculations, electric circuit analogy is used as boundary conditions, especially at the outflow of 3D anatomical model. Determination of the model (boundary condition) can be done in two ways, using a geometrical parameter to define the blood vessel tree hence deriving the total tree resistance, or finding flow information at the terminal ends of the vessel using supplementary information such as PET.

Using this simplified electric analogue of the coronary artery tree, the following relationship between the resistances of the stenosis, microvascular resistance, and FFR can be derived.

$$FFR = \frac{Pd}{Pa} = \frac{QR_{micro(Hyperaemic)}}{Q(R_{Stenosis} + R_{micro(Hyperaemic)})} \quad (5)$$

Here the resistance of the stenosis is $R_{Stenosis}$ and the resistance of the microvascular outlet during hyperaemia is $R_{micro(Hyperaemic)}$. Q is the inflow into the artery. As the microvascular resistance decreases during hyperaemia to drive maximal flow, $R_{micro(Hyperaemic)}$ can be expressed as

$$R_{micro(Hyperaemic)} = \frac{R_{micro(Baseline)}}{H} \quad (6)$$

Where $R_{micro(Baseline)}$ is the baseline microvascular resistance, and H is the increased flow proportion during hyperaemia.

$$FFR = \frac{Pd}{Pa} = \frac{R_{micro(Baseline)}}{(HR_{Stenosis} + R_{micro(Baseline)})} \quad (7)$$

This essentially shows that FFR, in a simplified model, is independent of flow, independent of neighbouring vessels, and is purely a function of the resistance of the stenosis (or suspected stenosis), the microvascular resistance and the vasodilatory capacity (the response to hyperaemia) of those vessels.

Whilst this is a heavily simplified model of the coronary artery flow problem, and the electric analog is not always applicable to fluid dynamics behaviours, it is indeed observed in invasive FFR where there is very little

influence of one neighbouring vessel on another, which is why FFR is the gold standard in per-vessel ischaemia analysis.

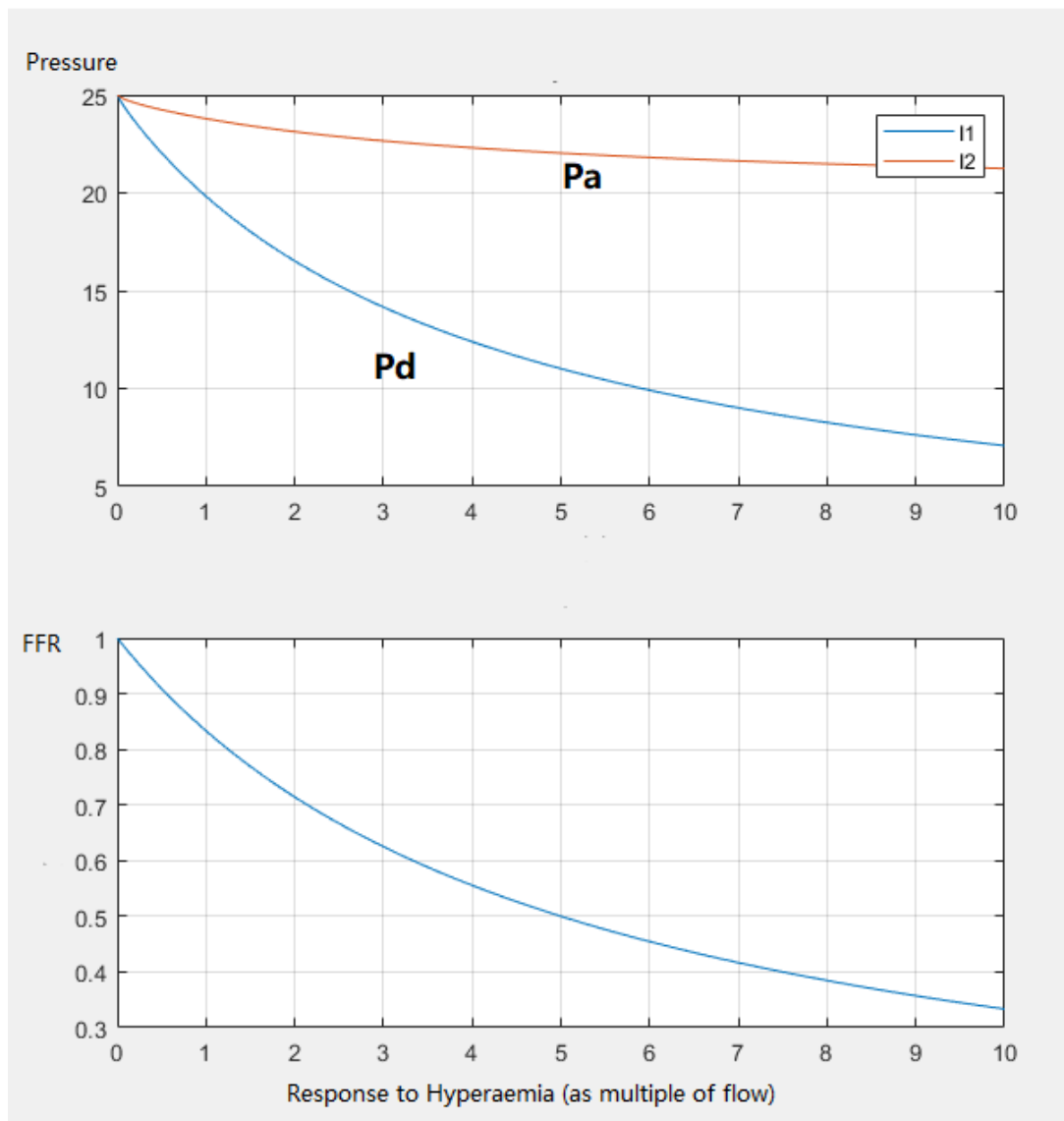


Figure 3-2 (Top) Simulated "pressure" proximal (P_a) and distal (P_d) using electrical analogue model. (Bottom) The relationship between FFR and response to hyperaemia, see equation 7

3.3. Computational Fluid Dynamics Simulations

3.3.1. Navier Stokes equation

The basis of computational fluid dynamic for haemodynamic problems is to solve the incompressible Navier-Stokes (NS) equations numerically for variables p pressure, and \mathbf{u} velocity, at any given point in 3D space and for a non-steady state problem, at any given point in time t . There is the mass conservation equation:

$$\frac{\partial \rho}{\partial t} + \nabla \cdot (\rho \mathbf{u}) = 0 \quad (8)$$

Where ρ is the density of the fluid and \mathbf{u} is the velocity vector. Then there's the Navier-Stokes momentum equation, which can be expressed as the convective form of the Cauchy Momentum equation

$$\rho \left(\frac{\partial \mathbf{u}}{\partial t} + \mathbf{u} \cdot \nabla \mathbf{u} \right) = -\nabla p + \mu \nabla^2 \mathbf{u} + \rho \mathbf{g} \quad (9)$$

Where p is the pressure, μ is the viscosity, and \mathbf{g} is the body force, external forces acting on the fluid such as gravitational.

The left side of the equation is the acceleration $\frac{\partial \mathbf{u}}{\partial t}$ and the convective term $\mathbf{u} \cdot \nabla \mathbf{u}$. On the right side, $-\nabla p$ represents the pressure gradient term, $\mu \nabla^2 \mathbf{u}$ is the diffusion term, and $\rho \mathbf{g}$ is the body force term.

3.3.2. Solution to NS equations

NS equations are highly non-linear partial differential equations and therefore analytical solutions generally cannot be found. Numerical methods are usually used to solve these equations.

The choice of actual numerical methods depends on several conditions of the flow, and typical one being existence of turbulence. Since the Reynolds number of coronary blood flow is generally less than 1000 [77], the flow can be considered laminar hence no turbulence model is needed to describe the flow. In the simulation scheme for this study, the rigid wall assumption is also used.

Currently most commercial CFD applications solve NS equations with either of the three main methods: Finite Element Method (FEM), Finite Difference Method (FDM) and Finite Volume Method (FVM). FVM is the most widely used of the three, and is the method employed in ANSYS CFX, the CFD tool used in this study. FVM calculates the conservation of mass and momentum in every element in the mesh based on the flux of those through the element border. This system of conservation allows the simulation to be performed resource effective, with the benefit from a flexible choice of mesh element (e.g. tetrahedral, hexahedral and prism) that offers the computational mesh well adapts to any geometrical configurations [78].

More specifically in ANSYS CFX, the governing equations are discretised in space using element-based FVM, where volume and surface integrations are performed at the Gaussian integration points on each element/face using tri-linear shape function, interpolating nodal values of velocity and pressure in 3D within each element. The time integration in the computations appear in this thesis was performed using 2nd order backward Euler scheme. Stabilisation of the advection term was achieved by adaptive 2nd order upwinding scheme, in which 1st order upwinding was blended with the 2nd order scheme such that the nodal value of any variable did not exceed the maximum/minimum bounds of surrounding nodal values. For more details, readers are referred to CFX theory manual [79].

3.3.3. Boundary conditions

To numerically solve the NS equations within a control volume, boundary conditions are needed at the borders of the control volume: walls, inlets and outlets

The coronary arteries are a complex system to define boundary conditions for. In most cases the blood pressure at the terminal ends of the arteries, where they meet the myocardium, is unknown. Unlike simpler systems, blood is not simply expelled into a vacuum or atmospheric levels of pressure. Additionally, with the limited resolution of CT images, the total volume of the coronary arteries is truncated, leaving out the smallest blood vessels. To realistically simulate the blood flow in coronary arteries, the boundary conditions need to approximate the effect of the smallest branches and the myocardium.

Lumped parameter models serve to simplify the entire downstream vessel system into one parameter, such as pressure or resistance at the boundary, and often used in blood flow computations [44,80]

3.4. Lumped parameter models

A lumped parameter or 0D model approximates a complex system of blood vessel network into a simple representation that can be integrated to the 3D CFD model as a boundary condition. The simple representation is derived based on assumptions and physical laws known about the system's behaviour. A typical example is that of a circuit of series and parallel resistors, which can be easily lumped together into a single resistor with a certain resistance value. By lumping the resistors into one, the intricacy of the circuit may be lost, but if the parameter representing the downstream circulation is simply the total resistance, the lumped parameter model is sufficient for the problem at hand.

The lumped parameter equivalent for the coronary arteries ideally need to reduce all the microvascular system into a few parameters, which in a fluid dynamics context, are resistances or pressure. Flow resistances can

be summed up similarly to the way how resistances connected in parallel and series in an electric circuit are added up. And there are scaling laws that dictate how arteries branch out, which can be used to define resistance of each branch in the microvascular network.

3.4.1. Murrays Law

Murray proposed that physiological structures such as blood vessels organise themselves following laws of energy minimisation [81][82].

Murray's work focused on oxygen transport in the circulatory system. The cost or inefficiency defined for the blood vessels is represented by the diameter, arguing that smaller vessels require more energy to push the same amount of flow (i.e., transport energy), however a vessel too large will also be a burden as the metabolic/biochemical energy – proportional to the volume of blood – required would be too high. Murray modelled the blood flow in arteries as fluid flow in a tube/pipe, which follows Poiseuille's law [81].

$$p = \frac{q \cdot l \cdot 8 \eta}{\pi r^4} \quad (10)$$

where p is the pressure loss from fluid flow in a given cylindrical tube, q is the volumetric flow, l is the length of the tube, r is the radius of the tube and η is the dynamic viscosity. Multiplying it by the flow, an equation for frictional losses is obtained, measured in energy or work.

$$pq = \frac{q^2 \cdot l \cdot 8 \eta}{\pi r^4} \quad (11)$$

Murray then calculated the cost of maintaining blood volumes in the body. The total energy consists of two cost parts: frictional losses and the energy cost to maintain a blood volume [82].

$$E = pq + bVol = \frac{q^2 \cdot l \cdot 8 \eta}{\pi r^4} + bl\pi r^2 \quad (12)$$

where pf is the frictional losses from fluid flow in a given cylindrical tube, and $bVol$ is the per second energy expenditure for every unit volume of

blood multiplied by the total blood volume in the tube. By differentiating this equation and finding the minima, the cost of operation is minimised, and the relationship between vessel radii and flow can be derived. Using some empirical information to simplify some of the terms, Murray eventually reached the relationship that blood flow was proportional to the cube of the radius of the vessels [82].

$$q = r^3 \sqrt{\frac{\pi^2 b}{16\eta}} \quad (13)$$

$$q = kr^3 \quad (14)$$

[82]. Combining this with volume conservation between parent and two daughter branches through a Y-bifurcation, the relationship between daughter vessel radii and parent vessel radius can be found.

$$r_p^3 = r_{d_1}^3 + r_{d_2}^3 \quad (15)$$

This is called Murray's law and used as the basis of calculating resistance in a lumped-parameter vessel network model.

3.4.2. Structured tree model

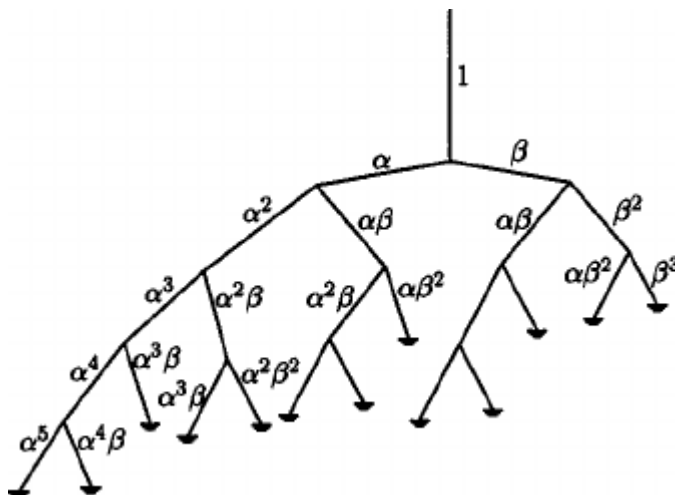


Figure 3-3 Diagram from Olufsen et al[93] showing a structured tree diagram of a root vessel of unit radius, and the radii of subsequent branches. The bifurcation parameters, α and β , are chosen to specify the sizes of the major and minor branch of each bifurcation relative to the parent vessel

Olufsen et al. devised a zero-dimensional structured tree model of blood flow and pressure in systemic arteries. A diagram of the structured tree is shown in Figure 3-3.

The paper starts with the premise that the total cross-sectional area of vessels at the aortic root starts at approximately 5cm^2 and reaches 400cm^2 at the arterioles [83]. At each bifurcation (branching), the total cross-sectional area of the daughter vessels is larger than that of the parent vessel. Although the paper [83] is not specifically about coronary arteries, the model is applicable to this problem.

Olufsen et al assumes large arteries are elastic due to its composition of smooth muscle, collagen and elastin. The elasticity stores pressure energy and releases to flow during diastole. In the paper, the storage and release mechanisms are suggested to even out the flow rate over a cardiac cycle [83].

Olufsen uses a combination of assumptions and empirical measurements to constrain the model. Starting with inflow measurements taken using MRI to create the inflow boundary condition [83]. She also uses the conservation of flow: the sum of flow in daughter vessels is equal to the parent flow as the bifurcation condition [83].

The purpose of the model is to predict outflow boundary conditions given the 3D anatomical model of epicardial arterial tree, considering that the smaller arterioles are a collection of binary and asymmetrically structured trees. The main challenge is that each sub tree has a variable number of generations from the root [83]. To simplify the model further, Olufsen et al assume that the vessels are straight, and higher order terms than those linear to diameter are dropped. This essentially emulates an electrical circuit-like impedance based calculation [83]. The vessels are terminated at a cut-off diameter (e.g. set to 50 microns in [83]), where smaller blood vessels are physiologically unrealistic. However, because of this cut-off, the calculation must be performed numerically. Starting from the terminal ends of the tree, the root impedance for each upper generation (towards the

arterial root) can be used recursively to calculate the total resistance of the tree [83].

An interesting feature of Olufsen's model is that it is self-similar at every generation, similar to a fractal structure. However, it is deliberately asymmetric between each pair of daughter vessels. The ratio between the sizes of each daughter branch comes from the literature of experimental observation, and all subsequent vessels can be calculated just from the ratio and the starting diameter.

They showed that because blood flow can be well characterised as DC current, and therefore there is no phase to consider. The resistance along a vessel segment can be written as:

$$Z = \frac{8\mu l_{rr}}{\pi r_0^3} \quad (16)$$

Where μ is the dynamic viscosity, r_0 is the vessel radius and $l_{rr} = L/r_0$ is the length-to-radius ratio of blood vessel segments [83]. This was found previously to be a constant value of around 50 based on animal studies[84,85]. This means that the flow resistance of a segment can be fully quantified, with only radius measurements, which are inferred in the morphological model. Treating the segments as resistors in an electric-circuit-like network will allow the calculation of the total resistance of an arterial tree.

3.4.3. Windkessel model

The two-element or RC Windkessel model, shown in Figure 3-4, is a 0D hydraulic–electric analogue where vascular resistance and vessel compliance are represented analogous to electrical resistance and capacitance [86,87]. Similarly, flow properties like a pressure difference and mass flow are analogous to a potential difference and electrical current. The downstream boundary condition after the RC component is essentially the venous bed approximated to have zero pressure.

There have been many Windkessel models developed, e.g., the three-element, four-element modified Windkessel and others[87–89]; however, complex models require more parameter estimation for each individual component in the circuit. We chose to use two-element model for simplicity. The limitation of the two-element Windkessel model is its inability to accurately replicate the high frequency component in the pressure waveform during systole, because it is essentially a low-pass filter. However, for the purpose of estimating the behavior in the diastolic wave-free region, the region important for FFR, it has been demonstrated to perform similar to more complex models[87].

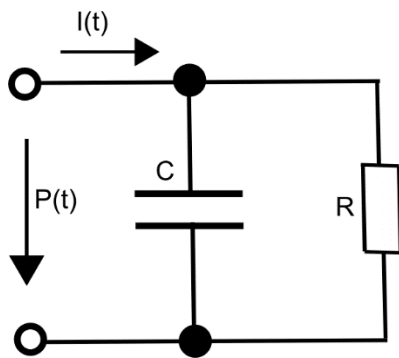


Figure 3-4 2-element Windkessel model in electrical terms. $I(t)$ represent the current, $P(t)$ is the potential difference across the two points, C is the capacitance and R is the electrical resistance.

In Hydraulic analogue terms, $I(t)$ correspond to $Q(t)$, the flow into the system. Electrical resistance R corresponds to the Poiseuille flow resistance, R , of the blood vessel. Capacitance, C , corresponds to the compliance, C , of the vessel. And the potential difference, $P(t)$, corresponds to the pressure change, $P(t)$, over time across the 2-element windkessel system.

3.4.4. Blood properties

The material properties of blood are also relevant in the CFD simulation. Blood is a relatively viscous liquid with its viscosity about 2-3 times that of water. Although blood is known to be a shear-thinning non-Newtonian fluid blood, in coronary arteries it can be considered Newtonian

because its high mean shear rate [90] which has also been demonstrated in the work of Abbasian et al [91]. When approximated as Newtonian fluid, the dynamic viscosity of blood is typically given as 0.003-0.004 kg/mPa · s at internal body temperature (37 deg Celsius).

Unfortunately flow within the coronary arteries cannot be measured directly, as imaging techniques like MRI and PET are too coarse to resolve individual blood vessels. CT imaging is also optimised for structural imaging as opposed to flow. However, it is possible to observe changes in ventricular volume to anticipate the quantity of flow into the body and from that, the instantaneous flow rate can be found, which is the approach taken in this thesis to estimate patient-specific flow condition.

3.5. Anatomic reconstruction of Coronary Arteries

The 3D models used for the CFD were reconstructed using the Simpleware ScanIP software (Synopsys Inc, CA, USA) /Simpleware Ltd (UK). The program is designed to segment, visualise and reconstruct 3D surfaces from a wide range of 2D image stacks.

In this study, stacks of CT images in the DICOM format are imported into the program and a 3D surface model of coronary tree is generated based on the Hounsfield unit representing the tissue in each voxel. The actual procedure is carried out in the following steps (shown in Figures 3-5 to 3-10):

Step 1: The user imports a stack of CT images into the ScanIP software. Then the user selects a part of the CT image, and the software can segment components based on CT Hounsfield units (HU) limits set. This is normally considered as an image segmentation process. See Figure 3-5

Step 2: As the initial flood-fill operation segments out all connected regions having similar HU (due to similar level of X-ray attenuation between bones and CT contrast agent), blood vessels, and ventricles and bones are segmented out all together in the program. After segmentation, a 3D model of a ventricular cavity, the aortic root and the coronary arteries are cropped

out. Because the myocardial muscle normally has a different level of HU from blood cavity, the myocardium is not segmented here as its HU is outside the range to be segmented. See Figure 3-6

Step 3: of anatomical model reconstruction. The user needs to define the terminal ends of the model. While it can be left as is, it is generally good practice to “prune” parts of the mesh which are too small to have been properly resolved in the CT image (Figure 3-8). Vessels in these ends – peripheral regions of coronary vessel network – are usually tortuous, and the polygonisation during segmentation create blood vessels that are physically unrealistic. While the polygon size can be decreased to refine the model surface, there is a limit to how much can be recovered since the CT resolution is the limiting factor. The proximal and distal ends of aorta also need to be defined, preferably perpendicular to the vessel centrelines.

Step 4: Once model boundaries are defined, the ScanIP +FE module fills the vessel cavity with volumetric (tetrahedral and prism) mesh elements so that the model is meshed for CFD. The near-wall (boundary layer) region is filled with prism mesh of small thickness such that the expected steep velocity gradient can be adequately resolved. The final mesh is shown in *Figure 3-9*.

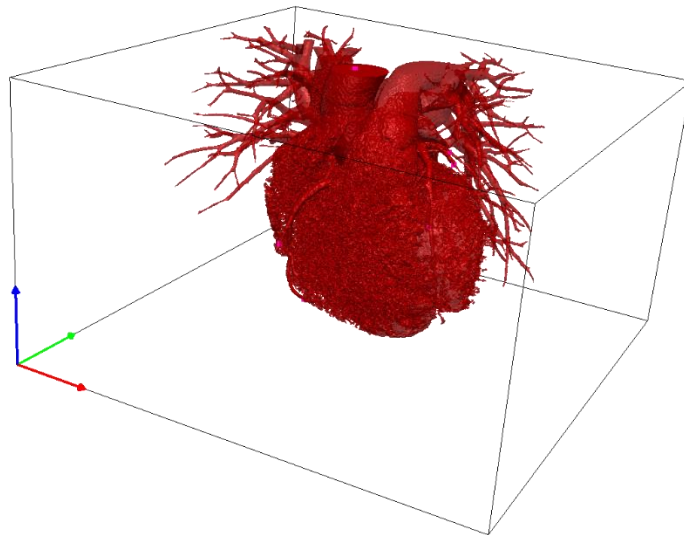
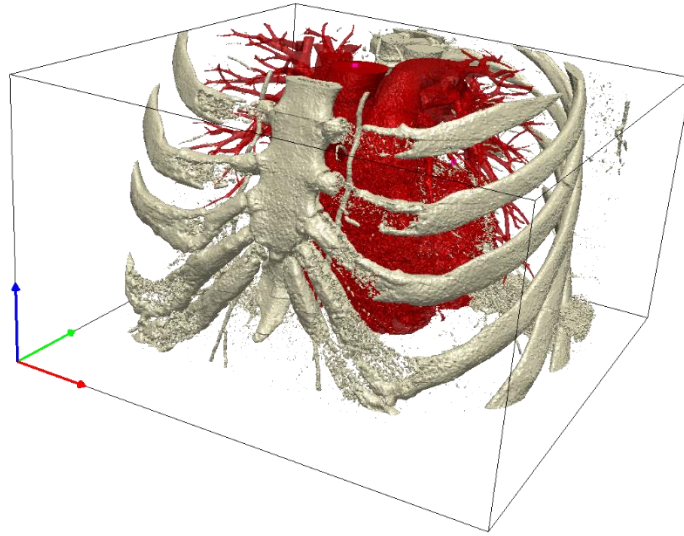


Figure 3-5 (Top Panel) 3D rendering of the segmented Chest CT images, the rib and spine are shown in a bone colour whilst the heart and blood vessels are shown in red. (Bottom Panel) Ribcage and Spine removed leaving just the heart and its blood vessels, e.g aorta, vena cava, pulmonary artery and veins etc.

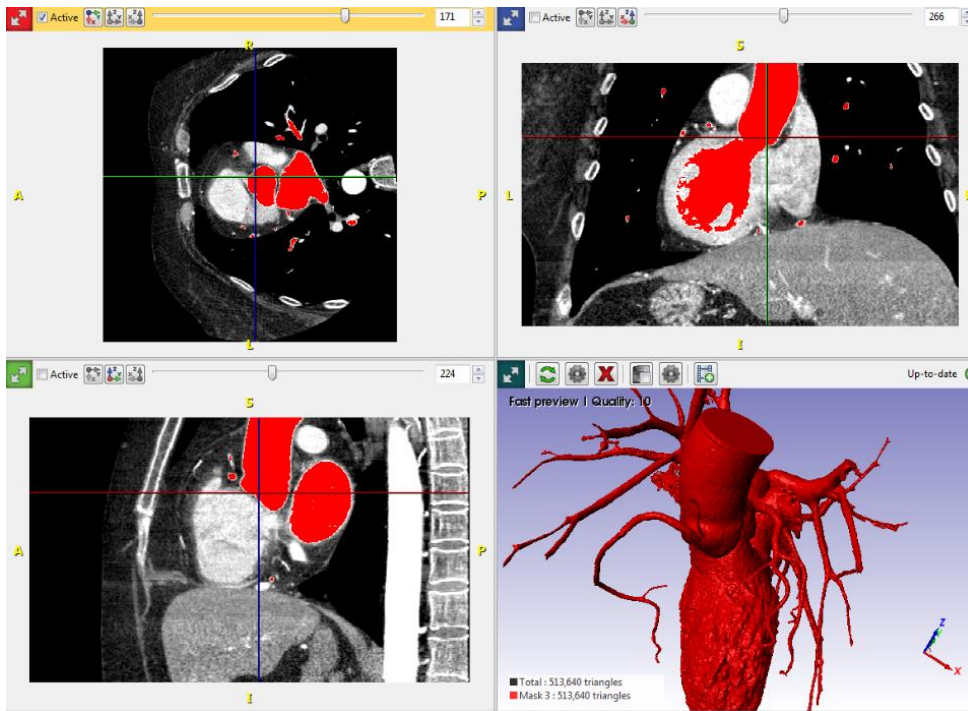


Figure 3-6 User interface of ScanIP software, used in Step 1 of anatomical model reconstruction. In this study, the aortic root and coronary arteries are focused, therefore the HU range needs to be narrow enough to exclude the heart cavity. If there are any remaining unwanted parts that cannot be segmented using the HU range, it can be manually eliminated in step 3.

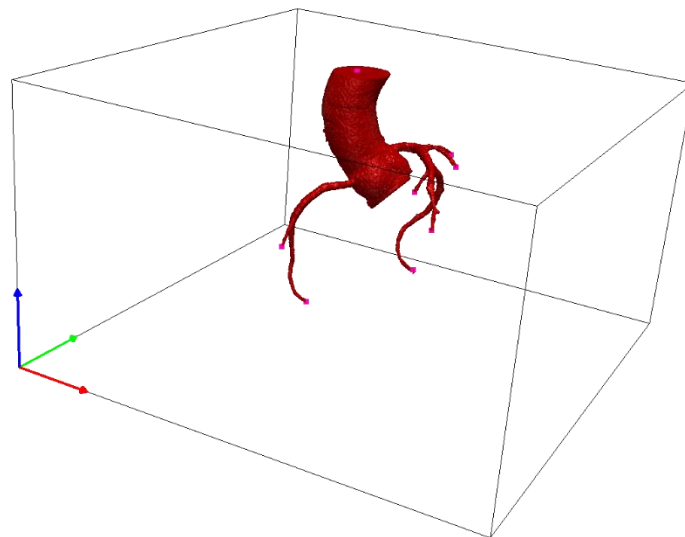
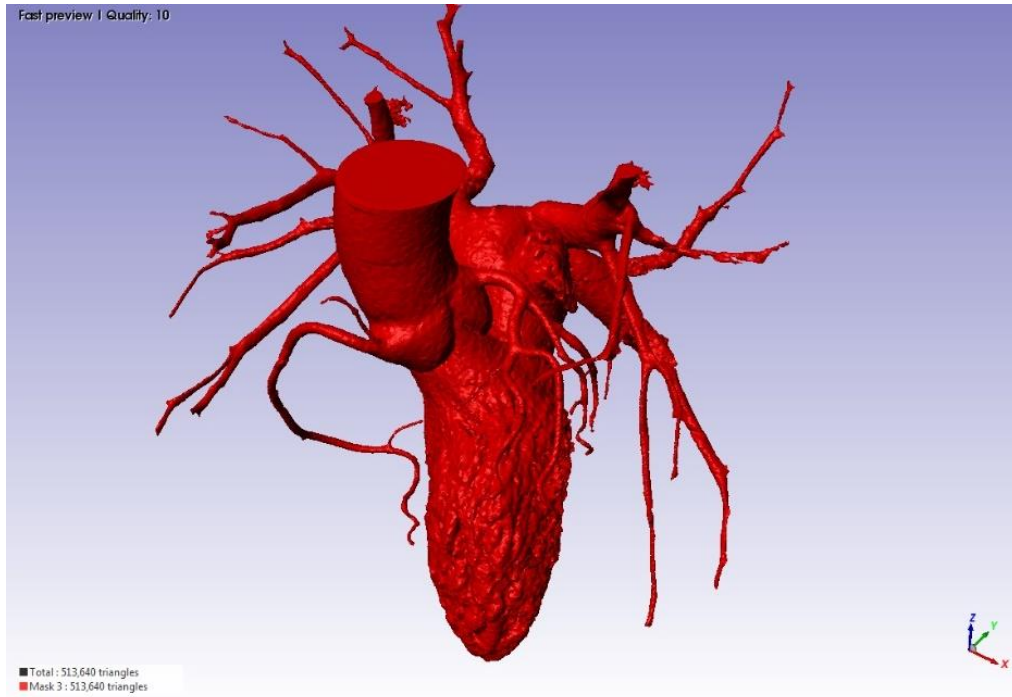


Figure 3-7 (Top) The Aorta and coronary arteries connected to the myocardial cavity. The myocardium is not visible as its HU is outside the range that is being filtered here. (Bottom) Coronary artery segmented from the myocardium

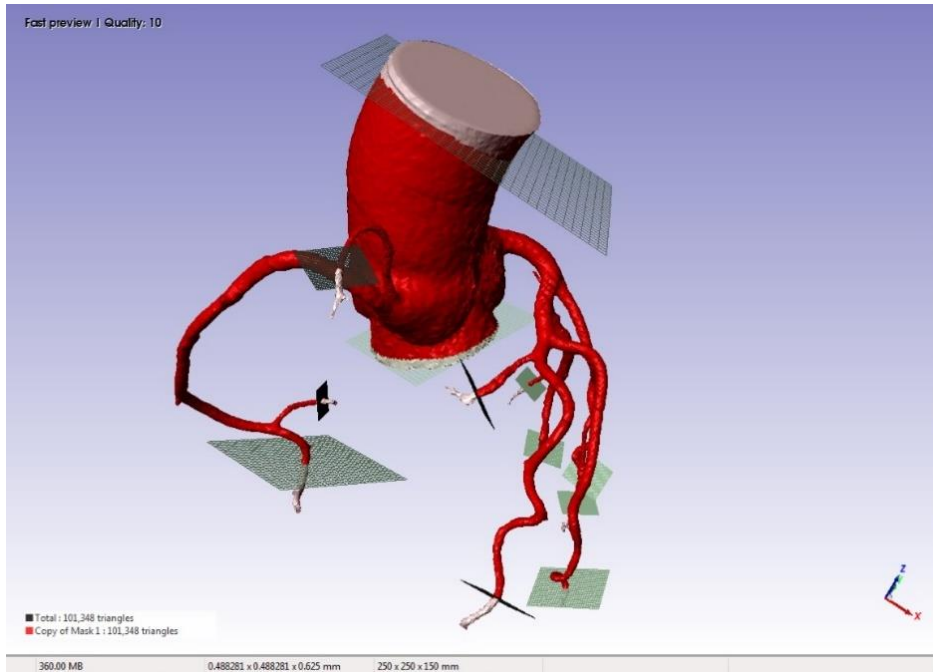


Figure 3-8 Segmented aortic root and coronary arteries with boundaries defined for CFD simulations



synopsys

Figure 3-9 (Top) Example of a completed mesh. (Bottom) Completed mesh zoomed in and oriented to view the cross section of the coronary artery opening. Note the prism layers at the edge.

3.5.1. Mesh sensitivity test

One of the parameters that needs to be considered when creating a mesh from a 3D model is the mesh size. Mesh size is essentially the “resolution” of the model, how many polygons/elements the model is being represented by. A higher mesh size has a larger number of polygons, each of a smaller size, and represents surface curvatures better. A lower mesh size will reduce computational cost during simulations, as CFD generally scales with the number of elements in the control volume. Computations using insufficient mesh resolution would yield unreliable results. To gauge the best “goldilocks” mesh size where the simulation will produce sufficiently accurate results at the lowest runtime, a mesh sensitivity test was performed, shown in Figure 3-10 and **Table 3-1**. Mesh 3 shows similar pressure difference values as the larger meshes, but Mesh 4 appears to have a more consistent pressure value with the rest. Mesh size in mm is effectively the size of the polygons used to represent the 3D model.

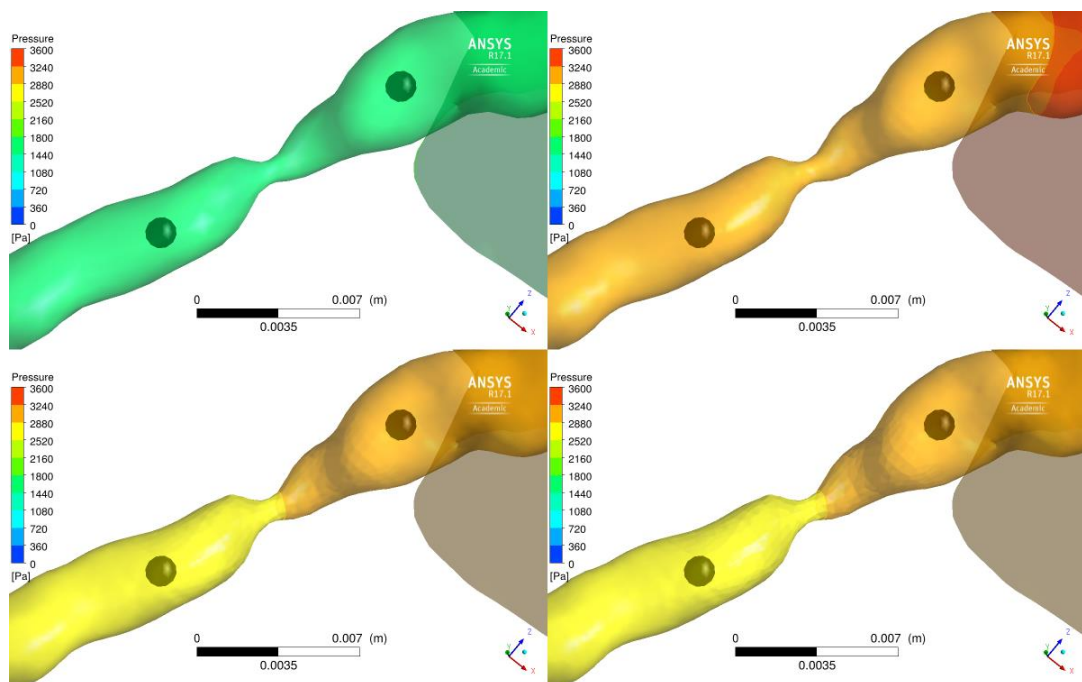


Figure 3-10 A comparison of pressure differences across the same stenotic artery, at different mesh sizes.

Table 3-1 The difference in pressure values calculated in the CFD simulation using various mesh sizes.

Mesh	Element Size (mm)		Number of		Pressures		
	Stenosis	Vessel	Nodes	Elements	Proximal	Distal	Difference
1	1	1	12250	60536	1765.6	1600.27	165.33
2	0.3	0.7	146813	353465	3238.57	3055.75	182.82
3	0.2	0.5	253705	648771	3125.13	2929.24	195.89
4	0.15	0.4	461946	1206400	2994.65	2798.59	196.06
5	0.1	0.3	874547	2719423	2962.55	2768.12	194.43
6	0.075	0.3	989059	2983263	2967.98	2772.75	195.23

3.6. Olufsen model implementation

3.6.1. Structured tree model implementation

The first lumped parameter model is implemented based on the model outlined in the Olufsen [83]

The boundary condition at the terminal end of each coronary artery outlet is an RC circuit with an unknown resistance R and capacitance C. To calculate the resistance first, the hypothetical branching must be developed using the Olufsen structural tree model. The bifurcation parameters, α and β , are chosen to specify the sizes of the major and minor branch of each bifurcation relative to the parent vessel, see *Figure 3-3*. α and β can be equal, but literature cited in Olufsen's model suggested an exponent to Murrays law as 2.76, an intermediate value compromise between 3 for laminar flow and 2.33 for turbulent flow [85,92]. This leads to the daughter radii: α as 0.9 and β as 0.6. This means at every bifurcation; the daughter branches have radii 0.9 and 0.6 times the radius of the parent vessel. This is developed to as many generations as it takes until the largest daughter vessel reaches the minimum terminating radius (where vessels do not realistically get smaller), usually about 50 microns [93]. Each bifurcation can be interpreted as the start of a new generation. The largest daughter branch will be the blood vessel that scales by α at every bifurcation. The daughter vessel generation is terminated when the larger daughter branch radius reaches the cut-off threshold, and generally, for the coronary vessel sizes being considered, the number of generations does not exceed 20.

The algorithm in producing the structural tree model is outlined below:

1. Start with two branches from the CT-based terminal artery radius R , with radii αR , βR
2. Split each of those branches into two daughter branches again
3. Each new branch is α and β multiplied by the radii of the parent branch.
4. Repeat this process starting from Step 2. for 20 generations where you will have 2^{20} terminal branches. Olufsen et al, suggests that 17 generations is sufficient [93], but as long as the same minimum radius is used, a larger generation number can account for a wider range of outlet sizes.

3.6.2. Resistance calculation.

The network can be visualised as a collection of resistors placed in series and parallel to each other, the total resistance of the outlet accounts for the total network geometry. This is achieved by adding resistances recursively from the ends and up the branches.

For the first set of branches, to calculate the resistance, simply use the equation specified in the Olufsen paper to calculate resistance based on the radius of the vessels. For each of the 2^{20} vessels, a corresponding resistance value can be calculated using equation 18.

The resistance calculation algorithm is as follows:

1. Calculate each of the terminal branch's resistance using its radius. For any branch of its radius smaller than the minimum radius (50 microns), set the resistance to 0.
2. Total resistance of each daughter pair is calculated by taking the two daughters connected in parallel. This total resistance is called the downstream resistance.
3. The resistance of the parent vessel is calculated based on its radius.
4. The parent and downstream resistances are summed in series, and this becomes a new daughter branch resistance of the bifurcation one level upstream in the tree.

5. Repeat steps 2–4 until the singular parent vessel is reached thus the total resistance of the tree can be calculated.

3.7. Concluding Remarks

This chapter described the fundamental framework to conduct coronary blood flow simulations using patient-specific anatomical models reconstructed from CT images which is the basis of CT-based FFR computations. The key theory and assumptions involved in the framework was also described. In particular, the methods for defining outflow boundary conditions such as the structured tree method, and assumptions when applying that, play key roles in the model framework. The methods described here will be applied in the subsequent chapters, 4, 5 ,6.

Chapter 4. Examining the Effect of Inflow Conditions in Computational Fluid Dynamics simulation for FFRCT Computations

4.1. Aim

In this chapter, the aim is to investigate the variability of computed FFR when the simulation models are simplified. Firstly, the importance of a pulsatile flow simulation is assessed, replicating the cardiac output from a heartbeat, versus a simplified steady-state simulation in a practical setting where boundary conditions are not fully known a priori. Secondly, the importance of patient specific inflow parameters such as heart rate, stroke volume, blood pressure and flow waveform are examined in comparison to general population average metrics.

4.2. Introduction

Recently, with an increase in the use of computed tomography coronary angiography (CTCA), the determination of FFR has been proposed to utilise coronary CT images and computational fluid dynamics (CFD). A 3D model of the aorta and coronary arteries is segmented from the CTCA images, and the pressure profile across the model can be calculated using CFD. There have been many attempts at simulating the conditions in the coronary arteries, including commercial entities such as HeartFlow Inc. that performs the CT-based FFR analysis for clinical diagnoses. The Heartflow approach has been demonstrated in various clinical trials and studies [70,71,94] and has been accepted for use in the US with FDA approval[95] and UK under guidance from NICE[96]. The challenges that are faced by a technique like CT-based FFR is the availability and quality of input data (parameters), computational time and its accuracy in producing reliable values of FFR.

Despite invasive FFR being the gold standard, it is currently utilised in fewer than 10% of CAD assessments, with CT-based FFR even fewer still [71]. There is significant demand for faster and more automated simulations

with the ultimate goal of on-site calculation of FFR in the matter of minutes or seconds prompting the need for more efficient simulations [97]. Currently, a full 3D transient (or pulsatile flow) simulation can take over 36 h [71] and commercial systems still require 12 - 24 h . The ability to reduce this time to be comparable or faster than an invasive FFR measurement will likely increase the use of FFR-based assessments, in general, due to its lower cost (32% lower cost, HeartFlow Inc. Redwood City, California, US[70]) fewer adverse effects from vasodilators, non- or minimally invasive procedures and less requirement of trained clinical staff to be present to perform the procedure.

There is yet to be solid consensus established for CT-based FFR calculation or coronary blood flow simulation in general, with various research groups using a varied set of patient parameters, boundary conditions and simulation types. For example, in inflow parameters, a successful attempt has been reported only using population average, rather than patient-specific values of cardiac output, heart rate and typical vasodilatory response in the presence of hyperaemia or exercise [98], which raises a question about the value of patient-specific boundary conditions. Coronary artery blood pressure in the distal regions of the vasculature have been characterised well using a steady state simulation with arterial wall assumed to be rigid. The predicted pressure was found to be similar (~1%) to both a pulsatile simulation and invasively measured pressure, though conversely this study relies upon patient-specific inlet conditions that have been measured invasively[99]. It has been demonstrated in a highly controlled simulation, where boundary conditions are known or measured invasively, that the steady-state simulations, pulsatile/transient simulations and measured FFR are close to equivalent, suggesting that transient effects may not be significant[100].

4.2.1. Pulsatile flow vs Steady flow

In the invasive FFR procedure during catheterisation, the pressure proximal to the stenosis and the pressure distal to the stenosis are monitored across multiple cycles spanning minimum 2 min, which are 100–250 full

cardiac cycles depending on the patient [101]. The FFR value is taken as the lowest (most severe) Pd/Pa measured, with the caveat that there are various artefacts that are ignored. This diastolic-quasi-steady state is considered more representative of the vascular resistance [102], and the lowest FFR value measured in this period is normally taken as the single numerical indicator, as the final form of FFR, to be used in diagnoses. Additionally, it has been suggested end-diastolic FFR (dFFR)—FFR measured at end-diastole—is a better representation of flow limitation caused by the stenosis [102,103].

4.2.2. Patient specific input variables

It is also important to consider how variable FFRCT simulation outputs are when population averaged cardiac outputs, heart rates, blood pressures, even flow waveform are used, versus the outputs with patient-specific metrics. For the majority of patients that undergo CTCA, heart rates and blood pressure is commonly documented but cardiac output is not, this can be measured using other imaging modalities, or setting a dynamic CT process to capture the volume of the left ventricle across a cardiac cycle to infer the stroke volume of the heart and therefore cardiac output. All these variables play a role in a pulsatile flow simulation but even in a steady flow simulation, cardiac output and blood pressure can have an immediate impact on the FFR value that is measured.

For the same given patient, considering constant coronary arteries and microvascular resistance, a higher cardiac output will lead to proportionately higher flow, across a resistive “pipe”, i.e., a stenosis, a higher flow will create a larger pressure drop and therefore FFR will be lower (the patient will be diagnosed as a more severe case). Blood pressure also affects FFR, as the pressure drop across a stenosis is only dependent on the flow rate and resistance, the same given pressure drop with different patient blood pressures will create different FFR measurements as FFR is the pressure drop divided by the aortic pressure. Though blood pressure is recorded for every patient, this pressure value is measured on an upper arm using

pressure cuff, also known as Brachial pressure, which is shown to correlate significantly with but not necessarily the same as the Central Blood Pressure[104,105], i.e. the blood pressure in the ascending aorta. This is another consideration worth investigating but is outside the scope of this chapter.

4.3. Methods

The analyses are based on computational fluid dynamics applied to a 3D patient-specific anatomical model, following the steps summarised in Figure 4-1. To investigate the dependency of FFR values on boundary conditions, the inflow conditions were varied in 4 ways: (1) pulsatile patient-specific, (2) steady inflow patient-specific, (3) pulsatile population average and (4) steady inflow population average. Additionally, the same conditions were applied to calculate FFR alternatives such as iFR and baseline Pd/Pa. Details of the procedure in each stage of the analysis are described in the following sections.

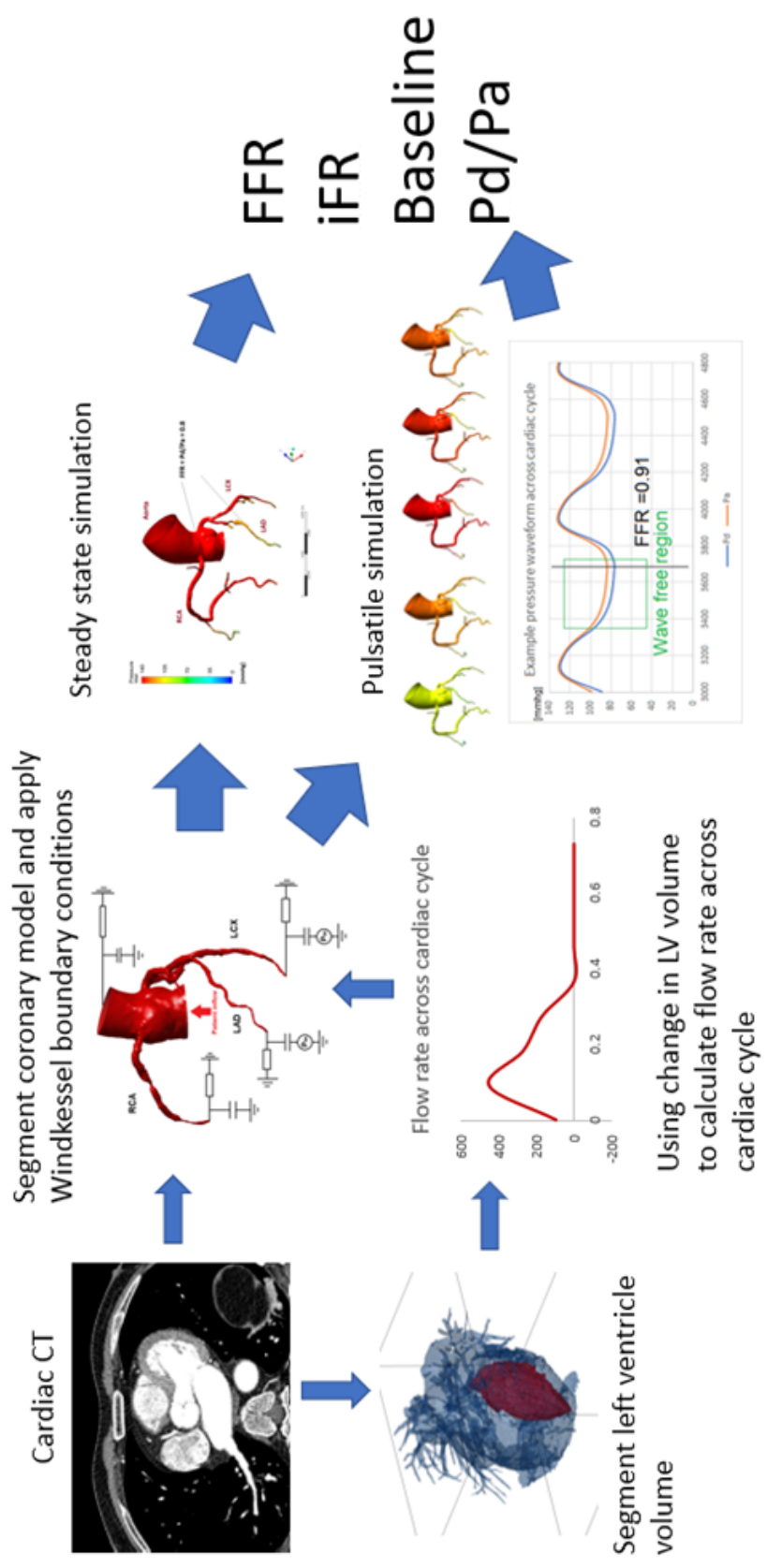


Figure 4-1 Workflow of computational procedure to calculate FFR

4.3.1. Patients

Four patients (2 male, 2 female, age: 58 +/- 6 years) who have various levels of angiographically determined epicardial stenosis (2 mild, 1 moderate and 1 severe case) were selected. The patients, came to UCL Hospital, presented chest pain and other symptoms that indicated an intermediate risk of coronary artery disease. All patients underwent cardiac CT angiography for anatomical assessment. The study was carried out in accordance with the recommendations of the South East Research Ethics Research Committee, Aylesford, Kent, UK, with written informed consent from all subjects. The written consents were obtained in accordance with the Declaration of Helsinki.

4.3.2. Image Segmentation and Meshing

Three-dimensional anatomical models of the coronary arteries were obtained by segmenting the coronary CT angiography images using the Simpleware ScanIP package (Synopsys, Mountain View, CA, USA). Due to the limiting resolution of CT, approximately 0.488 mm per pixel in-plane and 0.625 mm slice thickness, the anatomical model included arteries whose diameter was larger than 2 mm. The 3D anatomical model was meshed using tetrahedral elements with 6 layers of prism elements near the wall. Total number of elements resulted in the order of 10^6 for all patients.

In this investigation, stacks of CT images in the DICOM format are imported into the program and a 3D image of voxels is generated with the Hounsfield unit representing each voxel.

4.3.3. Patient Specific Inflow Boundary Conditions

Retrospectively gated CT was performed/acquired, with the data binned into 10% R–R intervals, to enable segmentation of the LV cavity. Using these CT snapshots, the left ventricular cavity was segmented including its

morphological variation. By calculating the change in volume across each time point, the aortic outflow, which subsequently splits into the systemic and coronary outflow, was calculated as a function of time (Figure 4-2). Here, the flow was assumed to be zero in the diastolic phase of the cardiac cycle after the LV cavity volume started to increase, when the aortic valve is expected to shut. Physiologically, blood flows from the left atrium in this phase, rather than backflow from the aorta thanks to aortic and mitral valves.

For the steady-state simulation, the patient-specific stroke volume was calculated from the difference between the end-diastolic and end-systolic volumes, and combined with the measured heart rate of the patient to obtain their time-averaged flow rate. For the pulsatile flow simulation, the patient-specific flow waveform was used directly as the inflow condition at the aortic inlet.

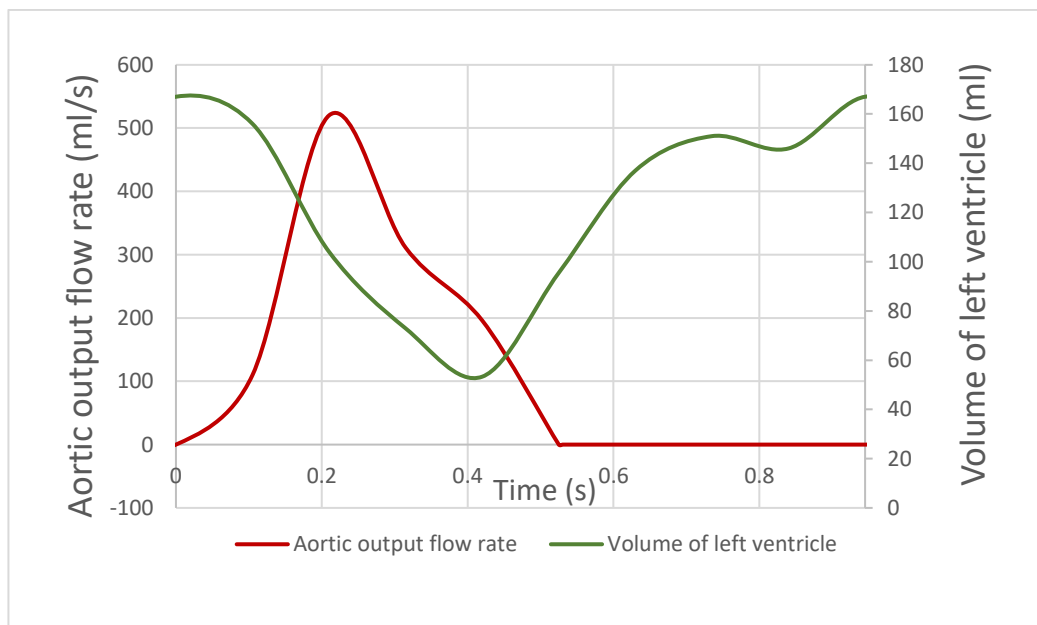


Figure 4-2 Red line indicates the aortic flow rate across the cardiac cycle, derived from the changing volume of the left ventricular cavity contracting and relaxing across the cardiac cycle, shown by the green line.

4.3.4. Coronary Outflow Boundary Condition

As described earlier, the coronary arteries in the anatomical model were terminated at approximately 2 mm vessel diameter, as it approached the limitations of the CT resolution. To incorporate the resistance of further downstream geometry (see Figure 4-3), a structured tree model proposed by Olufsen [93] was used. In this method, the vascular network after the terminal

boundary was modelled with a tree of asymmetric fractal-like bifurcations where each daughter branch of a bifurcation is further divided into asymmetric branches recursively. The method was based on empirical studies on geometry of the coronary microvasculature and had been shown to produce realistic resistance conditions for coronary flow simulations[98].

This process was terminated when the smallest of the daughter branches reached a size that was the limiting size for arterioles—this was 0.05 mm in our model following Olufsen et al. [93]. The resistance of entire tree was calculated and represented the resistance component of two-element Windkessel model, as shown in Figure 3-4. Note that as the simulation is for FFR, they need to be adjusted for adenosine-induced hyperaemia, which is explained in the next section. The capacitance parameter was determined by setting the time constant ($=1/RC$) equal to 0.063 s following the literature[98].

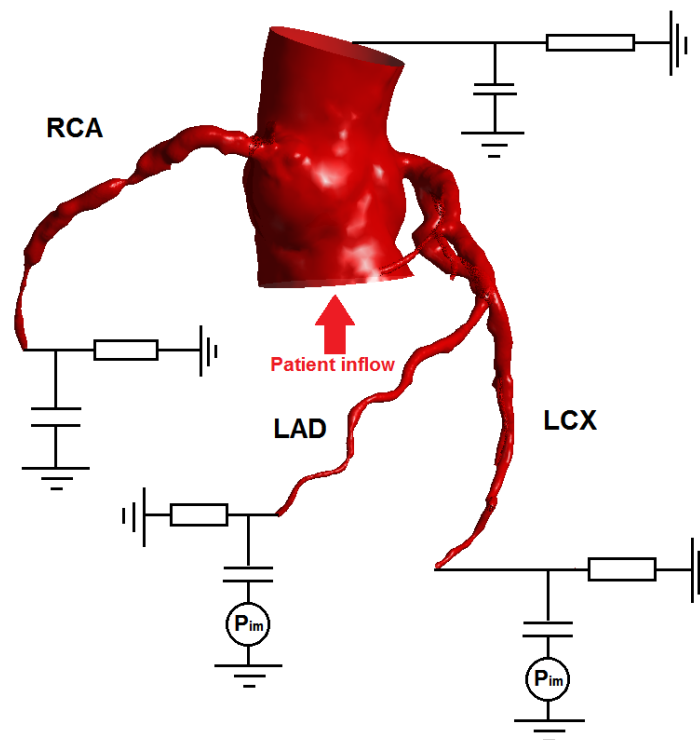


Figure 4-3 Schematic showing various outlet boundary conditions. All the boundary conditions are two-element Windkessel models represented in the circuit diagram. In this patient, both the left anterior descending artery (LAD) and left circumflex artery (LCx) supply the left ventricle, which is susceptible to higher levels of intramyocardial pressure. A pressure term is applied to the boundary condition to mimic the contraction of the left ventricle causing the embedded coronary arteries to be compressed and reduced flow[106]. RCA, right coronary artery.

4.3.5. Aortic Outflow Boundary Condition

The aortic outflow boundary is located proximal to the aortic arch and the flow to this outlet goes to the rest of the systemic circulation. Here, a simple two-element Windkessel model is placed, with systemic resistance tuned to account for 95% of the cardiac output[107] when compared to the resistance values of the coronary outputs.

As the coronary outlet resistances and the aortic outlet are essentially in parallel, it becomes a simple calculation to set the resistance to produce the appropriate flow distribution for a given pressure.

The compliance values were chosen to produce realistic pressure waveforms at the outlet based on appropriate time constants (resistance multiplied by compliance) from literature data[98]. The total resistance of all the outlets—systemic and coronary—was scaled to the patient-specific or population systolic and a diastolic pressure.

It is generally accepted that whilst outlet diameter is a good determinant for downstream microvascular resistance, the microvascular resistance should also be set to produce the appropriate blood pressure given a known inflow, or the appropriate inflow given a known blood pressure. This approach has been used in conventional FFRCT approaches[108], by multiplying the set of microvascular resistances by a scaling factor, therefore preserving the flow distribution across the vessels. When the downstream resistance is adjusted, it has been shown that different methods of resistance calculation tend to produce similar result, especially for functional measures like FFR[109]. For the simulation setup in this chapter, the simulations are conducted with a known inflow (both pulsatile and steady flow), and therefore the resistances are scaled to produce the appropriate blood pressure for the specific patient. Absolute values of resistance derived either by Olufsen[93] and Kassab[110] methods can serve as the starting point of resistance scaling. From this point onwards, the Olufsen structured tree calculation is used as its algorithm has been well validated experimentally[83], used often in FFRCT research[80,109] and its algorithm is easily implemented.

4.3.6. Modelling the Effect of Adenosine

Adenosine induces direct coronary arteriolar vasodilation through specific activation of the A_{2A} receptor. This usually results in a 3.5- to 4-fold increase in myocardial blood flow[13]. Under such hyperaemic conditions, coronary blood flow is directly proportional to perfusion pressure and a reduction in perfusion pressure due to a coronary stenosis will thus proportionally decrease coronary flow during hyperaemia[14].

To model the effect of vasodilation, the resistance values (obtained using the structured tree method) in the Windkessel boundary condition is uniformly decreased to 30% of the resistance at rest; this is a typical adenosine response and used in previous coronary flow simulations[98]. Here, the increase of the flow by adenosine administration from the baseline state ($Q_{\text{adenosine}}/Q_{\text{baseline}}$) is called coronary flow reserve (CFR), indicating the ability of vasodilation in a branch and its downstream vasculature.

Adenosine has also been found to increase the heart rate by 40–50% of baseline[111,112] as well as stroke volume to a much lesser extent (by approximately 10%[113]), ultimately increasing the average cardiac output. The patient parameters in this study had their heart rates and blood pressures measured already during adenosine-induced hyperaemia, there can be used directly. Similarly, for the population average example, Population average haemodynamic parameters (heart rate, etc.) for patients under hyperaemia were obtained from population average baseline cardiac statistics[114,115][111,112], and the typical adenosine response was applied as mentioned above[112,113], these are presented in Table 4-1.

4.3.7. Modelling Intramyocardial Pressure

Pressure and flow waveforms in coronary arteries are out of sync, i.e., the flow is not systolic-dominant, in the coronary arteries which is strongly influenced by the intramyocardial pressure. Intramyocardial pressure is assumed to be purely dependent on and linearly proportional to left ventricular pressure[116,117], and left ventricular pressure closely traces aortic pressure during systole but drops down to nearly zero during diastole. In our model, an

intramyocardial pressure was incorporated as the surrounding pressure across the capacitive component of the Windkessel model boundary condition, as indicated in Figure 3-4, in the coronary arteries that supply the left ventricular muscle. This practically mean that the condition was applied primarily to the main branches of the left anterior descending artery (LAD) and left circumflex artery (LCx). Due to lack of patient-specific ventricular cavity pressure, the intramyocardial pressure waveform from the literature was adopted and scaled to patient-specific systolic pressure, while the diastolic pressure was kept zero [118].

4.3.8. Computational Schemes and Parameters

The time step for pulsatile/transient simulations used was 0.001 s, and the convergence criteria for the linear iterative solver was set to 1.0×10^{-5} based on the root-mean-square of the residual at every node. Pulsatile simulations required 3 cycles before it stabilised to a consistent waveform, and therefore all simulations were performed up to 5 cycles. The actual time of simulation and total number of time steps varied between patients, as their heart rate determined the length of the simulation. The steady inflow simulations were carried out in quasi-steady condition, i.e., transient simulations were conducted with the steady inflow boundary condition. This was required to account for the transient response of the downstream impedance. Here, the same time steps (0.001 s) and convergence criteria (1.0×10^{-5}) as the fully transient simulations were used. Sensitivity tests of the computational results to both mesh and time step size were carried out such that the pressure drop across a stenosis computed with the finally chosen mesh and time step was less than 1% of difference compared to a mesh with doubled number of elements. Computations were conducted using 2 cores on standard desktop workstations (Intel Core i7 6700K 4 GHz, 16 GB RAM, 4 cores and Intel Xeon E5-2670 2.6 GHz, 128 GB RAM, 32 cores).

4.3.9. FFR quantification position and interpretation

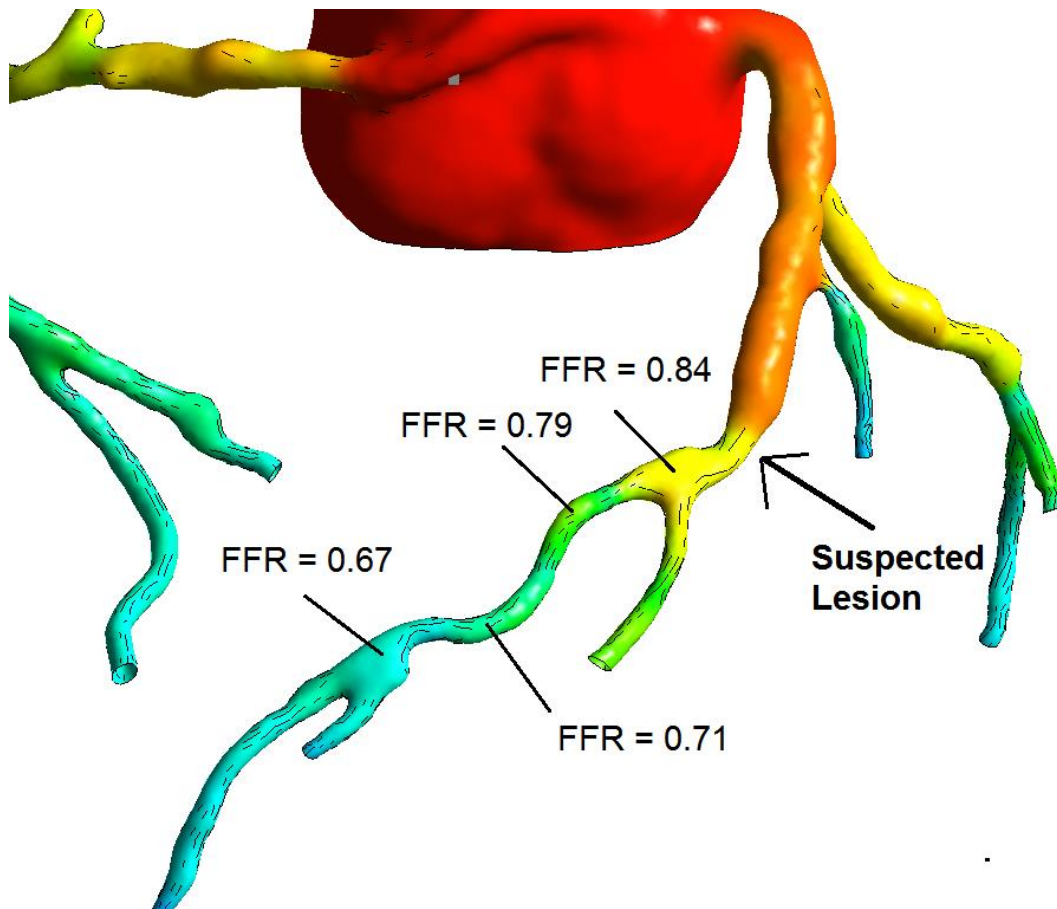


Figure 4-4 FFR values measured across various distances from the locus of the stenoses.

In the results of CFD simulations, FFR values were “measured” by recording pressure values proximal and distal to a stenosis. For simplicity, this calculation – virtual measurement – will be called simply “measurement” hereafter.

In some cases, the pressure drop is much more diffuse over a stenotic artery, like the example in Figure 4-4, making measurement of FFR ambiguous. There is no general guidance for both invasive FFR measurements nor conventional FFRCT, on what location to measure FFR from. FFR standards in invasive measurements specify at least 3-4 cm distally [40][119]. A further point of consideration is that a diffuse pressure drop may suggest that the overall pressure drop is not caused by, or not solely caused by the stenotic segment, but rather by other forms of disease:

microvascular disease, diffuse atherosclerosis, endothelial damage, low coronary flow among many other possible causes. In such a case, PCI or stenting could be ineffectual if not counterproductive to the patient[75].

The HeartFlow Inc service simply returns an FFR profile, essentially the pressure profile divided by the aortic pressure at the coronary ostia, that allows quantification and visualisation of the computed FFR at any point along the coronary arteries[120]. It is then up to the discretion of the physician to decide the FFR at which point to take.

In the present simulations, monitor points were placed at the coronary ostium and in the coronary artery at a point approximately 4 cm distal to the stenosis. In the steady inflow simulation, the pressure ratio of the two points when the simulation had stabilised and converged was used to represent FFR. In the pulsatile flow simulation, pressure values at each monitor point were recorded across the cardiac cycles to calculate FFR (*Figure 4-5*). FFR was taken as the lowest value measured (i.e., the most severe measure) following common clinical practice[121]. FFR of less than 0.8 is deemed as a physiologically significant stenosis that should be best treated by stenting.

4.3.10. Instantaneous Wave-Free Ratio measurement

The instantaneous wave-free ratio or iFR was similar to the pressure ratio across the stenosis; however, it is measured during rest (no induced hyperaemia), and it is the average value across the “wave-free” region of the cardiac cycle, where the competing forces of aortic compression and microvascular compression were minimal and where pressure and flow became linearly related (*Figure 4-5*). In this region, vessel resistance was at a minimum and stable throughout. The cutoff threshold of iFR indicating significant stenosis was <0.89 [55].

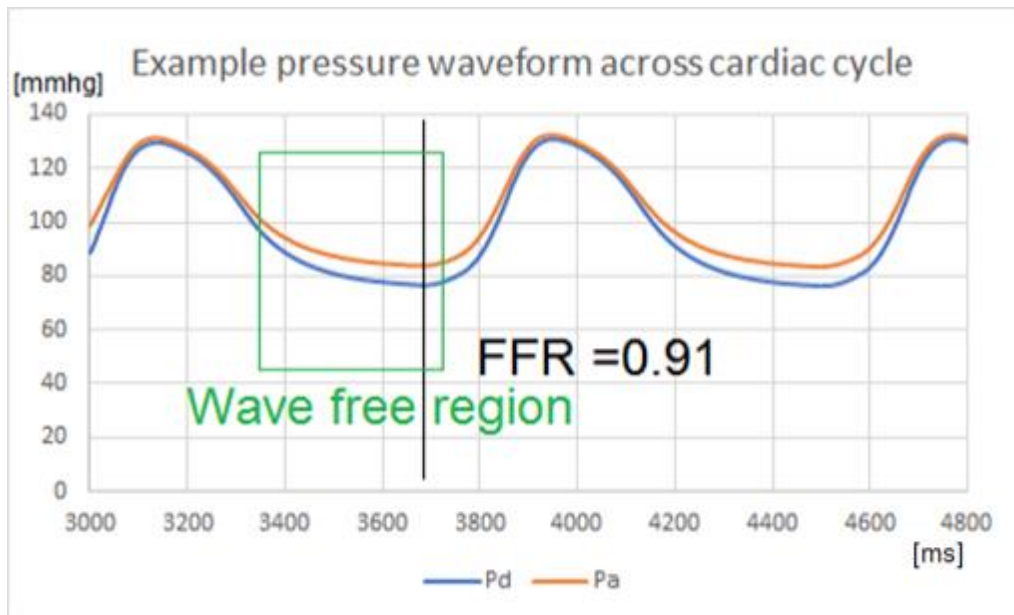


Figure 4-5 Pressure waveform of a patient under induced hyperaemia, showing the pressure at the coronary ostium (P_a) and pressure distal to an obstruction (P_d) across the cardiac cycle. Fractional flow reserve (FFR) is measured as the lowest ratio P_d/P_a measured. Note that there is a region in diastole known as the wave-free region, where the gradient of both pressure and flow are aligned and peripheral resistance is minimized. This is when the pressure drop is usually the most prominent across an obstruction. Instantaneous wave-free ratio (iFR) is measured in that region if the patient is at rest[122].

4.3.11. Comparison of Patient-Specific Parameters and Population Average-Based Inflow Parameters

Simplification of models by using population average data for boundary conditions is a widely accepted approach. While that may not reduce the simulation, time required to produce FFR values, it reduces the burden on clinicians to record every patient-specific parameter for each individual patient. Adequate level of patient information must be thoroughly investigated by assessing whether the pressure profile and FFR is sensitive to patient specificity in the inflow parameters and in what cases might this cause a significant discrepancy. The population average data under induced hyperaemia[114,115] is listed in Table 4-1.

Table 4-1 Patient-specific and population average inflow parameters during hyperaemia. Note: the heart rate is elevated due to adenosine administration.

Patient	Heart Rate (bpm)	Pressure (mmHg)	Stroke Volume (mL)	Cardiac Output (mL/min)
1	106	114/68	98	7200
2	79	140/58	114	9000
3	99	108/46	68	6800
4	115	128/68	103	11800
Population average [115,116]	98	122/71	77	7500

4.4. Results

Spatial distributions of pressure obtained from the patient-specific CFD simulations of patient 2, with steady patient-specific inflow and with pulsatile patient-specific inflow, are shown in **Figure 4-6** and **Figure 4-7**. The pulsatile simulation result is also accompanied by pressure waveforms in the coronary ostium (P_a) and distal to the stenosis (P_d). Comparison of the two series of the results shows that the pressure distributions are similar in general. In particular, the distribution with steady inflow and that with the pulsatile inflow at $t = 0.2$ s appear to be close to each other. In both steady and pulsatile inflow cases, a significant pressure drop is observed across the stenosis (red-orange-yellow in the **Figure 4-6**). It is also important to mention that the pressure difference across the stenosis (P_d vs P_a) is nearly constant from the peak flow (~ 0.4 s) to the end of the cycle in **Figure 4-7**. Note that in **Figure 4-5** and **Figure 4-7**, the proximal–distal pressure difference is larger in the diastolic period. This is because of the diastolic dominant flow in coronary arteries, shown in **Figure 4-8**.

The impact of the type of inflow boundary conditions—pulsatile, steady, patient-specific and population average—on FFR was examined first. **Table 4-2** the result of computations for all four patients and four inflow conditions, in terms of FFR values in various definitions. Note that the conditions of the FFR computation in the present study are all hyperemic, which is required for the measurement of FFR. The FFR are, in general, nearly independent of the boundary conditions for patients 1–3 (approximately 0.6, 0.8, 0.95, respectively) but more variable for Patient 4 (range 0.84–0.94). From the direct comparison between pulsatile and steady conditions for each patient, the maximum discrepancy of FFR due to flow pulsatility is 0.02 for Patient 2. Likewise, the maximum discrepancy of FFR owing to the difference between patient-specific and population-averaged conditions is larger, 0.07, for Patient 4.

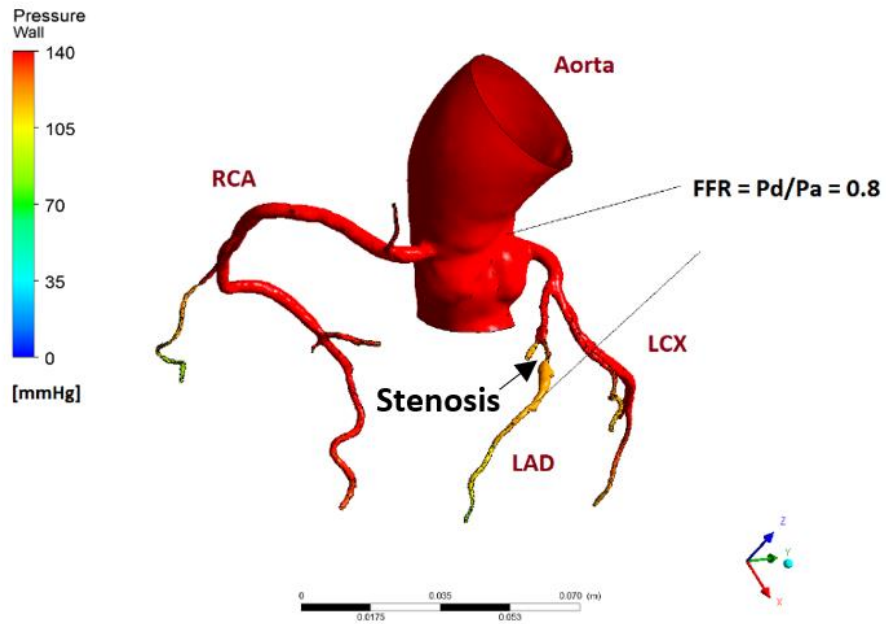


Figure 4-6 Pressure profile of patient 2 with an obstruction in the LAD. At 0.8 FFR, this patient is in the borderline area where stenting is only marginally better than optimal medical therapy. This pressure profile is obtained from the steady inflow simulation.

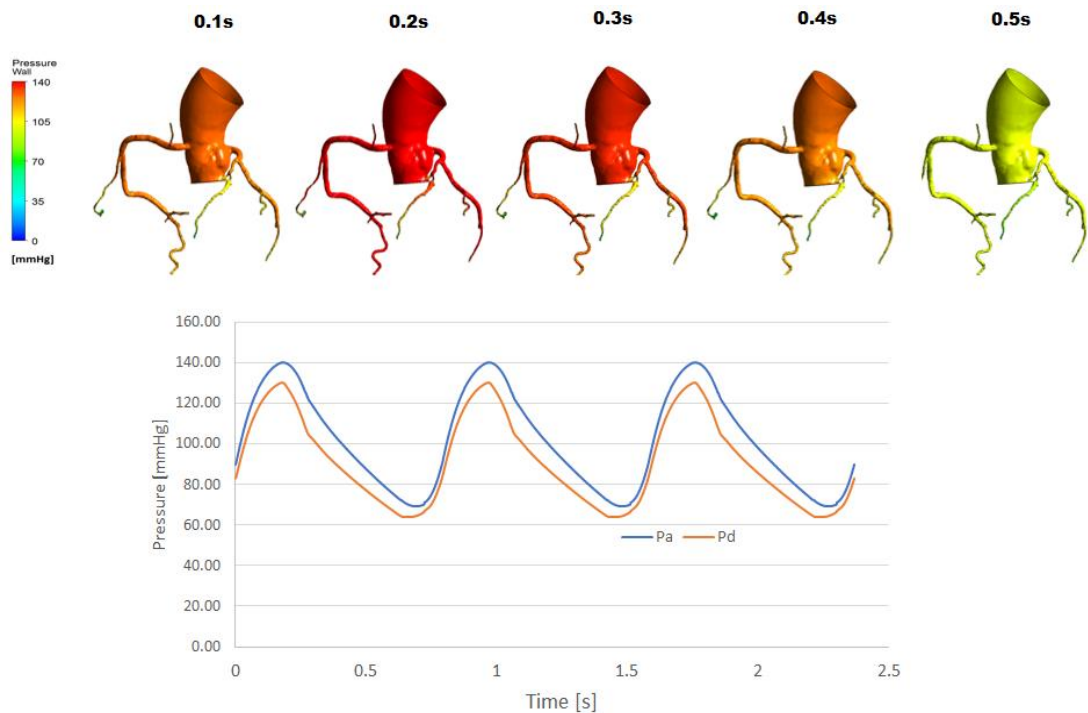


Figure 4-7 Pressure profile of the same patient as Figure 4-6 for a pulsatile flow simulation. The stenosis is located on the LAD. In the time history of pressure, result from the last 3 cycles is shown.

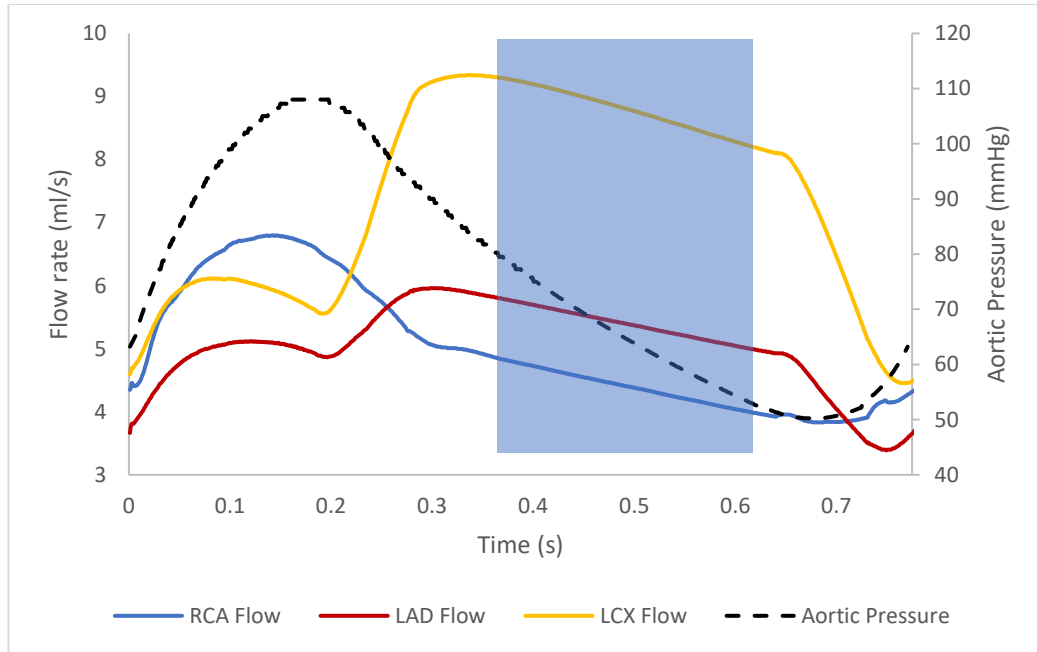


Figure 4-8 Flow rates of the various coronary branches across the cardiac cycle. In the left coronary arteries, flow is the highest during diastole due to high intramyocardial pressure during systole inhibiting flow. Note that there is a stenosis in LAD of this patient. The highlighted region (Blue) shows the diastolic wave-free region, where flow and pressure decline together [55, 123].

Table 4-2 Comparison of pressure ratio/FFR values obtained using various types of simulation.

Patient	With Patient-Specific Inflow				With Population Average Inflow			
	Pulsatile Average Pd/Pa	Puls. End-Diastole (dFFR)	Puls. Min (FFR)	Steady State (FFR)	Puls. Average Pd/Pa	Puls. End-Diastole (dFFR)	Puls. Min (FFR)	Steady State (FFR)
1	0.63	0.59	0.59	0.60	0.62	0.59	0.59	0.59
2	0.84	0.81	0.80	0.80	0.85	0.81	0.80	0.81
3	0.96	0.94	0.94	0.95	0.97	0.96	0.95	0.96
4	0.88	0.84	0.84	0.86	0.94	0.91	0.91	0.92

Next, the impact of hyperaemic conditions on the flow reserve indicators were studied, including iFR—an indicator based on the non-hyperaemic condition. The comparison of various flow reserve indicators is presented in **Table 4-3**. Here, all indicators are based on the pressure drop across the

stenosis and the difference between those in the baseline and hyperemic conditions are shown. Because FFR by definition requires hyperemia, non-hyperaemic (baseline) pressure drop is shown as Pd/Pa —ratio of the pressure downstream of the stenosis to the aortic pressure. The results were derived with patient-specific flow conditions. The pulsatile FFR was calculated as the average of Pd/Pa throughout the cardiac cycle, whereas iFR was only in the wave-free (diastolic) region. The hyperemic indicators are consistently lower than the baseline ones, and the indicators agree with one another within each category. This is also in agreement with the difference of cutoff values of the haemodynamic indicators: lower cutoff value of FFR (0.80 [47,124]) in comparison to baseline indicators (e.g., 0.91 for iFR [123]). Among the patients in this study, consistent with the FFR below the cutoff, Patient 1 appears to have a severe stenosis indicated with both baseline Pd/Pa and iFR below their respective diagnostic cutoffs (0.91 and 0.89). The patients with the higher FFRs also had baseline Pd/Pa and iFR well above the cutoffs, indicating good diagnostic agreement in the two metrics.

Lastly, the distribution of the flows to the stenosed coronary branch and the other non-stenosed branches were investigated under the various inflow boundary conditions. The results are summarised in **Table 4-4**. The flow rates through the stenosed branches are closely matched between the two simulation types while the difference in the healthy branch flows tend to be higher. The largest discrepancy in stenosed branch flow rate between pulsatile and steady flow conditions was observed in Patient 3 (2.18 mL/s versus 1.83 mL/s). At the same time, Patient 3 has the highest FFR (i.e., least functionally severe stenosis) and, therefore, it is likely that the pressure drop across the mildly stenosed branch is not affected by the difference of the flow rates.

Table 4-3 Comparison of pulsatile FFR, iFR, resting Pd/Pa, steady-state FFR and resting Pd/Pa. Simulations were done using patient-specific inflows.

Patient	Hyperamic Indicators		Baseline Indicators		
	Pulsatile FFR	Steady-State FFR	Pulsatile iFR	Pulsatile Baseline Pd/Pa	Steady-State Baseline Pd/Pa
1	0.59	0.60	0.85	0.88	0.85
2	0.80	0.80	0.93	0.94	0.92
3	0.94	0.95	0.98	0.99	0.98
4	0.84	0.86	0.95	0.96	0.95

Table 4-4 Comparison of flow rates out of stenosed and healthy branches, pulsatile versus steady. Simulations were done using patient-specific inflows.

Patient	Stenosed Branch Flow Rate		Healthy Branch Flow Rate ¹	
	Pulsatile Inflow ² (mL/s)	Steady Inflow (mL/s)	Pulsatile Inflow ² (mL/s)	Steady Inflow (mL/s)
1	4.44	4.28	14.3	11.6
2	1.18	1.15	14.6	11.0
3	2.18	1.83	11.6	9.10
4	5.74	5.59	20.8	18.6

¹ Sum of flow out of branches that are not diseased; ² instantaneous flow rates measured at the time point of FFR measurement.

4.5. Discussion

4.5.1. Effect of Flow Pulsatility on FFR

The high correlation between the FFR values obtained using a pulsatile simulation and that of a steady-state simulation indicates that the use of simple steady flow condition may be acceptable. Across the range of coronary artery stenosis from healthy to significantly diseased, the discrepancy of FFR between the steady state and the pulsatile simulation is small (maximum discrepancy of 0.02). This remains true for diseased LAD and LCx arteries, where the systolic–diastolic discrepancy of the flow is particularly high due to its higher impact of intramyocardial pressure that inhibits relatively low level of systolic flow.

The cycle averaged Pd/Pa ratio from the pulsatile flow simulation is naturally higher than the FFR because of its definition, i.e., FFR is the smallest Pd/Pa throughout the cycle. However, dFFR is not necessarily the smallest FFR, although it tends to approximate closely to FFR. The minimal pressure ratio is almost always found in the wave-free region and usually at the end of diastole. This is well explained by the fact that the downstream microvascular resistance is stable and minimal in the wave-free region [55], therefore inviting high flow rate that results in a much larger pressure drop in the epicardial stenosis.

The steady-state FFR values are more closely aligned with the standard FFR as opposed to the pulsatile average despite both simulations having the same average flow rate/cardiac output. Referring to the flow distributions (**Table 4-4**), the flow in the stenosed branch seems not sensitive to the difference between steady and pulsatile conditions, relative to the non-stenosed branches. This indicates that a stenosis is likely to cause redirections of flow to the healthy branches, which make it less sensitive to fluctuations in inflow. This is also consistent with the waveforms presented in Figure 4-8; the flow in the stenosed branch (LAD) varies less than the healthy branch (LCx).

Additionally, when iFR as well as baseline Pd/Pa in the pulsatile simulation are compared with the steady-state baseline Pd/Pa , the steady-

state Pd/Pa tends to be closer in approximating iFR than the cycle-averaged pulsatile baseline Pd/Pa . It is most apparent in the case of Patient 1 where the discrepancy between cycle-averaged pulsatile baseline Pd/Pa and pulsatile iFR is the largest. This suggests that the steady inflow simulations in both resting and hyperaemic states may tend to be more representative of the conditions in the wave-free region of the cardiac cycle. The wave-free region is defined as the time interval within the cardiac cycle where pressure and flow are linearly related [55]. In a steady inflow simulation, the pressure and flows converge to a static value, therefore satisfying this condition. This would also suggest that in a pulsatile simulation that perhaps rather than the average Pd/Pa , the value in the wave-free region should be used.

Steady-state simulations would not be the replacement to pulsatile simulations in all coronary flow simulations; however, there is much value in using them when the focus is on studying the flow limiting effects of a coronary obstruction. It is far simpler to simulate, with less input parameters and therefore assumptions needed and completed in a much shorter time. The computational time was approximately 2 hours for the steady-state simulation, whereas a pulsatile simulation that observes 5 cardiac cycles required approximately 16 hours. Using steady-state simulations may vastly improve the efficiency of blood-pressure-focused coronary haemodynamic research and medical diagnostics, especially when a larger population is looked at.

4.5.2. Importance of Patient Specificity in Inflow Parameters

The largest discrepancy of FFR between patient-specific and population-averaged inflow was observed for Patient 4, approximately 7% larger in the population average simulation than with the patient's own inflow parameters. The largest disparity between the patient-specific inflow parameters and population-averaged was indeed in Patient 4 (Table 4-1); the patient-specific cardiac output, heart rate and stroke volume are all universally higher than that of the population average. The lower FFR (i.e., less functionally normal) in Patient 4 is found with patient-specific inflow in both pulsatile and steady-state simulations; therefore, the likely cause of the FFR discrepancy is the

cardiac output, a combination of increased heart rate and/or high stroke volume. Patient 4's cardiac output is 1.9 times as large as the population average. Using patient-specific inflow, the flow diverted to the stenosed branch is about 1.7 times (5.6 mL/s versus 3.3 mL/s) more than using population average inflow. The discrepancy between the inflow difference ($\times 1.9$) and the stenosed branch flow ($\times 1.7$) suggests that the stenosis redirected the increased flow more to healthy branches.

Using the equation for laminar flow resistance: $Q = \frac{\Delta P}{R}$, where Q is flow rate, ΔP is pressure drop and R is vascular resistance, a higher flow rate should lead to a proportionately higher pressure drop for the same coronary artery system having the same vascular resistance. With the systolic and diastolic pressures comparable between patient-specific (128/69) and the population average (122/71) conditions for Patient 4, it is reasonable to interpret that the pressure drop difference is owing to the flow rate difference between the patient-specific and population average inflows (i.e., patient-specific is 1.7 times higher). This is indeed true as the FFR for the patient-specific case indicates a pressure drop of approximately 1.75 times larger than that of population average. However, the definition of FFR ($Pd/Pa = (Pa - \Delta P)/Pa$; ΔP is the pressure drop across the stenosed vessel) reduces the impact of pressure drop, which is why the discrepancy in inflow conditions are not reflected to FFRs. At the same time, the flow in the branches is clearly sensitive to the inflow condition, which indicates that if the focused parameter is not FFR but shear stress, impact of inflow conditions would be more significant.

It has been documented that FFR is related to the relationship between coronary artery lumen volume (V) and left ventricular mass (M). Left ventricular mass is linearly correlated with left ventricular chamber volume (volume/mass ratio $0.80 \text{ mL/g} + 0.15 \text{ mL/g}$) [125]. Low V/M ratio indicates that a small lumen volume is available for large blood demand (i.e., large volumetric flow) for a large ventricular mass, thus a lower V/M ratio tends towards a lower FFR (high pressure drop) and higher overall likelihood of CAD [126]. It has also been suggested that an obstruction in a small coronary

artery lumen volume is likely to cause ischaemia, and more so for a larger LV mass that demands a higher volume of blood[126].

4.5.3. Various Definitions of Flow Reserve Parameters

The various definitions of FFR and metrics alternative to FFR —for gauging physiological severity of an obstruction—fundamentally evaluate the pressure ratio Pd/Pa in various definitions, each of which has its own merits. The main advantage of iFR, or baseline/resting Pd/Pa , lies in its measurement procedure, i.e., the intravascular pressure measurement is free from adenosine. From a simulation perspective, it may seem irrelevant; however, setting microvascular resistance and appropriately determining its response to vasodilatory drugs as the coronary outlet conditions is crucially important, although acquisition of such data in patient-specific manner is a challenge. It has been reported that coronary artery haemodynamic simulations are particularly sensitive to their outlet conditions [71,99]. While a typical adenosine response is often used, e.g., reduction of peripheral resistance to 30% of baseline, the response in reality is highly variable and more importantly, diseased patients' vasodilatory response is typically less than optimal. Therefore, using an adenosine/vasodilator-free method even in simulation is expected to provide a substantial advantage by potentially reducing the unknown.

Among the patients examined in this chapter, Patient 2 is a borderline case according to the FFR; both pulsatile and steady-state simulations gave a value of 0.80–0.81, which is right at the cutoff for stenting treatment. On the other hand, the baseline Pd/Pa for both pulsatile and steady-state simulation (0.92 and 0.94) indicate that they are both above the optimal cutoff of 0.91 [55] for determining a significant stenosis. Similarly, the iFR obtained from measuring the Pd/Pa ratio at the wave-free region (0.93) indicates that the stenosis is not severely flow limiting, using the iFR cutoff of 0.89. Adenosine-free methods such as iFR and baseline Pd/Pa is not only beneficial for invasive assessment but could also be beneficial in simulation-based assessment of coronary artery disease. As mentioned in the introduction, a hybrid approach using multiple flow reserve parameters (e.g., FFR and iFR)

has been considered. The results demonstrate that computationally derived flow reserve parameters could provide a more consolidated indication when one parameter shows a borderline result.

4.5.4. Limitations and Further Work

The work presented in this chapter was conducted with a small sample size ($n=4$), as a pilot study, including mild to severe range of coronary artery disease. The inflow waveform was taken from a series of chest 4D CTs across the cardiac cycle divided into 10 equal intervals. A more in-depth examination of the pulsatile effects especially around the systolic peak will require waveforms with more sampling points over the cycle, which may be acquired with 4D CT of a much higher temporal resolution, time-resolved MRI or invasive flow measurements. However, as FFR and iFR tend to be measured during diastole in the wave-free region, an increased complexity in simulating the systolic region may not add a significant benefit.

CT-based calculation of FFR is focused on this thesis but other approaches exist. For example, an FFR-equivalent parameter called quantitative flow ratio (QFR) has been proposed, which is calculated based on the 3D model reconstructed from 2 projections of X-ray angiograms [127]. Such approaches have their own advantages and disadvantages, but the discussion of that is out of the scope of our work.

Although the trend of flow reserve parameters we observed in this study—not strongly sensitive to the inflow boundary conditions in most cases—appears consistent, this research can be furthered in two major directions: (1) using a larger sample size comparing the various inflow boundary conditions, and (2) verifying the result with the gold standard, i.e., invasively measured FFR. There are other factors, such as outflow boundary conditions, that potentially affect FFR. Studies to examine those factors are also warranted, and the effect of outflow boundary condition is investigated in next chapter.

It should be noted that whilst Patient 4's stroke volume and heart rate are both very high, they are within 2 standard deviations of from the average person[128], however the likelihood of a person having both these traits is

highly unlikely, and the cardiac output (calculated from multiplying the stroke volume by heart rate) for patient 4 does seem to be unrealistically large. As the stroke volume is produced from segmentation compared to heart rate, which is directly measured, it is likely that the LV cavity was not segmented well. Not all CTCA imaging produces a full set of images that allows segmentation of the LV cavity at specifically at the systolic and diastolic peaks. This may suggest that methods for calculating cardiac output may need to be refined, a common patient metric readily available to use is Body Surface Area (BSA), calculated from height and weight of the patient[129].

4.5.5. Concluding Remarks

The results in this chapter presented/confirmed that steady inflow simulations are appropriate for the purpose calculating of FFRCT, as well as alternate measures such as iFR. For the simulations in subsequent chapters, the steady inflow condition will be used, which minimises computational time and reduces the need for datasets with full dynamic CT required for a pulsatile inflow. With regards to using patient specific or population average parameters, it is apparent that FFR in particular varies with the flow through the vessel, which is highly correlated with cardiac output. Therefore, it is best to utilise patient specific parameters where possible, but cautions are needed when patient-specific metrics are derived from imaging which may introduce additional errors.

Chapter 5. The variability of FFRCT due to outflow boundary conditions and assumptions

5.1. Aim

The aim in this chapter is to examine the sensitivity of FFR to the various types of outflow boundary conditions (perfusion based and conventional morphological based) and evaluate the significance of patient-specific outflow boundary conditions. Additionally, a method to evaluate a potential range of FFR for individual patient is proposed and tested as an alternative method when perfusion is not known from PET or other type of imaging.

5.2. Introduction

In the previous chapter the variability of FFR was examined based on the inflow parameters such as pulsatile flow vs steady flow, patient specific flow rate and blood pressure. In this chapter, the impact of outflow boundary conditions, especially with regards to vasodilatory response to stress or hyperaemia, is investigated. As introduced earlier, vasodilation using adenosine is induced clinically in invasive measurement of FFR, which has been incorporated in conventional simulation based FFR assessment by a reduction of the outlet resistance.

Adenosine activates the A_{2A} receptor causing coronary artery vasodilation, leading to 3.5 to 4-fold increase in myocardial flow in healthy humans.[130] The increase in flow under hyperaemia is known as coronary flow reserve (CFR), a functional measurement of coronary health similar to but distinct from FFR. It reflects the health of an entire coronary tree including but not exclusively the microvasculature whereas FFR only assesses the possibility of epicardial disease. In microvascular ischaemic disease, the vasodilatory response is reduced (a CFR of <2 is common in diseased patients and is often used as a diagnostic threshold for general CAD) and in

some extreme cases, adenosine causes no change from the resting state ($CFR \leq 1$).[130]

In simulation-based measurements, these microvessels are part of the downstream boundary conditions for the outflowing coronary branches, which are typically defined by the resistance of the microvessels. The microvascular dilatory response can thus have a significant influence on the flow rate through each coronary branch. As CT cannot resolve microvascular anatomy and vasodilatory behaviour, many simulations resort to using this 3-4-fold increase of the flow as an assumption, which is used to adjust the downstream microvascular resistances for hyperaemic conditions down to 25-30% of its rest resistance.[131] This particular assumption was noted as a limitation of the conventional FFRCT methodology by Heartflow researchers [108], and suggested that in patients that suffer from microvascular dysfunction as well as epicardial disease, it would likely overestimate the severity of a stenosis.

To test the variability of the response to patient-specific hyperaemia and its effect on FFR, CTCA and Positron Emission Tomography (PET) perfusion imaging were integrated into CT-based FFR measurements, aiming to realise simulations with outflow boundary conditions that are more patient-specific and representative of diseased coronary arteries. PET perfusion is currently the gold standard for assessing myocardial perfusion among available imaging modalities: SPECT, CT perfusion and MR perfusion.[132] Because standard clinical PET myocardial perfusion imaging protocol includes both rest and stressed states (i.e. normal and hyperaemia, respectively), it allows to incorporate a clear picture of how the microvasculature dilates in CT-based FFR simulation as outflow boundary conditions.

5.3. Methods

5.3.1. Patients

The work in this chapter included 10 patients (6 male, 4 female, age: 61.7 ± 12.2 years) of various levels of epicardial stenosis (6 mild, 2 intermediate and 3 severe case) determined based on CTCA. The patients presented chest pain and other symptoms that indicated an intermediate risk of coronary artery disease. All patients underwent 4D CTCA for anatomical assessment and ^{82}Rb PET perfusion imaging to identify ischaemic regions in the myocardium. Demographic details of the patients are summarised in **Table 5-1**. The study was carried out in accordance with the recommendations of the South East Research Ethics Research Committee (Aylesford, Kent, UK) with written informed consent from all subjects, in accordance with the Declaration of Helsinki.

Table 5-1 Patient data table.

Patient	Sex	Age	Stenosed branch	Stenosis severity	
				Clinical classification	Diameter reduction on CT
1	M	79	RCA	intermediate	45%
2	M	59	LAD	mild	31%
3	F	64	LAD	severe	76%
4	F	75	LAD	mild	19%
5	F	80	RCA	severe	73%
6	M	51	LAD	trivial to mild	11%
7	F	64	LAD	trivial to mild	9%
8	M	50	RCA	mild	14%
9	M	50	RCA	trivial to mild	4%
10	M	45	LAD LCx	severe intermediate	55% 37%

RCA: right coronary artery, LAD: left anterior descending (artery), LCx: left circumflex.

5.3.2. ^{82}Rb PET Perfusion and flow reserve

The new model being investigated is a PET perfusion based FFRCT model, serving as a comparison to the morphological lumped parameter models, see section 3.3. The main drawback of CT-only FFRCT systems is

that hyperaemia (stress) is usually simulated by adjusting resistance uniformly across all branches and constant for all patients.

However, there are several reasons why that might not be a valid assumption: diseased vessels do not respond to the vasodilating drugs – typically adenosine – in the same way as healthy vessels, and not all patients respond to it to the same proportions, which can be measured as CFR. PET perfusion data is taken once at rest, and once stressed (using adenosine), producing realistic and patient-specific data. To use PET perfusion data to inform our boundary conditions, the co-registered CT and PET images are used to find the terminal position of coronary artery branches, which the regions of interest for assessing myocardial perfusion. A PET sampling sphere script is written in MATLAB to find the mean average PET Standard uptake value (SUV) at the regions of interest.

To make sure the PET sampling sphere is not adding up voxels that carry no perfusion as it is outside the myocardium, the PET sphere will perform a check and not add up perfusion values in regions where the corresponding voxel in the CT image displays a HU that is not representative of the myocardium. Essentially only when the CT image confirms a certain voxel is part of the myocardium will the PET value of that voxel be considered.

The patient data is taken using 82-Rb PET perfusion imaging (GE Healthcare PET/CT Discovery STE) as part of a PET/CT combined investigation. 82-Rb is a popular tracer choice used almost exclusively in PET/CT imaging modalities and has the advantage of not requiring an on-site cyclotron and its short half-life also reduces radiation dose to the patient.

However, 82-Rb uptake values do not correlate proportionately to flow/perfusion in comparison to 15-O (Water) and 13-N (Ammonia) perfusion imaging and therefore requires additional processing to produce perfusion values.

The perfusion values in this study are obtained via the Siemens Syngo software shown in Figure 5-1. It uses a single compartment model

based on the tracer kinetic models of Lortie et al[132] for Rb-82 tracer.

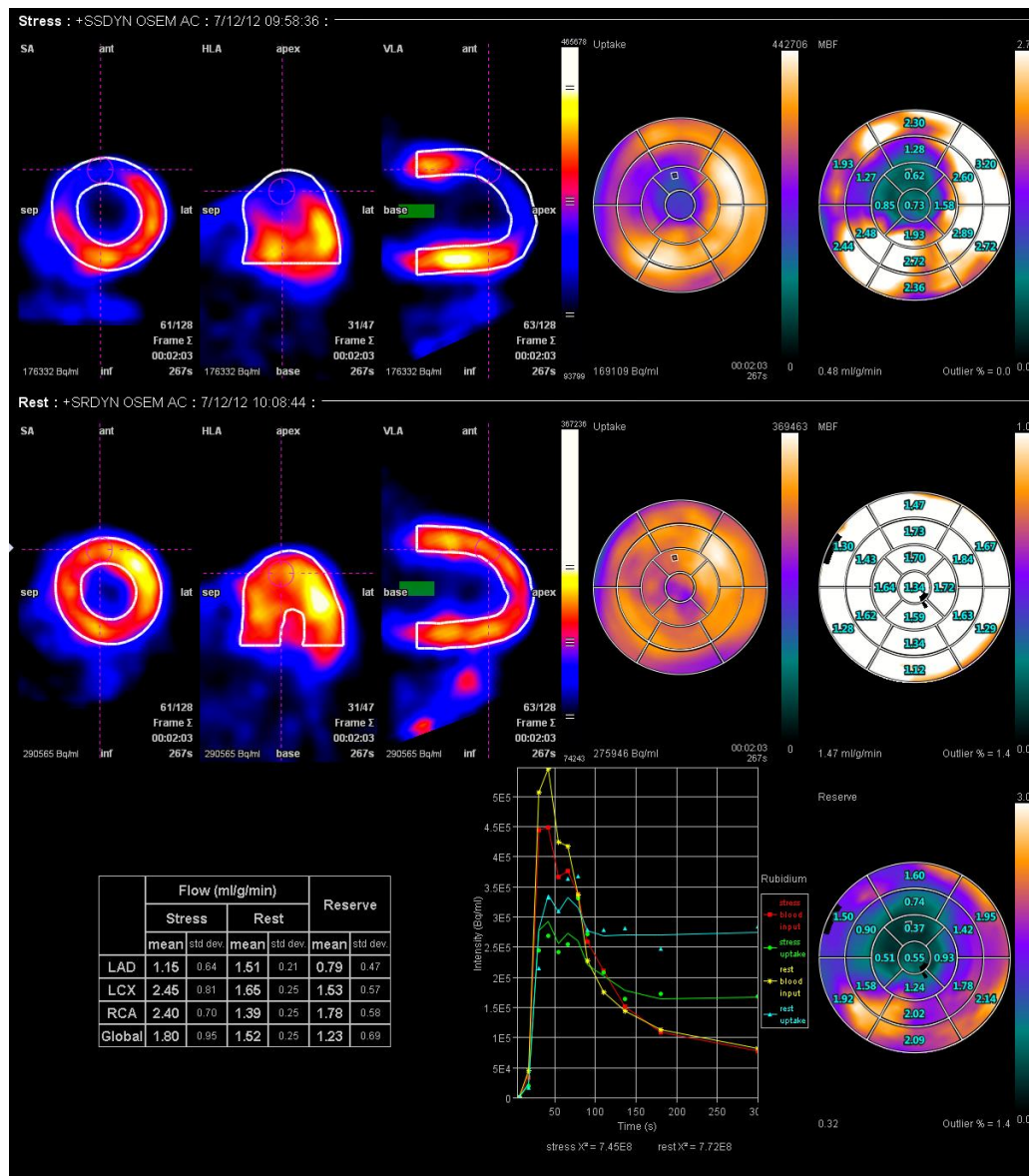


Figure 5-1 Example of Siemens Syngo software outputs that accompanies Siemens PET/CT scanners (image courtesy of UCLH). The bullseye plots show the estimated blood flow based on tracer uptake of each myocardial region. The program requires minimal manual segmentation by the operator to identify the approximate shape of the myocardium. The table on the bottom left shows the stress and rest flow (though perfusion and flow here are used interchangeably, as the value is divided per unit tissue mass), and the ratio, the flow reserve for each macro-region supplied by each major coronary artery: LAD, LCX, RCA.

Table 5-2 Perfusion and coronary flow reserve obtained from PET imaging. *Vessel specific flow reserve and absolute perfusion (during stress) was obtained by sampling the region supplied by the stenosed vessel. **LAD, LCX, RCA regional flow reserves and absolute perfusion are obtained by Siemens Syngo software package. Yellow shaded cells indicate the vessel that has the suspected stenosis.

Patient (affected vessel)	Vessel-specific flow reserve (absolute perfusion [ml/g/min])*	LAD regional flow reserve (absolute perfusion [ml/g/min])**	LCX regional flow reserve (absolute perfusion [ml/g/min])**	RCA regional flow reserve (absolute perfusion [ml/g/min])**
1 (RCA)	1.72(1.45)	2.05(2.12)	2.44(2.00)	1.43(1.16)
2 (LAD)	4.45(4.11)	4.09(3.80)	4.60(2.99)	5.13(3.99)
3 (LAD)	0.80(1.03)	0.79(1.15)	1.53(2.45)	1.78(2.40)
4 (LAD)	2.21(3.42)	2.05(3.28)	1.16(2.16)	1.84(3.22)
5 (RCA)	1.21(1.13)	1.73(1.68)	1.56(1.64)	1.15(1.09)
6 (LAD)	3.44(3.27)	3.19(3.13)	3.17(3.03)	3.65(3.17)
7 (LAD)	1.89(2.65)	1.58(2.14)	2.04(3.35)	2.01(2.99)
8 (RCA)	3.59(4.50)	3.46(4.30)	3.71(4.04)	3.54(4.74)
9 (RCA)	3.32(2.18)	3.53(2.62)	4.01(2.47)	3.15(1.90)
10 (LAD)	0.81(1.11)	0.65(0.92)	1.07(1.27)	1.40(1.50)
10 (LCX)	1.19(1.41)	0.65(0.92)	1.07(1.27)	1.40(1.50)

5.3.3. PET/CT registration

As PET/CT scans were performed sequentially not simultaneously, subsequent co-registration of the PET and CT images are required to align the PET perfusion information with the correct myocardial region in the CT image. PET data of patients in a stressed and rest states, time averaged were used for the purposes of this study.

A MATLAB script was developed to co-register the PET and CT images; the process is shown in Figure 5-2 to Figure 5-6 . The script scales the PET image, which has the lower resolution of the two (typically 2.5mm for ^{82}Rb PET vs 0.35mm for CTCA), to the same pixel dimensions as the CT.

The user manually selects 5 correspondent points on the two images, using landmarks such as the ventricles, apex, ribs, aorta etc. The script uses a 5 point iterative closest point (ICP) algorithm that rotates and translates within a plane. This is repeated in the sagittal plane.

As PET images have far too low resolution to observe flow information within the coronary arteries, registration error smaller than the vessel diameter $\sim 2\text{-}5\text{mm}$ is unnecessarily accurate. Using a 1-2 cm radius spherical sampling volume surrounding the terminal ends, the averaged PET intensity of each region can be used to determine relative flow between each coronary artery. The flow distribution will then serve as the outlet boundary conditions, in contrast to the morphology based outlet condition outlined by Olufsen et al and ZKM etc [93,133].

This contrasting outlet condition is to challenge the common assumption made in FFRCT protocols that use morphology based outlet conditions: that hyperaemia reduces the flow resistance in each branch by a universal value (approximately 25-30% of the resistance in the rest state in the conventional approach [44]). However, this is often criticised as individual arteries may have varying responses to hyperaemia, especially in patients suffering from microvascular disease. As CTCA imaging is generally performed only in the rest state, the PET flow information, which is obtained in both rest and stressed states, will serve as a useful point of comparison to CT-only FFRCT protocols that simulate stress by adjusting resistance artificially.

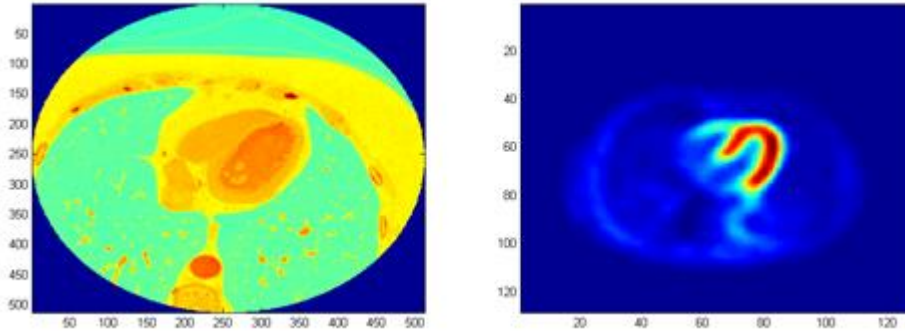


Figure 5-2 A pair of CT (left) and PET (right) images of the patient's chest. The coordinates shown indicate the pixels of the images

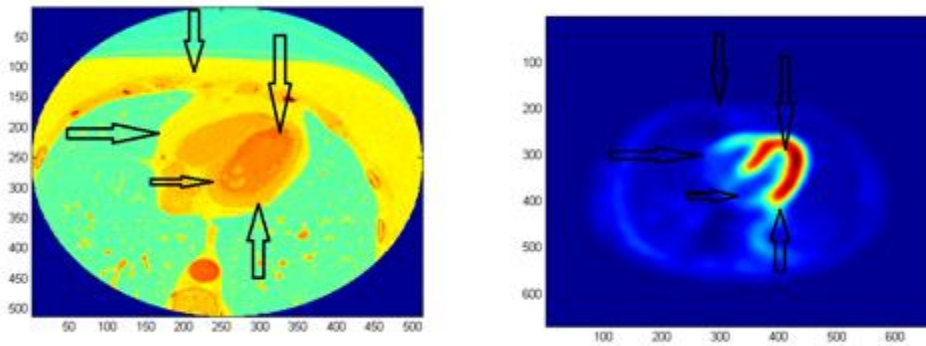


Figure 5-3 PET image is resized, and five corresponding points on each image are identified by the user. An ICP algorithm manipulates the images through translation and rotation so that they are fully aligned. The example is a transversal image across the chest cavity, and the same process is followed for the sagittal plane to get the co-registration done in 3D

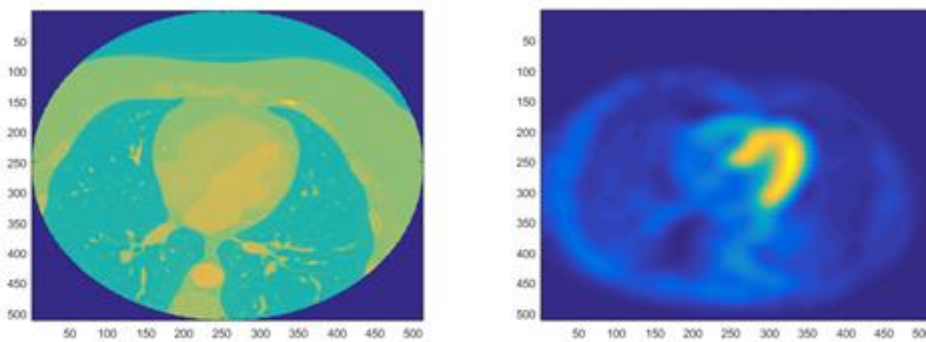


Figure 5-4 An example of a co-registered transverse slice of CT (left) and PET (right)

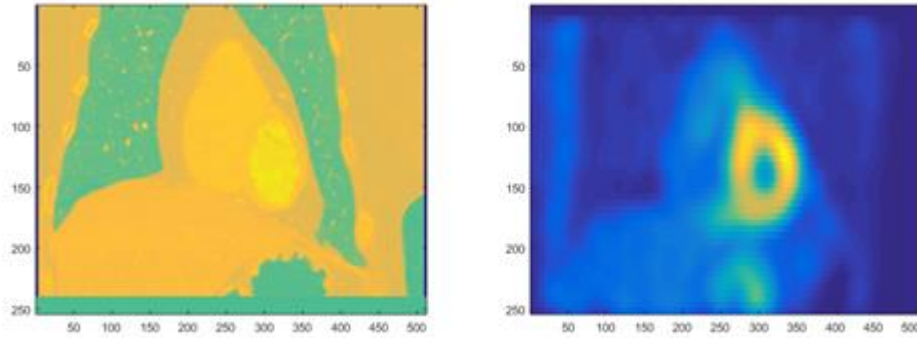


Figure 5-5 An example of a co-registered sagittal slice of CT (left) and PET (right)

Each patient has two sets of PET perfusion images, taken during the rest state (baseline) and during the hyperaemic state. The patient-specific and spatially local hyperaemic response can be calculated and implemented in the model. As the result, the total hyperaemic coronary outflow as a proportion of cardiac output is not fixed and reflect the varied hyperaemic response between patients.

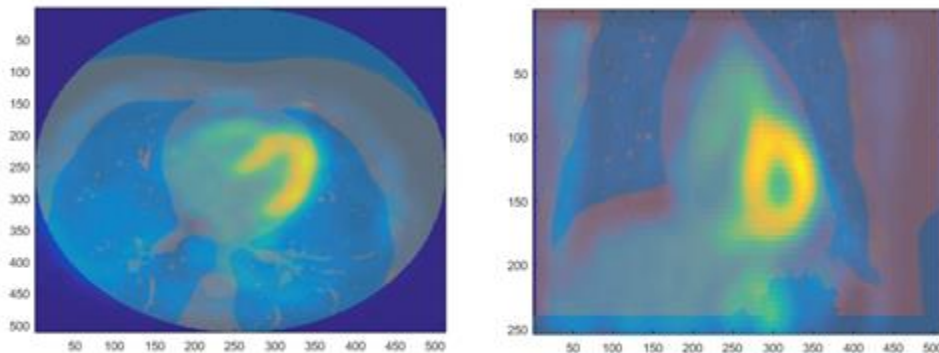


Figure 5-6 Example of a composite PET/CT image of Subject 3. Transverse slice of the heart (left). Sagittal slice of the heart (right)

5.3.4. Variability quantification of PET-CT registration

To consider the intra-operator variability in registration, the manual landmark selection was performed twice on two separate occasions and the variability in X, Y, Z coordinates between the two attempts at registration was counted for each subject. Here, X, Y, Z coordinates correspond to left-

right, anterior-posterior and head-foot directions, respectively, i.e., XY plane is the transversal plane.

Table 5-3 Pixel deviation (variability) between two attempts of co-registration. Note that the value is absolute, i.e., strictly positive. Error is the result of manual selection of corresponding landmarks

	x-error in pixels	y error in pixels	z error in pixels
Subject 1	5	4	2
Subject 2	5	5	1
Subject 3	6	3	2
Subject 4	4	6	0
Subject 5	3	8	1
Subject 6	6	5	0
Subject 7	7	4	2
Subject 8	3	8	1
Mean Variability	4.875	5.375	1.125
Mean Variability in mm	2.93	3.36	3.67

The Z dimension experiences the smallest pixel error in registration but highest spatial error primarily because its pixel size represents a far larger space. The Z dimension pixel is the slice thickness of the image which is 3.27 mm per slice. While the X and Y dimensions are 0.625 mm per pixel. This is an acceptable error as it is lower than the spatial resolution of the PET image which is ~5mm.

5.3.5. PET-based perfusion sampling for PET model implementation

A PET-perfusion-based boundary condition was developed to contrast the structured tree method in Chapter 3 which prescribes downstream resistances only based on the size of the of the branch

terminus in the 3D model. The perfusion-based boundary condition (PBC) refers to the local perfusion quantitatively, based on the PET image intensity (representing perfusion in ml/g/min [130]), in the region supplied by each branch. Local perfusion was quantified by placing a sampling sphere (20 mm diameter) at the end of each branch in 3D model, and the spatial average of perfusion was calculated, excluding image pixels with its value lower than 10 ml/100ml/min (this was determined by looking at the noise of empty space and 10ml/100ml/min is low enough to discount any myocardial tissue whilst not including noise), in order to eliminate the space outside the myocardium in the sphere. Rather than averaging out all the pixels of the sample region, Figure 5-7 to Figure 5-9 show why the low intensity regions (area outside the myocardium) needs to be excluded. The peripheral resistances downstream to each of the branches are then determined such that the flow split through each branch corresponds to the split in the PET-based measurement. Thus, in this approach, the resistance does not depend on the terminal branch size. Here, as in the MBC, the coronary outflow is assumed to be 5% of the total aortic output.

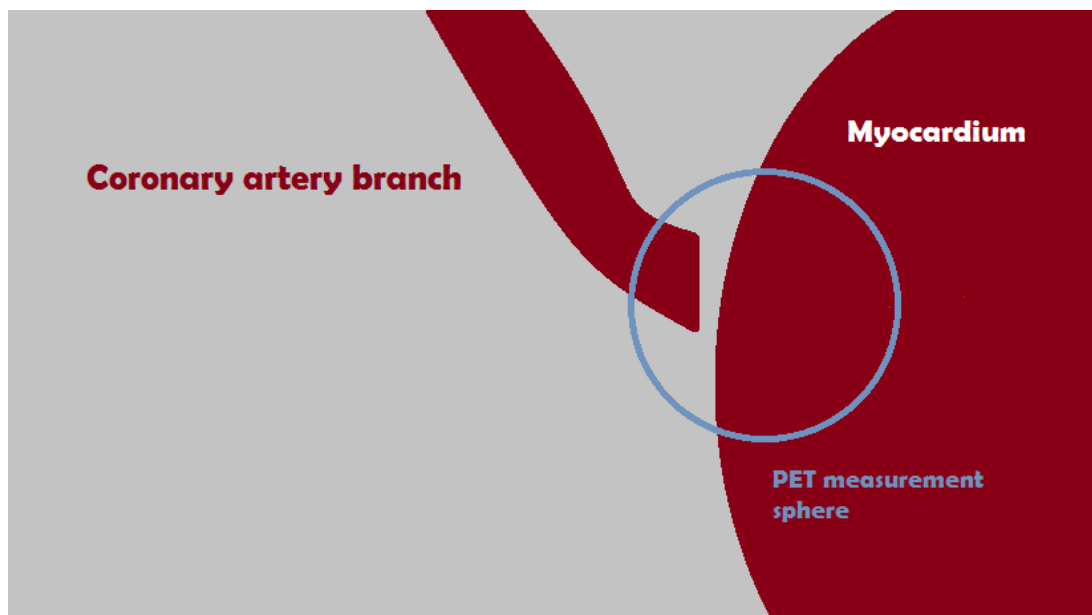


Figure 5-7 Diagram showing a good placement of the PET perfusion measurement sphere. The coronary artery mesh is terminated right next to its contact point with the myocardium. By projecting the sphere forwards, it can easily quantify the perfusion supplied by this branch

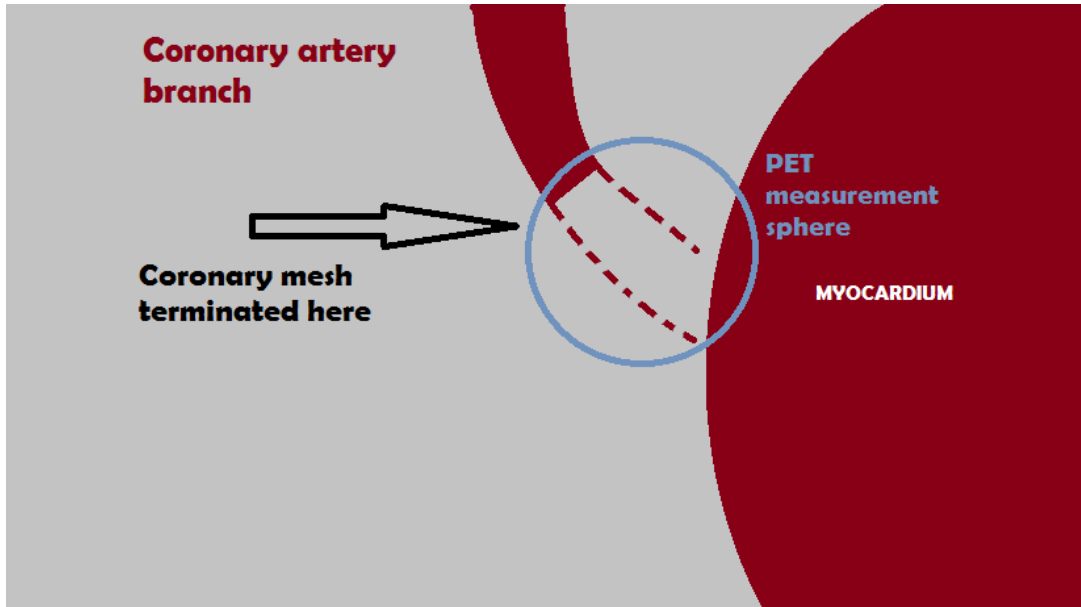


Figure 5-8 Diagram showing the problem with an early terminated mesh, where the coronary artery branch ends far away from the myocardium. The PET measurement sphere will just average the portion of that sphere that is within the myocardium ignoring the space outside the myocardium. While that will work, it is still recommend placing the sampling sphere closer to the myocardium as it is more representative of the coronary flow.

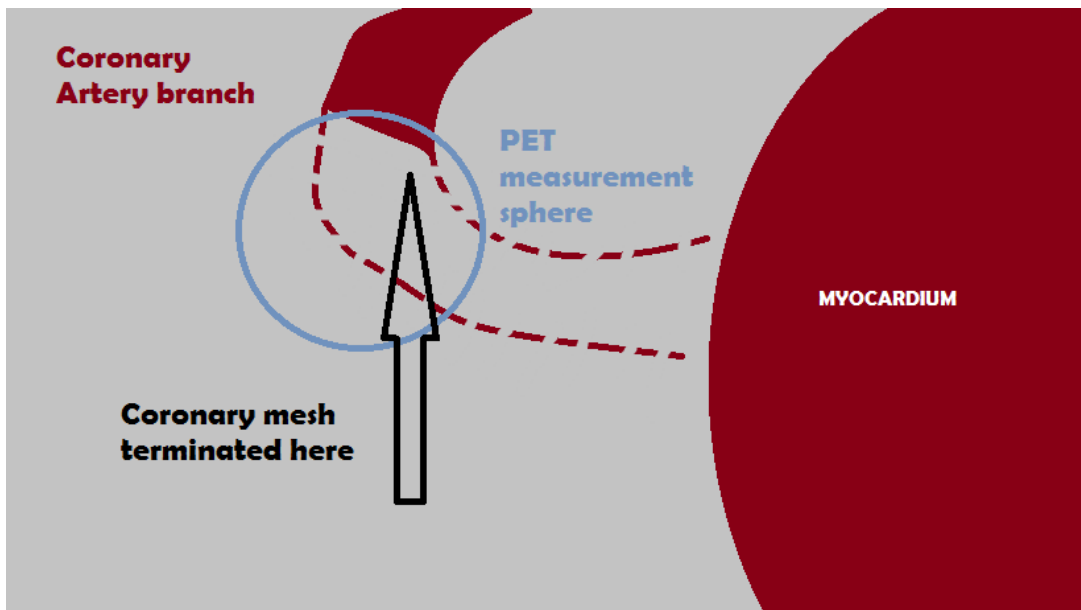


Figure 5-9 Diagram showing an obviously early terminated mesh. Because the coronary artery points away from the myocardium, it is easily identifiable by eye, when looking at the mesh, that the PET values measured within the sphere is meaningless. The PET sampling will know through the CT image that it is outside the myocardium and therefore return a 0 value. This happens because of poor registration, but also because CT and PET scans are taken at different times, different orientations and different stages of the cardiac cycle. When a large misalignment occurs, it is easier to just manually input the perfusion sphere coordinates based on inspection of the mesh geometry, rather than re-registering the two images.

Two different size spheres were used to capture perfusion. Occasionally, the small sphere size may not be representative of the perfusion of the region, especially if it is mis-aligned. Conversely, a large sphere may observe perfusion from multiple sources and not the coronary artery being assessed. A large sphere also helps to minimise the effect of any errors in CT-PET registration. 10mm (Figure 5-10) and 20mm (Figure 5-11) sampling spheres were chosen as they represented a good compromise between overcoming CT-PET co-registration errors (in the order of 2-5mm), and incorrectly attributing perfusion from other branches (some branches terminate as close as 20mm from each other). Ultimately the 20mm sampling sphere option was chosen.

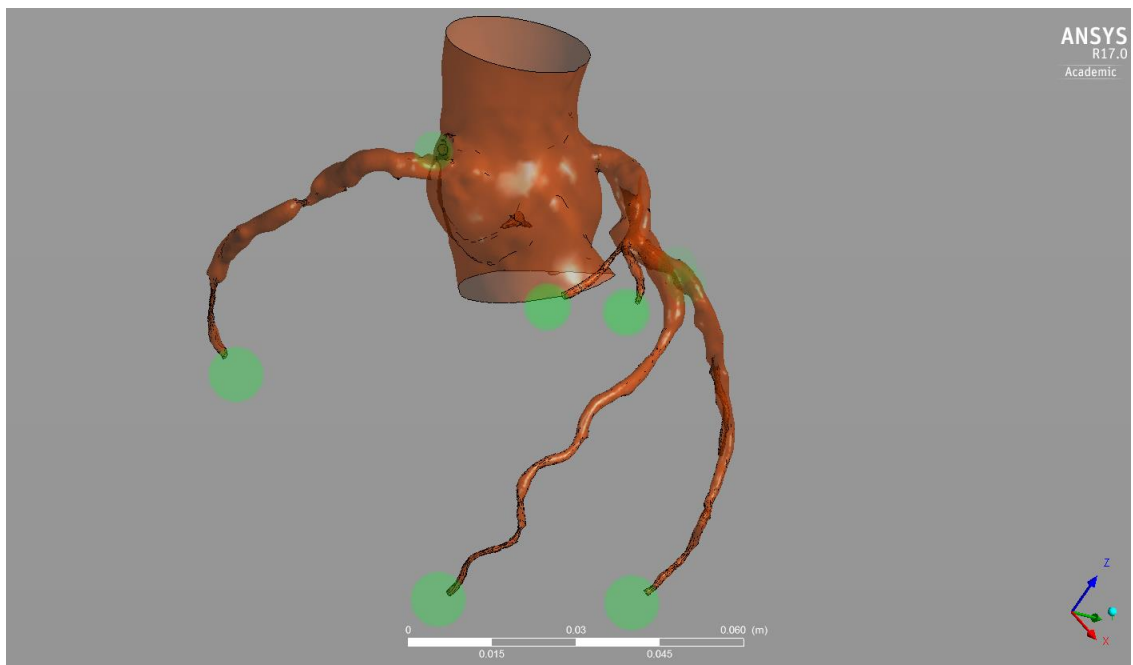


Figure 5-10 Depiction of the placement of PET perfusion measurement spheres (green circles). Note that they are projected forward from the terminal end of the artery, to approximate the myocardial region that is being supplied. The example here is the 10mm diameter measurement sphere.

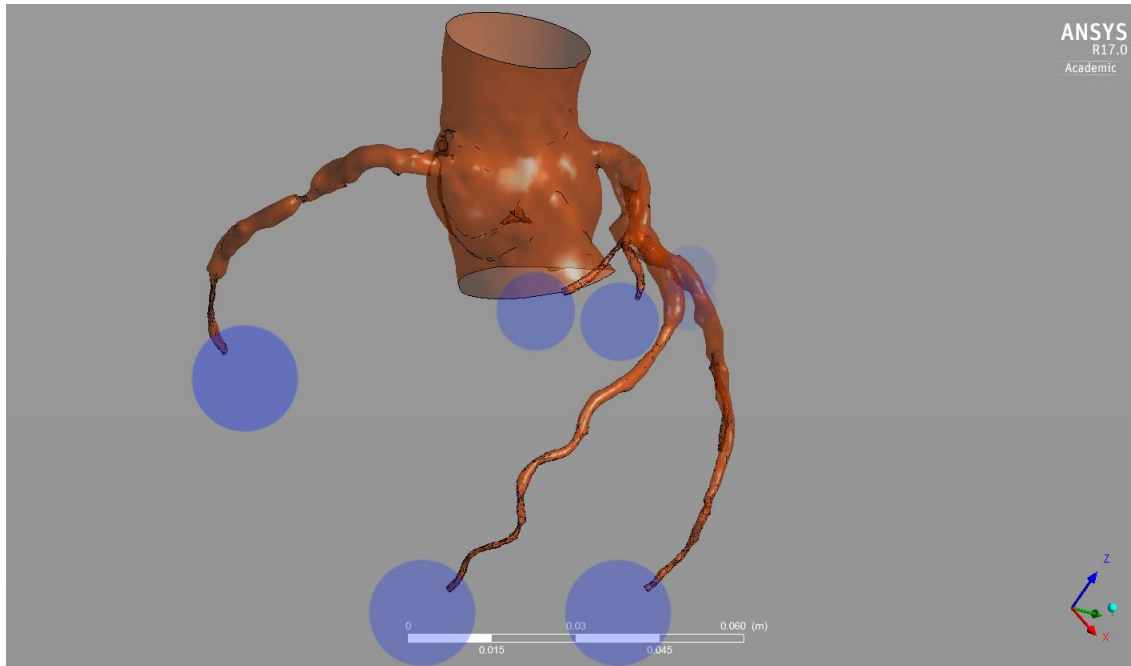


Figure 5-11 Depiction of the placement of PET perfusion measurement spheres (blue circles). Note that they are projected forward from the terminal end of the artery, to approximate the myocardial region that is being supplied. The example here is the 20mm diameter measurement sphere.

The final PET perfusion sampling works as follows:

1. Generate a sphere of 20 mm diameter around the terminal end of a coronary branch (this must be located using the CT image during segmentation) in the 3D model. The sphere in general overlaps significantly with the myocardial region supplied by the chosen coronary branch.
2. Sample the sphere for perfusion values above 0.1 ml/g/min (a normal value of perfusion is between 0.5 – 3 ml/g/min[130]), effectively ruling out the spaces captured in the sphere where it is outside the myocardium.
3. Calculate the spatial mean perfusion of the myocardial region within the sphere, this value is used to represent the flow capacity of a coronary branch.
4. In the baseline (resting state) simulation, the 5% of aortic output that is allocated to the coronaries is divided by the various branches via

their flow capacities, that are implemented in the form of downstream microvascular resistance.

5. In the hyperaemic (stressed state) simulation, the magnitude decrease in resistance of each branch is derived from the change in perfusion that is observed between the rest and stressed states.

5.3.6. Inflow boundary conditions

Based on the previous chapter, it was decided for efficiency that the inflow into the aorta was set as a steady flow. While this is not representative of ordinary cardiac function that is pulsatile, the detailed comparison between steady and pulsatile flow conditions has shown that steady flow condition is sufficient in CT-based FFR calculations.[71] Inflows were set patient specific, calculated based on the difference between ventricular cavity volume, segmented from 4D CT images, at maximum contraction in systole and maximum dilatation in diastole, multiplied by the patient's heart rate.

5.3.7. Implementation of outflow boundary conditions

In the baseline state, a reasonable assumption is to assign 5% of the total aortic output to the coronary arteries.[107] To accomplish this, the resistance at the aortic outlet was tuned, also in reference to the total coronary resistance, such that the systemic outflow through the aorta corresponds to 95% of the stroke volume. In the hyperaemic state, however, the proportion of coronary flow to aortic output varies from 5% and also patient to patient, and especially so in patients who suffer from some form of coronary artery disease.

This was accounted for by adjusting peripheral resistance downstream to each branch, without control of the flow split between systemic and coronary circulations at hyperaemia. This was achieved using the relationship below:

$$R_{aorta} = 0.05 \frac{1}{\sum_{i=1}^n (1/R_i)} \quad (17)$$

R_{aorta} is the resistance of the aorta outlet, and this relationship is essentially tuning this resistance to 5% of the total resistance of the microvessels, each microvessel outlet resistance expressed as R_i . As these outlets are in parallel, the inverse of the sum of their inverse is the total resistance of the microvasculature. It should be noted that all the resistances are also scaled to produce the known patient blood pressure and cardiac output. This approach is used in conventional FFRCT methods [44].

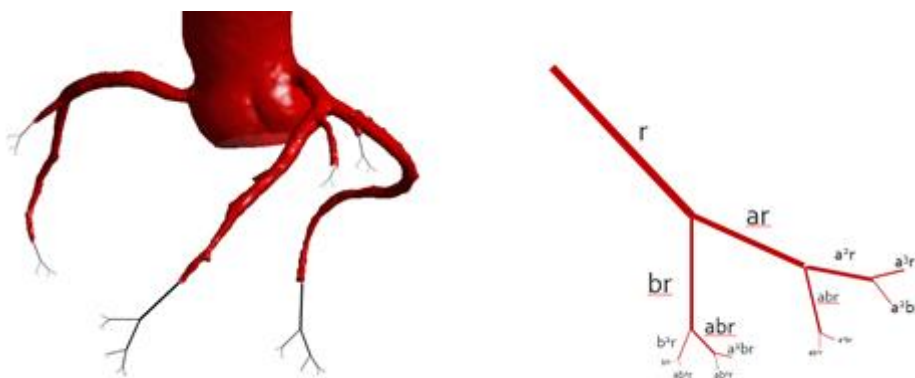


Figure 5-12 (Left) Illustration of downstream microvascular trees. (Right) Diagram of structured tree downstream microvascular structure. r represents the radius of the terminal vessel, and the daughter branches split asymmetrically in a repeated way, with fractions a and b , with values of 0.9 and 0.6 respectively.[93] This branching occurs indefinitely until it reaches the minimum radius.

5.3.8. Vasodilatory response model with structured tree

To test whether it is appropriate to set hyperaemic resistance to be 30% of baseline resistance and how sensitive FFR is to this, we performed simulations in which the downstream resistance of the diseased branch is adjusted to various reduced level (30%, 50%; 70%, 90%) of its baseline value calculated from the structural tree model. The range reflects the vast majority of patient disease cases, where microvascular vasodilatory response varies

from healthy and ideal ($CFR > 3.0$) to ineffectual ($CFR \sim 1.0$, virtually no vasodilation). These conditions are referred as Morphological based Boundary Conditions (MBC) with their reduced resistance level, e.g., MBC 30%, MBC 50%, etc., later in this chapter.

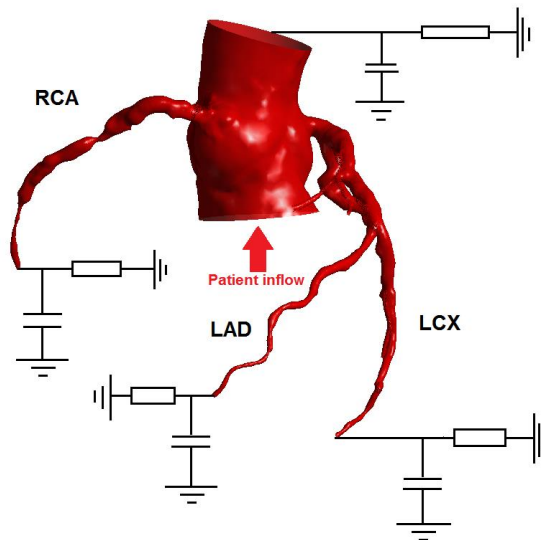


Figure 5-13 Schematic showing the outflow boundary conditions. All the boundary conditions are two-element Windkessel models represented in the circuit diagram.

5.3.9. Computational methods

The computations in this chapter were conducted in the same way as in Chapter 4. However, in this chapter it will strictly be in steady state flow simulation rather than attempting pulsatile flow.

5.3.10. Examination of results to investigate the effect of outflow BC

CFD analyses on 3D patient-specific anatomical models were conducted using various outflow boundary conditions introduced above, namely

- (1) structured tree boundary conditions with typical hyperaemic response (reduction of resistance to 30% of baseline)
- (2) structured tree boundary conditions with hyperaemic response that is varied across the possible disease spectrum and
- (3) perfusion (PET) based boundary conditions.

The results were evaluated in terms of FFR values. Monitor points were placed at the coronary ostium and in the coronary artery at a point approximately 4 cm distal to the stenosis. FFR standards in invasive measurements specify at least 2-3 cm distally, 4 cm was chosen to be consistent and to ensure the minimum possible FFR (i.e. largest pressure drop in the vessel) is captured, following the finding of a computational sensitivity study by Solecki et al.[119] In the simulated results, the pressure distal to the stenosis divided by the pressure at the coronary ostium was used as the final CT-based FFR value.

5.4. Results

5.4.1. Perfusion based boundary conditions versus conventional boundary conditions

Typical examples of the computational results, in terms of pressure distributions along the coronary vessel tree, are shown in Figure 5-14. Wide spectrum of anatomical variations (tortuous/straight vessels, high/low number of side branches etc) and some different levels of pressure drop across the tree can be observed. The pressure drop from the aorta to the end of branches is in general larger for the models with PBC.

A quantitative comparison of FFR values across the stenosis is presented in Table 4 including those with all the peripheral resistance variations of MBC. FFR range is from 0.64 (Patient 5 with MBC 30%) to 0.99 (Patients 6 and 7 with PBC). In reference to the cut-off value of CT-based FFR (0.80 [134]), the range of FFR in this study reflects the wide range of disease state included in the study.

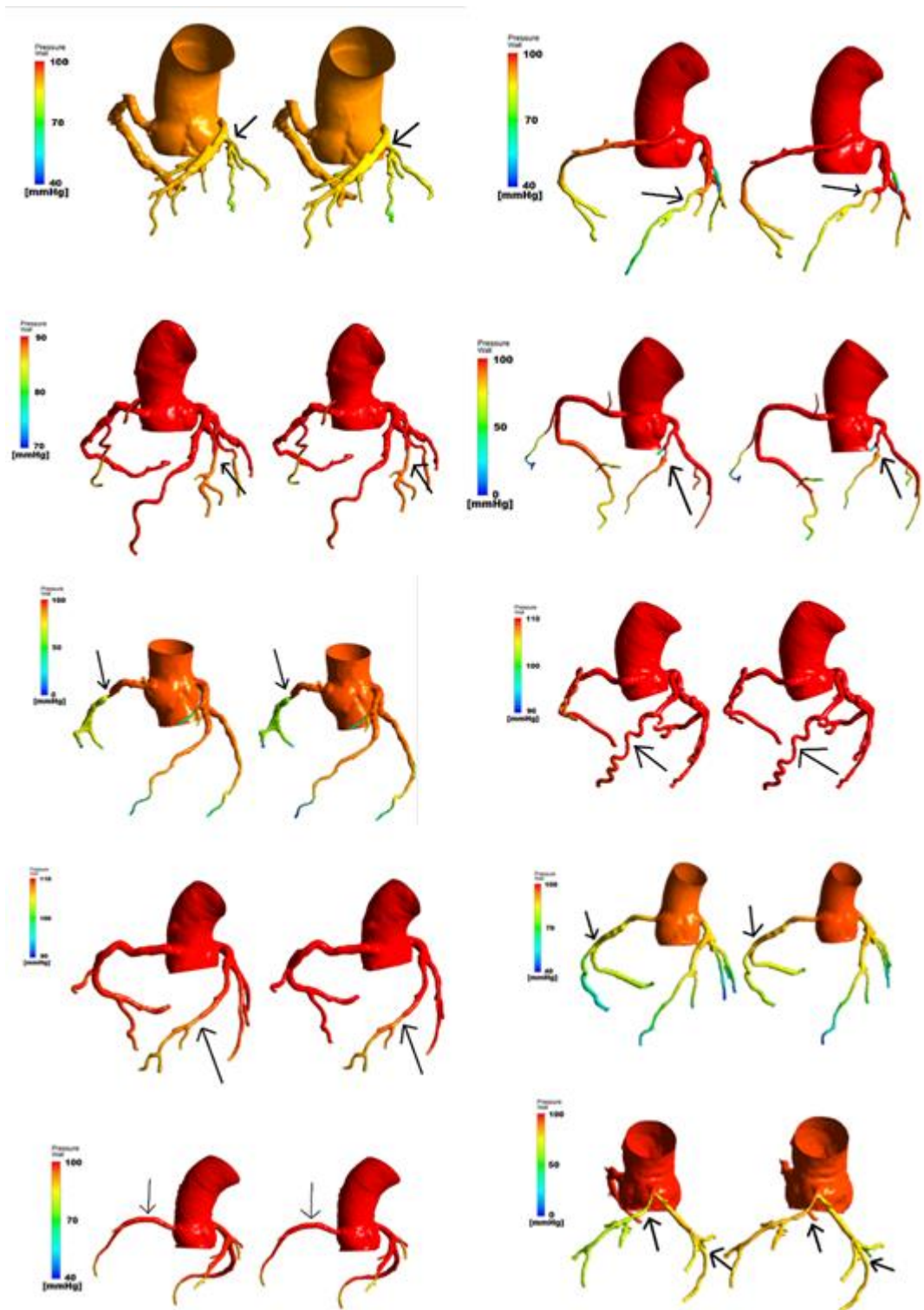


Figure 5-14 Comparison of pressure profiles obtained from PET-based boundary conditions (left of pairs) versus conventional morphology-based boundary conditions (right of pairs). Patient 1-10 from top left to the bottom right. Arrows indicate focal stenosis

The FFR with PBC and ‘the standard (i.e., 30%)’ MBC are in general correlated well ($r = 0.68$). The correlation is higher for the patients with high FFR values ($FFR \gg 0.80$), i.e., patients with relatively minor or insignificant stenosis. The PBC tends to result in FFRs that are higher than the ones with the conventional boundary condition (MBC 30%). However, this is not true for Patients 3, 9 and 10. Patient 3 is the most extreme case where the FFR with PBC (0.76) indicates a different diagnostic result than the conventional MBC 30% ($FFR=0.81$), straddling across the standard cut-off value of 0.80.[134]

The FFR values obtained with the variable peripheral resistances in MBC show a clear trend of high FFR for high resistance (i.e., smaller degree of resistance reduction – close to the baseline) consistently across the patients. This was expected, based on a principle of fluid mechanics; low peripheral resistance invites higher flow to the branch which results in a larger pressure drop thus smaller FFR.

The flow rates through different branches are summarised in Table 5, both in absolute value and proportion to the total coronary flow. A comparison between Tables 4 and 5 indicates that the flow rate is a strong determinant of FFR, with higher flow rates corresponding to lower FFR (more severe stenosis). Considering Poiseuille’s law, the flow rate increase should linearly be related to the pressure drop and define FFR in these vessels as in the following equations.

$$1 - FFR = 1 - \frac{P_d}{P_a} = \frac{P_a - P_d}{P_a} = \frac{\Delta P}{P_a} \quad (18)$$

$$\Rightarrow FFR = 1 - \frac{\Delta P}{P_a} = 1 - \frac{8\mu L}{\pi P_a r^4} Q \quad (19).$$

Additionally, the MBCs with various level of peripheral resistance demonstrate a strong association between the flow rate and the percentage of coronary flow that is distributed to the stenotic branch. In general, the flow through the stenosed branch is lower with PBC than with MBC but for Patients 3, 9 and 10 (LCx), where the PBC-based FFR was lower than that of MBC 30%, the flow with PBC is higher.

Figure 5-15 is a graphical representation of Table 4, showing FFRs obtained with PBC and MBC with the range of reduced peripheral resistance.

Here, the range of FFR with the variable MBC is examined in a different way to illustrate more fundamental principle underpinning their relationship. The patients are reordered in reference to FFR with MBC 30% so that the trend is clearly visible. For patients with an FFR close to or below the cutoff of 0.8, the discrepancy in FFR values between PBC and MBC 30% is more significant. The range of FFR for the various peripheral resistance is also larger for the lower overall FFR. On the other hand, the range for patients having high overall FFR is small, only 0.01 for Patients 4, 7 and 9.

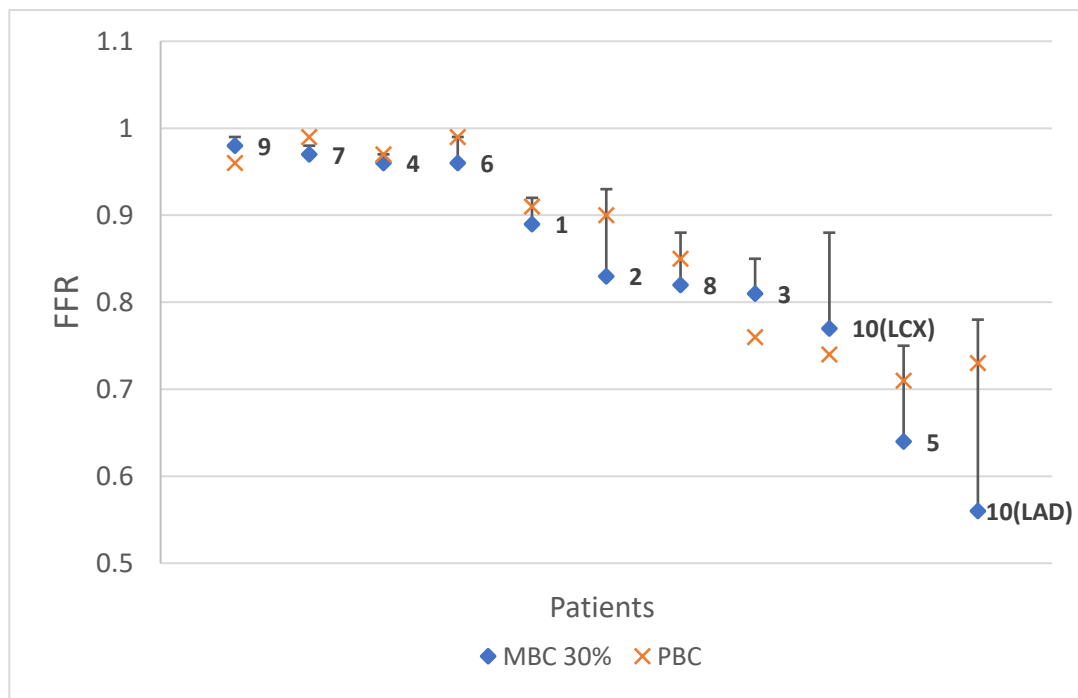


Figure 5-15 The FFRs of patients, reordered in reference to the value of FFR calculated with MBC 30%. The bars indicate the range of FFRs obtained using the various MBCs, with the conventional (MBC 30%) marked as a blue diamond, and the PBC marked as orange cross. Patient numbers are shown on the plot as reference.

Table 5-4 CT-based FFR values obtained using various outflow boundary conditions. PBC: PET-based boundary condition, MBC: morphology-based boundary condition. The percentage values indicate reduced resistance level to account for hyperaemic flow increase and reduction to 30% (MBC 30%) is the conventional assumption. *This is technically not FFR as it is in the rest state, but rather Pd/Pa.

Patient	PBC	MBC (30%) "Conventional"	MBC (50%)	MBC (70%)	MBC (90%)	MBC (100%) "Rest"*
1	0.91	0.89	0.91	0.92	0.92	0.92
2	0.90	0.83	0.88	0.92	0.93	0.93
3	0.76	0.81	0.83	0.84	0.85	0.85
4	0.97	0.96	0.96	0.97	0.97	0.97
5	0.71	0.64	0.74	0.75	0.75	0.75
6	0.99	0.96	0.96	0.98	0.99	0.99
7	0.99	0.97	0.98	0.98	0.98	0.98
8	0.85	0.82	0.85	0.86	0.88	0.90
9	0.96	0.98	0.98	0.98	0.99	0.99
10 (LAD)	0.73	0.56	0.68	0.74	0.78	0.80
10 (LCx)	0.74	0.77	0.85	0.88	0.88	0.88

Table 5-5 Flow rates through stenosed branch and proportion of that to the overall coronary flow (%), obtained using various outflow boundary conditions.

Patient	PBC, [ml/s]	MBC (30%), [ml/s]	MBC (50%), [ml/s]	MBC (70%), [ml/s]	MBC (90%), [ml/s]
1	3.98 (48%)	4.69 (56%)	3.78 (45%)	3.39 (41%)	3.26 (39%)
2	3.41 (40%)	5.54 (64%)	4.59 (53%)	2.72 (32%)	2.50 (29%)
3	2.78 (29%)	2.23 (28%)	2.07 (26%)	1.82 (23%)	1.74 (22%)
4	2.61 (32%)	3.45 (38%)	2.87 (32%)	2.57 (29%)	2.42 (27%)
5	1.39 (20%)	1.72 (22%)	1.28 (16%)	1.26 (16%)	1.20 (15%)
6	2.19 (33%)	5.18 (68%)	4.37 (57%)	2.79 (37%)	1.45 (19%)
7	1.34 (17%)	2.86 (22%)	2.35 (18%)	2.11 (16%)	1.98 (15%)
8	1.69 (16%)	2.14 (21%)	1.71 (17%)	1.52 (15%)	1.32 (13%)
9	5.01 (55%)	4.50 (53%)	4.12 (48%)	3.90 (46%)	2.56 (30%)
10 (LAD)	2.24 (21%)	3.83 (34%)	2.82 (25%)	2.17 (19%)	1.91 (17%)
10 (LCx)	1.22 (11%)	1.09 (9.5%)	0.71 (6.2%)	0.58 (5.1%)	0.56(4.9%)

5.4.2. Multi-vessel disease case

Patient 10 has two significant stenoses on two separate branches, see Figure 5-14, the LAD and LCx. In order to examine potential interaction of the flow in the two branches under the varied peripheral resistances. The hyperaemic condition was varied, using the concept of variable MBC, first in each of the LAD and LCx individually, and then both LAD/LCx simultaneously. The result is summarised in Table 6, it was observed that though the FFR values in one branch are affected by the varying outflow condition of the other branch, the effect is minor. Therefore, the effect of varying peripheral resistance in two stenosed branches can practically be seen as independent.

This is to be expected as the system of outlets can be treated as parallel circuits where the increased current/flow increases the pressure but maintains the same pressure/voltage ratio as suggested by the equation 7 in section 5.1.2.

Table 5-6 CT-based FFR values for Patient 10 when each diseased vessel's hyperaemic condition was varied individually and in combination.

Branch with varied BC	MBC 30%	MBC 50%	MBC 70%	MBC 90%
LAD	(LAD) 0.56 (LCx) 0.77	(LAD) 0.68 (LCx) 0.77	(LAD) 0.74 (LCx) 0.76	(LAD) 0.78 (LCx) 0.76
LCx	(LAD) 0.56 (LCx) 0.77	(LAD) 0.56 (LCx) 0.85	(LAD) 0.56 (LCx) 0.88	(LAD) 0.55 (LCx) 0.88
LAD+LCx	(LAD) 0.56 (LCx) 0.77	(LAD) 0.65 (LCx) 0.86	(LAD) 0.73 (LCx) 0.89	(LAD) 0.76 (LCx) 0.90

5.5. Discussion

5.5.1. FFR analysis

Although coronary artery flow computations have a relatively long history and boundary conditions have always been a point of discussion, to my knowledge, there was no study utilising measured myocardial perfusion to produce patient-specific outflow conditions. In addition there hasn't been much research using myocardial perfusion patient data to produce an estimate suitable for various patient demographics. The perfusion data was used to examine the impact of resistance reduction during hyperaemia, and an attempt was made to characterise an uncertainty range of FFR due to non-ideal response to vasodilator by the vasculature peripheral to the stenosis. Uncertainty of FFR-CT computation has been studied in terms of the sensitivity of FFR to imaging and segmentation uncertainty[135], but not the hyperaemic response to adenosine.

The results show a high correlation of FFR values computed using the two types of outflow boundary conditions, namely MBC and PBC. This is not surprising for the patients with relatively minor stenosis because there is no significant pressure drop across the stenosis anyways. Therefore, even with different flow distributions across the branches of the coronary arteries obtained via the varied outflow boundary conditions, the pressure drop across the stenosis for those patients was not significantly altered (e.g., Patient 9, FFR range: 0.98-0.99 for various MBCs).

On the other hand, the difference of hyperaemic condition model is shown to have a strong influence on the FFR calculations for more severe stenosis such as Patients 3, 5 and 10. The pressure drop ΔP across a pipe is related to the flow rate in the pipe Q and resistance R (in this case, the stenosis): $\Delta P \approx Q \times R$, using Poiseuille's law. An increase in flow rate for a given stenosis or a more severe stenosis (i.e., increased resistance) increases the pressure drop, therefore lowering FFR. This is a simple fluid mechanical principle behind the differences caused in FFR. The same principle therefore implies that a reduced flow rate in a stenosis would result

in a higher FFR, i.e., indicating a less functional severity. A reduced flow can occur if there is any disease in the peripheral vascular bed (microvascular disease), which would elevate FFR. From a diagnostic point of view, this may appear to be false negative, i.e., diseased patient seen as healthy. However, the purpose of FFR is to detect a focal flow-limiting stenosis for which percutaneous coronary intervention is effective. The relatively high FFR in such a scenario – indicating the stenosis being not flow-limiting or not flow-limiting enough to justify PCI– still provides a valid indication because this the reduced flow in this case is not due to the stenosis but to the microvascular disease.

The simulations using the PET perfusion-based boundary conditions take into account the patient-specific distribution of the flow across the different branches and the change in flow rate from normal physiological state to hyperaemia. The FFR obtained using the PBCs are in general higher than the FFRs with conventional boundary conditions. This is because the hyperaemic response in reality is generally less than 4 with a wide range standard deviation of 0.9)[130] and the PET perfusion boundary conditions reflect that. Clinically evaluated CFRs of our patients' diseased vessels are 2.12 ± 1.28 , indicating that the conventional assumption, i.e., $CFR=4$, is indeed an overestimate. However, in patients 3 and 10, the FFR values obtained using PBC are lower than those using MBC. Even though the conventional boundary conditions make the assumption of the ideal vasodilatory condition (4x the baseline flow), the baseline flow for the diseased branch may be higher in the model with PBC than with MBC, and therefore even with a reduced vasodilatory condition with PBC (<4x), the absolute hyperaemic flow across the diseased branch can be higher than that of the conventional model as shown in Table 5, causing a larger pressure drop and hence lower FFR. This is indeed true for those 2 patients, suggesting that the myocardium downstream to those vessels are still healthy despite the stenosis in its upstream, making these cases as illustrative examples of 'flow-limiting' stenosis that should ideally be detected by FFR. The flow through the diseased branch of those patients is underestimated with the conventional MBC, thus potentially causing false

negative – indeed, the FFR of MBCs are higher than the cutoff 0.8 and that with PBC is lower. To make the analysis framework more accurate, this group of patients need to be looked at for further characterisation.

The PBC-based FFRs generally fall within the range of FFR calculated using the varied MBC (30%-90%). The patients where the PET perfusion model predicts an FFR that is outside the bounds all have a higher flow through the stenosed branch compared to the computations with MBC. The method of ranging the hyperaemic response to obtain a lower and upper bound of FFR could therefore be useful approach to have a 'confidence interval' of FFR calculation. From clinical diagnostic point of view, it is particularly concerning when the range of FFR for a particular patient's stenosis straddles the cutoff value 0.9. The largest variance in FFR can be found in Patient 10, specifically with the LAD (0.56-0.78), however the bounds do not cross over the cut off and therefore it is unlikely to affect clinical decisions. For the LCx of Patient 10, while the variance is not as high, the range is across the clinical cutoff of 0.8 (0.74 – 0.88).

Lastly, whilst PET perfusion can identify the presence of ischaemia, it cannot necessarily identify whether the ischaemia is caused by an epicardial stenosis, epicardial diffuse disease, microvascular disease or in rare cases existing tissue damage or fibrosis[136]. That being said, alternative indicators may help suggest whether the flow impairment is caused by an epicardial issue or downstream defect.

Of particular importance are the patients where the varied boundary conditions produced FFR values that straddle the diagnostic threshold FFR of 0.8. For these cases, it is worth looking at the PET perfusion data directly and observe whether they are likely to produce the same diagnosis.

Table 5-7 2-element Windkessel model in electrical terms. I(t) represent the current, P(t) is the potential difference across the two points, C is the capacitance and R is the electrical resistance.

Patient	CTCA measured stenosis	Conventional FFRCT (MBC 30%)	FFRCT Range (MBC 30-90%)	FFRCT (PBC)	Absolute Perfusion	CFR	Pseudo IFR/ Rest Pd/pa
1 (RCA)	Grey	Green	Green	Green	Green	Orange	Green
2 (LAD)	Green	Green	Green	Green	Green	Green	Green
3 (LAD)	Orange	Light Green	Light Green	Light Orange	Orange	Orange	Orange
4 (LAD)	Green	Green	Green	Green	Grey	Green	Green
5 (RCA)	Orange	Orange	Orange	Orange	Grey	Orange	Orange
6 (LAD)	Green	Green	Green	Green	Green	Green	Green
7 (LAD)	Green	Green	Green	Green	Grey	Grey	Green
8 (RCA)	Green	Green	Green	Green	Green	Green	Green
9 (RCA)	Green	Green	Green	Green	Green	Green	Green
10 (LAD)	Grey	Orange	Orange	Orange	Orange	Orange	Orange
10 (LCX)	Grey	Light Green	Light Green	Orange	Grey	Orange	Grey

5.5.2. PET Perfusion and coronary flow reserve comparison to verify the computed FFR values

This study was conducted primarily as a sensitivity test of FFR computations to the outflow boundary conditions. Since there was no gold-standard data such as invasive FFR values, it was not possible to evaluate the absolute error of the predicted FFR. However, in light of assessing the

validity of the predicted FFR, a verification based on the perfusion observation using PET measurement is conducted.

In *Table 5-2*, Patient 3 for example has a very low flow reserve observed by both the vessel-specific sampling and the regional sampling by the stenosed LAD. Whilst flow reserve does not directly indicate epicardial disease, there is substantial evidence that indicates microvascular disease tend not to be localised to a single vessel or region but rather the whole organ or even systemic (across various organs)[137]. Therefore, when we observe that the flow reserve for the regions supplied by the LCX and RCA being well above the clinical threshold of CFR < 2.00, it is highly likely that the LAD is indeed affected by an epicardial vessel defect, and in the case of Patient 3, it has already been identified that there is a significant stenosis observed in the CT coronary angiography. These observations support the indication by the computed FFR values (*Table 5-4*).

Patient 10's LCX, on the other hand, is more of an ambiguous case. The region supplied by the stenosed vessel (left coronary territory) does have a lower flow reserve than the region supplied by the RCA that does not have a stenosis. Whilst the CFR in left coronary region is not significantly lower locally, CFRs in all regions supplied by the three major vessels are unanimously below the CFR < 2.00 threshold. This suggests that the stenoses observed in the CTCA – in LAD and LCx – may be considered minor therefore unlikely to require revascularisation, but likely a combination of diffuse disease and microvascular disease.

For the remaining patients, the perfusion data can also assist in confirming whether the simulated FFR is appropriate. Patients 2, 4, 6, 7, 8, 9 all have very mild angiographically observed stenoses, and their functional severity turned out non-significant as in their high FFR values >0.80. The flow reserves of the regions supplied by the suspected vessels are also all above the clinical threshold of 2.0, with the exception of patient 7 with a lowered flow reserve of 1.58. However, when sampling the region supplied by the branch downstream of the stenosis, the flow reserve was 1.89 which would make it a borderline case. Combined with the fact that the LCX and

RCA regions also have borderline flow reserves of 2.04 and 2.01 respectively, it is unlikely that the ~9% stenosis of Patient 7's LAD is functionally significant.

Conversely for more severely affected patients that have simulated FFR values less than the diagnostic threshold of 0.8 and therefore likely requires revascularisation, the perfusion data also heavily supports this diagnostic result. Patient 5 has a significant angiographically measured RCA stenosis of 73% constriction, and observing the flow reserves of 1.15 and 1.21, quantified as the entire RCA territory and the vessel specific sampling, respectively. These CFR values indicate a low flow reserve that stand out in comparison to the other regions (LAD and LCX). However, as all regions have flow reserves below 2.00, it is likely that patient 5 also suffers from microvascular disease, and therefore whilst the stenosis does require revascularisation, the upper bound of the FFR estimation: 0.75 is near the low end of the FFR "grey zone".

Lastly, patient 10's LAD has the most severe case of a focal stenosis, this is indicated by its markedly low flow reserve even below 1, observed by both the regional flow reserve, 0.65, and vessel specific flow reserve, 0.81. A flow reserve below 1 is rare as it suggests that the addition of vasodilators reduce the flow going through the affected vessel. This is due to the adaptation of significantly constricted vessels to dilate permanently, including during the rest state, to maintain sufficient blood flow to the myocardium. When vasodilators are used, the adapted vessels that are already at its limit of vasodilation, cannot dilate further, whilst neighbouring vessels that were unaffected by the stenosis will dilate, lowering their downstream resistance significantly [138]. Given the same or similar cardiac output, these newly dilated vessels will essentially draw more flow leaving the vessel with vasodilatory dysfunction with less flow than before. This phenomenon, though rare, has been observed and is called "Coronary Steal".[139,140]

5.5.3. Resting Pd/Pa and CT-based iFR comparison

Lastly, building on the work of the previous chapter, it was noted that Rest-state Pd/Pa in a steady inflow simulation tended to approximate iFR better than the true averaged Resting Pd/Pa in a pulsatile simulation. It is worth looking at the MBC 100%, essentially no vasodilation to see whether that consistently indicates the diagnostic results produced by the various FFR schemes, direct perfusion, and PET-based flow reserve.

In most cases, CT-based iFR shows high concordance with conventional FFRCT with one exception of Patient 3 whose FFR is on the borderline (FFR = 0.81) whereas the CT-based iFR/Resting Pd/Pa (= 0.85) is clearly below the cut-off of 0.89. It also confirms diagnostic result from the PET based boundary conditions, CFR, and absolute perfusion.

5.5.4. Final comments

It should be noted that PET perfusion or other similar myocardial perfusion imaging generally supersedes FFR measurement obtained both invasively or non-invasively [141]. It is rare in the clinic that both of those are performed before a diagnostic judgement is made, due to the cost and time it requires. The comparison in this study is not to suggest that a perfusion based FFRCT model should be adopted as clinical practice, but rather verifying the flow condition estimation in the downstream of the coronary arteries using purely morphological methods. That being said, there have been clinical studies that implement myocardial perfusion imaging in cases where FFRCT provided an ambiguous indication, and has shown a noticeable improvement in diagnostic accuracy [142].

Among patients having stable angina, 65% of women and 32% of men have no obstructive CAD (stenosis <50%) [12]. A significant portion of those patients suffer from coronary microvascular dysfunction which can be ischaemia without a focal stenosis [12]. This means that a significant number of patients would not be best served by current CT-based FFR techniques that make the assumption of ideal downstream microvascular health. Because the assumption uses the maximal possible vasodilation, for

patients whose vasodilatory response is impaired, the simulation would overestimate the flow passing through a stenosis, producing a lower FFR than the true value, potentially leading to false positive diagnosis and hence an unnecessary invasive revascularisation.

Although the FAME trials – the original and main clinical trial for FFR – suggest a strict 0.8 cut-off, following studies have since suggested that clinicians should be aware of the biological variability of FFR measurements, where repeated measurements will produce different values and possibly different diagnostic outcomes [143]. It has been suggested that there should be a grey zone around the cut-off, considered to be between 0.75 and 0.80, with particular caution given to values between 0.77 and 0.83, where the clinician will need to consider other patient metrics before deciding treatment [143]. This study has examined one major consideration that can have a drastic effect on CT-based FFR: the vasodilatory capacity of the patient's microvasculature. The PET perfusion-based model has shown that the majority of patient's microvascular health is between ideal and diseased, based on their CFR. In the clinic, additional assessment of microvascular health through testing or identifying risk factors such as diabetes, age, sex could be used to inform CT-based FFR measurements directly, producing a possibly more reliable FFR value, and if that is not available, a similar approach to this study where a band of FFR values can be produced to identify the likelihood that a stenosis falls below the cut-off.

5.6. Limitations

The main limitation of this investigation is that the FFRCT values for the patients were not validated against invasive FFR, the gold standard for FFR. The study was primarily designed as a sensitivity test, examining the variability of FFR in simulation based FFRCT with various outflow boundary conditions. As the best attempt to verify the predictive outcome of the CT-based FFR, the results were instead compared against perfusion-based outcomes.

Additionally, FFR measurement itself has limitations. A typical one is diffuse disease, where the narrowing is not focal but spread along an artery, which is also a known cause of ischaemia. The pressure drops across a diffused stenosis can be as severe as those of focal stenoses, however revascularization of diffuse disease has shown mixed results and therefore FFR is not applicable for these patients [144].

In terms of modelling method, assumptions other than those with boundary conditions are inevitable. The flows were simulated with steady flow condition using Newtonian approximation of the blood. As discussed in the method section, these are not deemed significant in FFR computation but would carry more importance in analyses of stented segment with potentially larger flow recirculation, and/or of patients with cardiac rhythm disorders.

Lastly, the finding from the study still need to be confirmed with a larger number of patients, which is planned for future.

5.6.1. 82-Rb PET and PET perfusion cut-offs

Whilst PET perfusion is well established as the best non-invasive imaging technique to diagnose coronary artery disease, 82Rb PET is not as well validated as alternatives like 15-O(Water) and 13-N(Ammonia) PET for the purpose of measuring both absolute myocardial flow/perfusion and myocardial flow reserve [145]. This is due to its nonlinear uptake versus flow relationship that requires additional processing using algorithms that currently still produce quite varied results depending on the software used [146]. A comprehensive study on inter-software variability of three major software packages (including Syngo.via that was used in this patient dataset) on 82-Rb perfusion imaging shows a kappa statistic upper bound agreement of 53% and lower bound of 34% when using the flow reserve CAD diagnostic cut off of <2.00 , suggesting variable perfusion values even for the same PET image [146].

Additionally, the CFR cut-off for ischaemia is not as well agreed upon like it is for FFR, in a review of multiple PET perfusion studies [147], a large

range of CFR cut-offs was identified from 1.44 to 2.74, and an absolute stress perfusion cut-off of 0.91 to 1.86 ml/g/min.

5.7. Summary

In this chapter, a series of computational FFR analysis was conducted using various outflow boundary condition to investigate their impact on the FFR derivation. The FFRs computed with a conventional morphology-based and the novel PET-based outflow boundary conditions agreed in general. However, the models with PET-based condition revealed that there are, though rare, cases in which conventional boundary condition underestimate the functional severity of a stenosis, potentially placing the patient in different diagnostic category. The proposed method to derive a potential range of FFR a patient might have, by varying peripheral resistance over a physiologically possible range, successfully capture the FFRs derived with PET-based outflow conditions. The method has demonstrated therefore its potential to compensate the lack of perfusion data in analysis.

Chapter 6. **Optimising accuracy of FFRCT without the use of perfusion-based imaging methods**

6.1. Introduction

6.1.1. Purpose

In this final chapter the aim is to develop an approach to FFRCT simulation that improves upon what is currently used in the clinic. In particular, there are three main areas of improvement: 1) to better utilise and implement patient information not previously used, 2) to improve the specificity of the technique in the “grey area”, i.e., FFR value around the threshold 0.8, and 3) to create a FFRCT solution that a clinician can more confidently assess and utilise.

In conventional approaches to FFRCT such as the one used by HeartFlow [44,70,148], the only information that is used are the CT Coronary Angiogram (CTCA) images that shows anatomy, as well as cardiac metrics such as blood pressure and heart rate. However, it has been reported that conventional FFRCT algorithm often overestimates the severity of a stenosis for patients that suffer from microvascular disease [108].

Although the works presented in the previous chapter demonstrate that perfusion imaging can provide vital information in determining vasodilatory effect of the downstream resistance boundary condition at hyperaemia, a necessary condition for FFR, myocardial perfusion imaging (MPI) is generally used independently of FFR and is considered the gold standard for ischaemia detection [145]. It should however be noted that FFRCT is not inferior to PET perfusion imaging for per-vessel ischaemia diagnosis [149] and in cases of multi-vessel disease where the source of ischaemia is not as easily identifiable, FFRCT can actually be of greater utility in deciding revascularisation strategy [136].

It is also clinically nonviable to require perfusion imaging for the purpose of providing outflow boundary conditions (BC) for FFRCT which is intended to be a much more routine technique that is used on patients with moderate disease that CTCA cannot accurately diagnose. As CTCA is recommended by medical bodies such as UK's NICE as the first line investigation for suspected CAD patients [11] and FFRCT uses solely CTCA images, it therefore does not incur additional radioactive dose to the patient, nor additional imaging.

It is therefore ideal to observe how the vasodilatory capacity of the microvasculature of a patient is associated with demographic metrics such as age, sex, heart rate, blood pressure, comorbidities, family history, smoker status etc., based on perfusion imaging for each patient and to guide the boundary conditions required for FFRCT.

The patient dataset from the previous chapters contains above-mentioned metrics and perfusion (PET) imaging of each patient with their coronary flow reserves (CFR) calculated. Using the full data set – 101 patients in total – rather than the selected small group in Chapters 4 and 5, the extent to which these metrics can act as surrogate may become evident and a statistical model can be derived to estimate the microvascular flow response to hyperaemia.

Additionally, in this chapter, a new dataset of CAD patients that underwent CTCA and CT perfusion imaging is referred as a point of comparison to test the hyperaemic flow model devised. This dataset also includes invasive FFR testing, the gold standard measure for the functional significance of a coronary artery stenosis, which would allow the FFRCT values produced to be validated against.

Finally, producing a FFRCT value that is closer to the invasive FFR in absolute terms will obviously provide confidence to the clinician using the method, however it is also crucial to observe whether the diagnostic accuracy is improved compared to the conventional FFRCT method, and whether it is possible to quantify in a statistical manner the likelihood of a FFRCT diagnostic result to be correct or incorrect.

6.1.2. Difference between CFR and response to hyperaemia in outlet boundary conditions

In this chapter, Coronary Flow Reserve (CFR), hyperaemic flow response and microvascular vasodilatory capacity/response represent similar concepts and sometimes used interchangeably, but there are contexts where these may differ.

One crucial element is that while CFR is the flow response to hyperaemia, i.e., the proportional increase in coronary flow during hyperaemia, it is related but not necessarily equal to the outflow boundary conditions in CFD, where microvascular resistance is lowered to simulate vasodilation. In the Windkessel boundary condition, the resistance element represents only the resistive part of the coronary branch downstream, the microvasculature, to the main sections of the blood vessel represented by 3D anatomical model in CFD whereas CFR takes into account the whole coronary tree from the aortic root to the microvasculature.

As suggested in the previous chapter, when the CFR of the patient's entire myocardium and for each myocardial region supplied by each artery are known, the downstream microvascular dilatory response to hyperaemia can be matched to the CFR accordingly, with the exception of the stenosed branch. In a branch with a stenosis, both the stenosis itself and the downstream microvascular dilation contributes to the CFR value of that artery/supplied region. To isolate the downstream microvascular dilation such that an accurate reduction of resistance can be set in the resistance boundary condition, it is useful to use other regional CFRs as a proxy to the microvascular dilatory capacity of the stenosed branch. This is because microvascular condition tends to be well correlated across all branches, with any microvascular defects tending to be global rather than localised[150].

6.1.3. CT Perfusion

Along with PET and SPECT myocardial blood flow/perfusion imaging, CT myocardial perfusion imaging has been a recent development in CT technology that aims to provide a similar ischaemia assessment. Iodinated contrast distribution during the first pass through the myocardium is determined by coronary circulation, areas with reduced contrast will show a lower attenuation and therefore identify areas of possible malperfusion. [151]

There are numerous advantages of CT perfusion imaging: imaging protocols can incorporate multiple image types such as CT perfusion, CT Angiography, Dynamic/Static etc, producing multiple means to assess a patient's cardiac health in one scanning session, reducing the number of machines, manpower and time required. [152] An example of CT perfusion shown alongside CT Angiography is shown in Figure 6-1

In this study, a CT perfusion patient dataset was available with invasive FFR measurements allowing a comparison of FFRCT using a perfusion based model and the gold standard FFR.

6.2. Method

6.2.1. Patient dataset

For this analysis two patient datasets were used:

PET perfusion dataset: (101 Patients, 65 male, 36 female, Age: 70 ±9)

The PET perfusion dataset used in the previous chapter is used here to produce a statistical model of CFR, as a function of demographic parameters, based on a realistic patient population (as opposed to general population including both healthy and diseased). The CFR values in this dataset were calculated clinically using Siemens Syngo.PET platform for every patient, and even for the ROI of each major branch. The dataset's size and a wide range of patient metrics labelled such as Age, Sex, Smoking status, Diabetes, Family history etc. are sufficient to determine the contribution of these metrics to a patient's CFR value using regression techniques, ultimately producing a patient specific estimate of CFR.

The limitation of this dataset is that these patients did not undergo invasive FFR testing, and therefore any FFRCT simulation technique cannot be validated against the gold standard. Therefore, a separate dataset that has invasive FFR should be used to test the simulation assumptions produced from this dataset.

CT perfusion dataset: (10 patients, 10 male, Age: 59±6)

In this chapter, the patient dataset consists of 10 patients that have undergone CTCA and CT perfusion (stress and rest) imaging (Siemens SOMATOM Definition Flash) for suspected coronary artery disease. The CT perfusion dataset whilst not the gold standard for perfusion imaging, has every patient undergone invasive FFR, as well as a built-in FFRCT algorithm (Siemens cFFR version 1.4, not commercially available). The perfusion data will also in addition serve as a benchmark for the CFR estimation as the data also contain the same patient metrics relevant to predicting CFR. The full CFD simulations performed in this chapter will use the geometries produced from the CT images of this dataset. The methods of meshing and simulation setup are the same as those of the previous chapters.

6.2.2. Perfusion estimation from CT perfusion

CT perfusion images whilst not being the gold standard for perfusion imaging, and is not currently widely used clinically, does have some advantages compared to PET perfusion imaging and especially beneficial to our perfusion based FFRCT method.

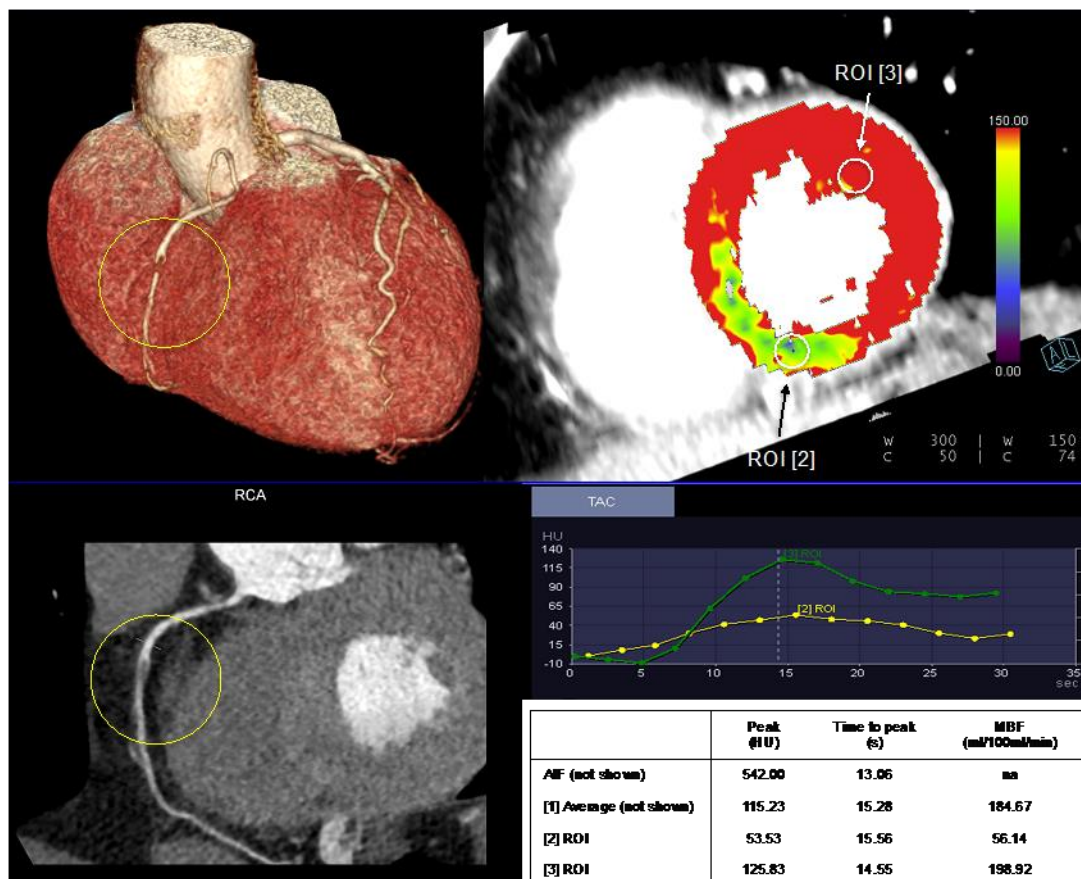


Figure 6-1 (Top left) 3D rendering of CTCA, (Top right) CT myocardial perfusion, (Bottom left) CTCA slice, (Bottom right) CT dynamic perfusion chart) from [181]

CT perfusion imaging though having a lower 3D resolution than CT coronary angiograms, have far superior resolution to PET perfusion imaging. As the resolution is high enough: 0.38mm x 0.38mm x 2mm there is not a need to co-register CT perfusion and CTCA Images to find the location of the coronary outlets. For the CT perfusion imaging datasets, major coronary arteries and branches are identifiable directly, and as the CT angiograms and the CT perfusion images are taken on the same machine, they can be quite easily superimposed if needed.

Please refer to the section 5.3.5 in the previous chapter for how flow supplied by an artery is calculated. Another advantage of this dataset is that the perfusion values have already been calculated using the Siemens software package, *Syngo.CT Myocardial Perfusion*, accompanying the CT perfusion machine.

One important step to note is that the images taken at rest and stress may not be aligned, therefore when calculating CFR, i.e., when dividing the stress perfusion by the rest perfusion for any given region, the images cannot be divided directly. However, returning to the method proposed in section 5.3.5, the approximate ROI for each branch is identified in the CTCA image taken at rest will correspond to the correct CT perfusion ROI at rest, and performing the same process for stress will produce corresponding perfusion values for each branches' ROI in both states.

6.2.3. Inflow conditions

The inflow boundary condition is the same as that of the previous chapters, a steady flow that corresponds to the patient-specific stroke volume estimated by the systolic-diastolic difference of left ventricular cavity volumes based on CTCA. As total cardiac output does affect FFRCT performance for the same coronary tree volume [135], it is vital to incorporate any patient metrics possible to estimate cardiac output.

As shown in Chapter 4, where a full range dynamic CT has been performed, it is possible to segment the LV cavity for its change in size between diastole and systole, i.e., stroke volume. As heart rate is almost always known, it can simply be multiplied with the stroke volume to obtain cardiac output.

Alternatively, Stress Echocardiography, a routine procedure for most CAD patients, and for medical institutions guided by the ESC, the first line investigation for suspected CAD, can predict cardiac output directly.

However, in this dataset, neither was available, and as the intention is to create a scheme where the result can be replicated without necessarily

having these additional modalities available, an estimation of cardiac output using height and weight was implemented [129].

$$BSA = \sqrt{\frac{Height(cm) \times Weight(kg)}{3600}} \quad (20)$$

$$CO = 3.06BSA + 0.37 \quad (21)$$

BSA is body surface area (m²), and CO is cardiac output (l/min)

6.2.4. Outflow conditions

The approach to outflow boundary conditions is unchanged from the previous chapters, the only difference is the way the vasodilatory factor (reduction in downstream microvascular resistance due to hyperaemia) is applied to each of the coronary outlets. The increase in flow for each branch during hyperaemia is shown in an example in *Figure 6-2*.

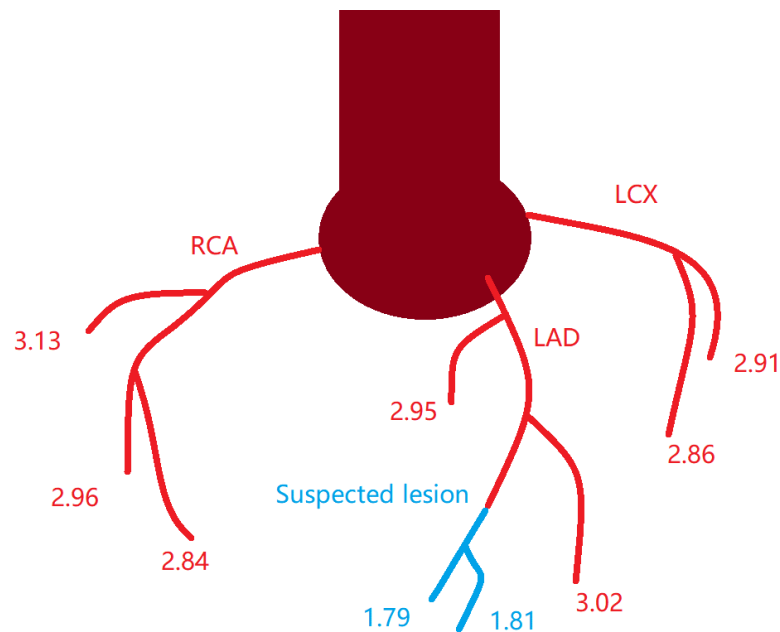


Figure 6-2 The ratio of flow during hyperaemia and rest, the Coronary Flow Reserve (CFR) of each branch outlet as measured. The values shown are just an example and does not represent any particular patient case.

6.2.5. Outflow BC with response to hyperaemia based on general population average (conventional FFRCT assumption)

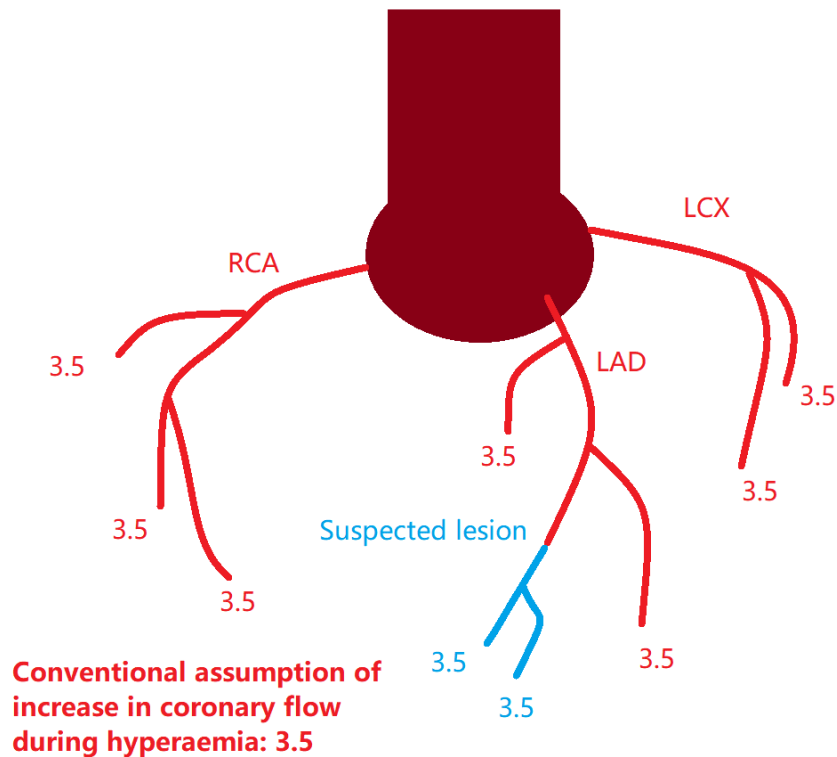
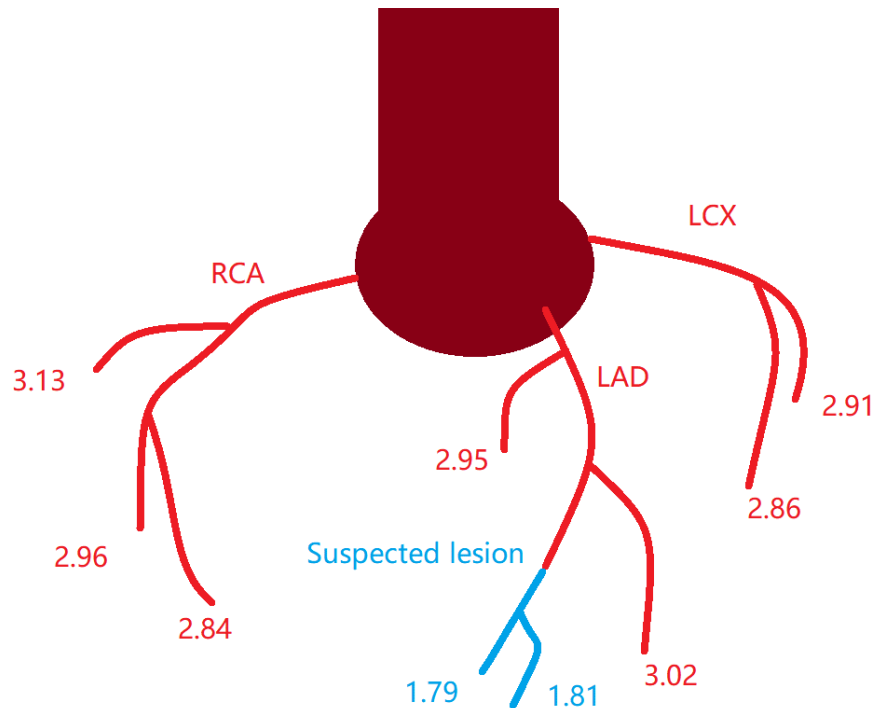


Figure 6-3 The conventional assumption of flow magnitude increase during hyperaemia is applied to the downstream resistance boundary condition. The resistance boundary condition is decreased by this value.

This is the “conventional” model (shown in Figure 6-3) of outflow BC that is used by commercial FFRCT such as HeartFlow [108], where the flow response to hyperaemia is based on a population average response of 3.5, i.e. coronary outlet resistance during hyperaemia drops to 0.29x its resistance during rest.

6.2.6. Outflow BC with adjusted response to hyperaemia based on patient-specific CT perfusion imaging – target branch:



The CFR measured at each outlet will be applied as the downstream resistance reduction.

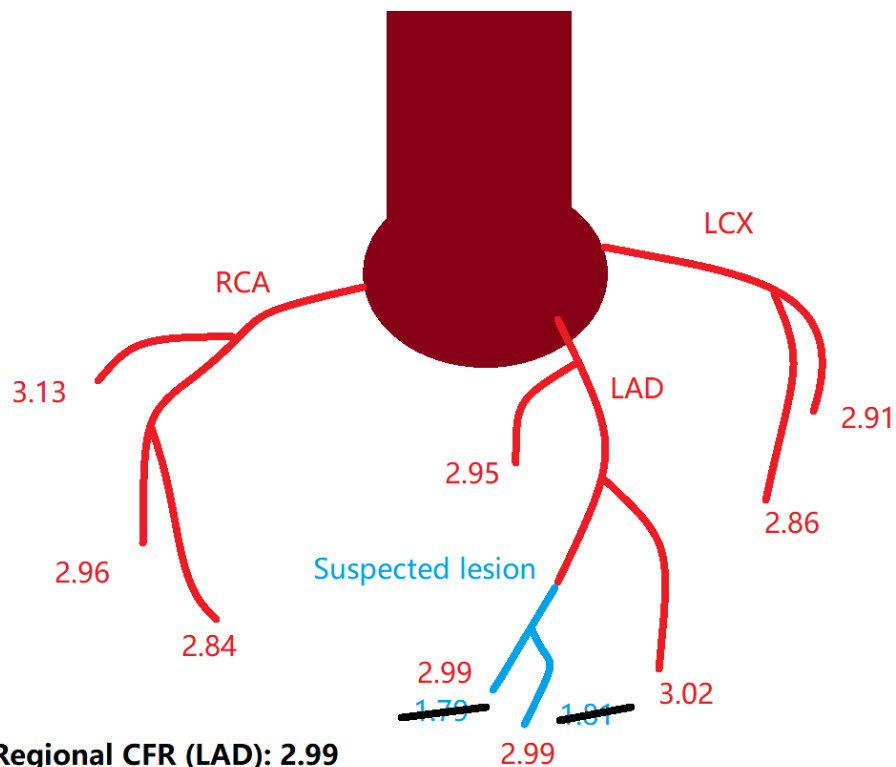
Figure 6-4 The measured (from perfusion imaging) flow magnitude increase during hyperaemia is applied to the corresponding resistance boundary condition. The resistance boundary condition is decreased by this value.

In this BC, CT perfusion imaging was used to identify the precise increase in coronary flow due to induced hyperaemia via adenosine compared to the flow at rest. This response values are observed for every outlet branch in the CT Image and is applied to the outlet boundary conditions of each branch in the simulation shown in Figure 6-4.

There is however one downside to this: CFR measures the change in flow due to hyperaemia, it captures both the upstream section of the coronary arteries – resolved in CTCA – and its microvascular outlets. In our simulation, however, the upstream section of the coronary arteries is represented by its 3D geometry, taking into account any obstructions, or narrowing. The reduction in resistance of the outlet boundary condition

concerns only the microvasculature, and therefore using CFR directly as a proxy for the proportional change in resistance makes erroneous assumption that the upstream section does not contribute to CFR.

6.2.7. Outflow BC with adjusted response to hyperaemia based on patient-specific CT perfusion imaging – regional



Regional CFR (LAD): 2.99

(Use the average CFR as the hyperaemic flow response of the artery with the suspected lesion whilst excluding the branches downstream, apply that response to the boundaries downstream.)

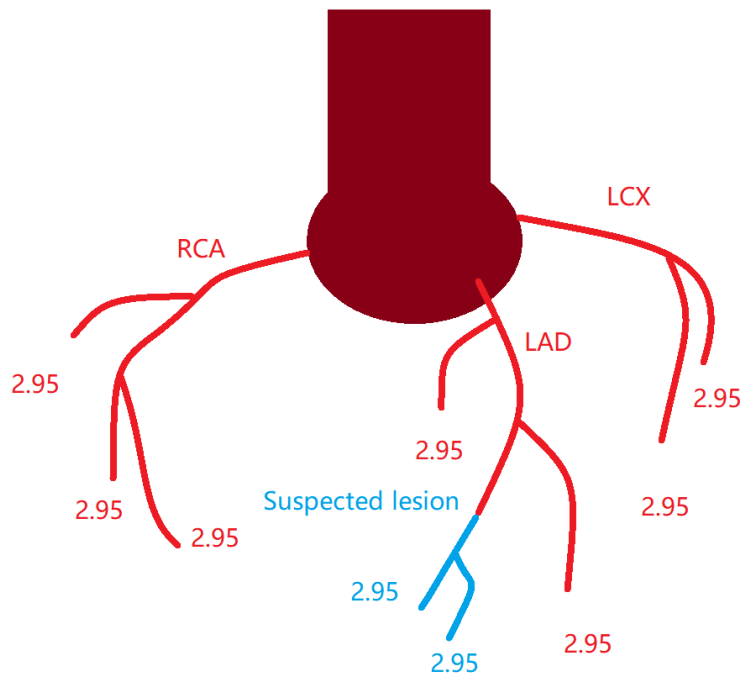
Figure 6-5 The measured (from perfusion imaging) flow magnitude increase during hyperaemia is applied to the corresponding resistance boundary condition. The resistance boundary condition is decreased by this value. However, the branches downstream of the suspected lesion will use the average flow increase of the other branches in the artery, in this case, the LAD, where the other branches show an increase of 3.02 and 2.95, averaging 2.99.

Similarly, to the outflow BC above, this condition instead reflects regional differences in CFR between the regions supplied by the RCA, LAD and LCX. The CFR of each outlet branch measured in the CT Perfusion

images is averaged for a regional CFR which is then applied back to the outlet boundary conditions of our CT-based flow simulation (*Figure 6-5*).

The advantage of using a regional based response to hyperaemia for our simulations is that it overcomes the weaknesses of the branch-wise BC, where it helps to overcome potentially large variabilities in CFR due to poor positioning of our perfusion measurement spheres. The second advantage is that by averaging out the regional CFR, it will help mitigate the issue concerning the inability to separate whether a low value of CFR is due to microvascular dysfunction or a specific obstruction in the main artery.

6.2.8. Outflow BC with adjusted response to hyperaemia based on patient-specific CT perfusion imaging – global



Average measured CFR of all branches (excluding branches downstream of suspected lesion): 2.95

Figure 6-6 The measured (from perfusion imaging) flow magnitude increase during hyperaemia is averaged before being applied to the corresponding resistance boundary condition. The resistance boundary condition is decreased by this value. The measured flow increases of the branches downstream of the suspected lesion are excluded from the average.

In this model of BC, instead of assigning CFR value to each branch's outlet boundary conditions, CFR values are averaged out to form a global "response to hyperaemia" value that is applied homogenously to all outlets, like in *Figure 6-6*.

This approach further mitigates the problem with the disparity between CFR and microvascular dilatory response to hyperaemia, as well as mitigating the effect of potential mismeasurement of outlet perfusion from the CT perfusion images.

Lastly, this approach most likely reflects the nature of microvascular function, where any dysfunction is likely uniform across the whole myocardium rather than severe microvascular dysfunction in one region or branch but healthy microvascular function elsewhere [150]. This is also well supported by our PET perfusion dataset which has a large volume of patients with CFRs of each cardiac region (RCA, LAD, LCX) calculated. Across 101 patients, the average standard deviation of CFR between the three regions is 0.13 ± 0.08 . This assumption is also in line with the assumption used in conventional FFRCT [108,148], though they make the additional assumption that the average CAD patient has microvascular function representative of the general population.

6.2.9. Outflow BC with adjusted response to hyperaemia based on patient population average

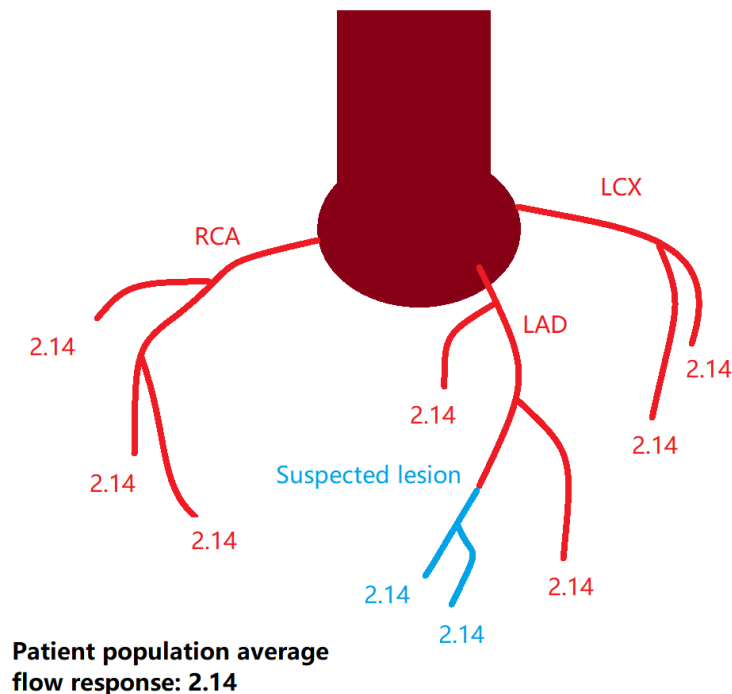


Figure 6-7 The patient population average CFR is applied to all branches. The resistance boundary condition is decreased by this value.

This BC is similar to the conventional outflow BC except the microvascular resistance response to hyperaemia uses a patient population average $\sim 2.14 \pm 0.51$ rather than general population average ~ 3.5 , example shown in Figure 6-7. Additionally, for this BC, since the variation of CFR across the patient population is known, an additional advantage is expected by performing the simulations with the statistical variability in the response to hyperaemia. This simulation would therefore produce a range of FFRCT values where the patient's "true" invasive FFR would likely lie within.

Clinically, this would aid decision making where currently decisions are made on a singular FFR value and compared to the FFR threshold of 0.8, as well as using clinical judgement based on other observations. With a range as well as a well-defined distribution of FFR values, the clinician can

not only see whether the most likely FFR value based on simulation is above or below the threshold, but also determine the probability that the true FFR value is above or below the threshold, creating an additional level of confidence.

6.2.10. Outflow BC with adjusted response to hyperaemia based on patient-specific demographic metrics

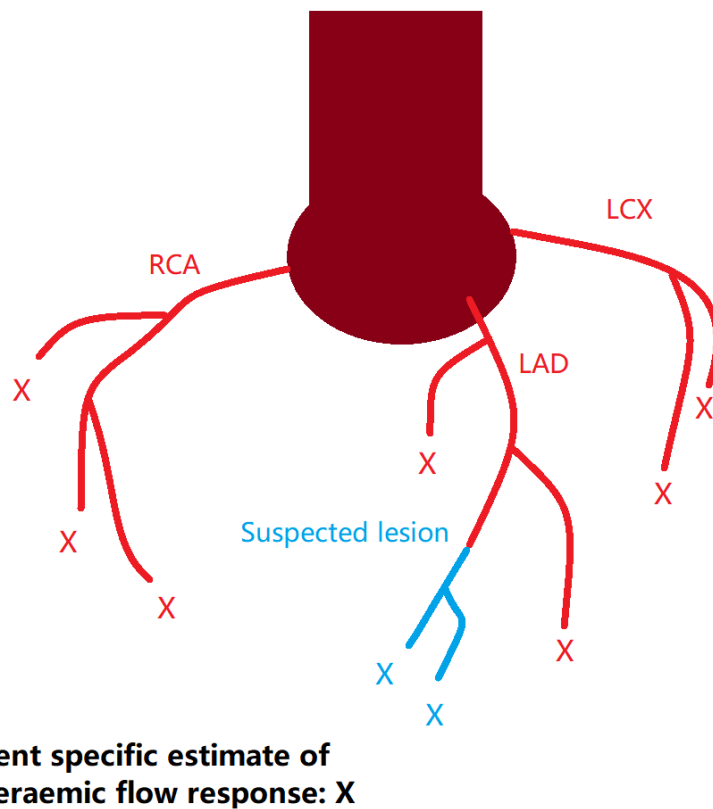


Figure 6-8 The patient specific estimate of hyperaemic flow increase is applied to all branches. The resistance boundary condition is decreased by this value. The estimate uses patient metrics and patient population data to calculate a patient specific value.

This BC is similar to the one that uses patient population average response to hyperaemia in its outlet boundary conditions. However, the response value is adjusted based on patient specific metrics that have been found to influence this value such as sex, diabetes, and smoking status.

This response value will therefore be patient-specific, but a uniform proportion across all branches as indicated in Figure 6-8

Simulations using this BC are used to assess whether there is any benefit to finetuning the response the hyperaemia based on patient specific information, whether it will bring the simulated FFR value closer to the true value, but without the use of perfusion-based imaging data.

6.2.11. Patient specific flow response and patient metrics

The boundary conditions set will have to use data that is readily available for a patient that undergoes a CT coronary angiography. This would be typical health metrics such as, height, weight, age, sex, heart rate, blood pressure, and other medical conditions and health indicators etc. The list of metrics that were consistently measured across all patients in the dataset (those patients with missing data points were excluded) are listed in the **Table 6-1**. This was first performed using univariate regression on each variable from the PET perfusion dataset against the CFR value (n=101). In **Table 6-2, Table 6-3**, multiple regression was applied to the variables that were statistically significant individually. The final regression model was produced in **Table 6-4**.

Table 6-1 Regression coefficients, error, and significance of various patient metrics on the overall CFR (excluding suspected branch) of a patient. This was calculated using the PET perfusion data set (n = 101), performing univariate regression on each data point individually. Coloured cells indicate the statistically significant coefficients (P value \sim <0.1).

	<i>Coefficients</i>	<i>Standard Error</i>	<i>P-value</i>
Age	-0.0098	0.0051	0.0583
Sex	0.2302	0.0998	0.0231
Pain limitation	-0.1440	0.0968	0.1401
Breathlessness	-0.1237	0.0970	0.2051
Diabetes	-0.3334	0.1131	0.0040
Smoker	0.2917	0.1106	0.0097
Hypertension	-0.1949	0.0965	0.0461
Hyperlipidaemia	-0.0753	0.0991	0.4488
Family History	0.0651	0.0975	0.5063
Rest HR	-0.0061	0.0038	0.1090
Rest Systolic BP	-0.0037	0.0022	0.0953
Rest Diastolic BP	-0.0019	0.0039	0.6293
Stress HR	0.0010	0.0030	0.7459
Stress Systolic BP	-0.0036	0.0024	0.1362
Stress Diastolic BP	-0.0046	0.0042	0.2688

Table 6-2 Multiple regression of the variables that were statistically significant in Table 6-1. The least significant variable is removed to perform the following step in Table 6-3.

	<i>Coefficients</i>	<i>Standard Error</i>	<i>P-value</i>
age	-0.0017	0.0051	0.7371
sex	0.2015	0.0960	0.0386
diabetes	-0.2859	0.1096	0.0106
smoking	0.2474	0.1083	0.0246
hypertension	-0.1251	0.0915	0.1747

Table 6-3 Multiple regression of the remaining variables, hypertension’s influence on the patient’s CFR is not significant and is further knocked out to produce the final model in Table 6-4.

	<i>Coefficients</i>	<i>Standard Error</i>	<i>P-value</i>
sex	0.2084	0.0934	0.0281
diabetes	-0.2906	0.1082	0.0085
smoker	0.2566	0.1043	0.0156
hypertension	-0.1280	0.0907	0.1614

Table 6-4 Regression coefficients, Standard Error and P-value of a reduced model that utilises only variables have a significance of P<0.05

	<i>Coefficients</i>	<i>Standard Error</i>	<i>P-value</i>
Intercept	1.95	0.253	<0.001
Sex (1 if male)	0.22	0.093	0.019782
Diabetes status	-0.30	0.107	0.005022
Smoker status	0.265	0.104	0.012905

6.2.12. Age

Regression coefficient for age (for each year): -0.0017(0.051) (P value = 0.74)

Whilst it is well documented that CFR generally declines with age [153], however when controlling for other health indicators and metrics it does not seem to be the case in our patient population. This may be due to a number of reasons: (1) The patient dataset has a relatively limited age range (70+- 9) with no patient under the age of 50, (2) age-related reasons for lower CFR are due to older individuals’ likelihood to have comorbidities that have been isolated in our regression [153], and (3) selection bias, whilst lower CFR with age may be true for the general population, when “selection” into the patient population,(e.g. the exhibiting of symptoms AND severity of symptoms to justify a referral to a perfusion imaging scan) may eliminate any age-related CFR effects.

6.2.13. Sex

Regression coefficient for male sex (as opposed to female): +0.22(0.09)

It has been documented that women exhibiting cardiovascular disease symptoms have a much higher probability of having microvascular dysfunction relative to male patients [154]. Note that this is not to suggest that coronary microvascular dysfunction (CMD) is a uniquely female disease or even more prevalent among women. The prevalence of CMD in both sexes have been shown to be comparable, the higher rates of CMD among the female patient population relative to the male patient population is due to more men becoming patients due to symptoms being caused by other cardiovascular conditions.

CFR, the increase in flow response to hyperaemia, takes into account any restriction in the epicardial vessels as well as microvascular dilatory capacity, the two most common metrics to measure these being FFR and IMR see chapter 2 respectively. However, when these are controlled for, i.e., a dataset of male and female patients with similar average FFR and IMR, female patients still exhibited lower CFRs relative to male patients. This has been suggested to be due to female indexed resting cardiac output (i.e., relative to their body size) to be higher than that of men, whereas indexed stressed cardiac output to be equal, thus producing a lower relative CFR. Unfortunately, in this CT perfusion dataset, there are no female patients therefore this variable cannot be tested directly in our proposed model.

6.2.14. Diabetes

Regression coefficient for diabetes status (as opposed to no diabetes): -0.30(0.11)

Diabetes is perhaps the most significant comorbidity that affects CFR, this is not surprising as it is well documented directly that microvascular dilatory capability and CFR specifically lowered in diabetic patients versus nondiabetic patients[155–159]. This is due to increased

formation of plaques in both macrovascular and microvascular sections of the coronary circulatory system, caused by hyperglycaemia, sustained high levels of blood sugar causing damage to arterial linings[159–162].

6.2.15. Smoking

Regression coefficient for smokers (as opposed to non-smokers):
+0.265(0.11)

Smoking status is also known as one of the more influential factors that affect CFR. However contrary to what is expected as the effect of smoking on cardiovascular health, it appears as if smokers tend to have above average CFR in the patient population in our patient cohort, i.e., their coronary flow increased during hyperaemia better. This is counterintuitive as studies on CFR and smoking points to smoking causing damage to circulatory function[163].

This paradoxical observation is in line with, an observation that has been first reported over 25 years ago known as Smoker's paradox[164–166], among many cardiovascular disease experts when assessing smoking patient's cardiovascular health. In these studies, for a wide range of varying cardiovascular diseases, a consistent trend was found where smokers tended to show better cardiovascular indicators.

Whilst some other research has suggested, though non-conclusively, that smoking may modify plaque and clot composition that may in some diseases provide better outcomes (in terms of likelihood of cardiac events in the short term) [167], the consensus on smoker's paradox is that the paradox is the result of a sampling bias [168].

Many studies [166,168] noted that smoking individuals tended to show up as cardiac patients at far younger ages that meant they were much less likely to have comorbidities such as diabetes that are much more common among an older patient population. These comorbidities may contribute to poorer cardiac outcomes that far exceed the sole harm that smoking may cause in a younger patient.

However, in our findings, we isolated the variables of age, sex, and other health indicators such as diabetes status, yet a significant positive effect on CFR for patients that are smokers is still observed. There has not been much research directly on the effect of smoking on CFR over a patient population or direct biological studies on physical or biochemical mechanism behind the positive or negative impact of smoking on vascular dilation during hyperaemia. However, multiple studies have shown even mild smoking to be detrimental to microvascular health [169,170].

The potential explanation is that smokers present in clinics at less severe stages of coronary disease whilst exhibiting symptoms that more commonly occur at more severe stages. The route to being a cardiac patient generally starts with the exhibiting of symptoms such as chest pain (at rest or during exercise) or breathlessness, these symptoms whilst indicative of possible cardiac disease is also influenced by lung function where smoking is known to cause degradation. Therefore, the paradox here does not necessarily indicate that smoking improves CFR, but rather smokers with less severe levels of disease tend to show up more often in patient datasets due to their symptoms, therefore producing this paradoxical phenomenon.

Whilst this hypothesis has not been documented elsewhere, it coincides with previous studies on the Smoker's paradox that it ultimately is a result of a selection bias. However, because such bias seems to exist in our large patient dataset, the regression coefficient should still be included in our modelling, as it would make the predicting model of the CFR more representative for patients who are smokers.

6.2.16. Other metrics

It was suspected that hypertension, hyperlipidaemia and a family history of CAD may contribute to lowering CFR based on the literature[171], however it appears to not be the case in our patient dataset ($P > 0.05$ for all those factors as shown in **Table 6-1**).

6.2.17. Patient specific estimate for hyperaemic flow response formula

Based on the statistically significant contributing factors to CFR, namely sex, diabetes and smoking which are identified in Table 6-4, a multivariate regression model was derived. The formula for microvascular response to hyperaemia:

$$\text{Flow Increase} = 1.95 + 0.22Sx - 0.30Db + 0.28Sm \quad (22)$$

Here, Sx is the sex of the patient, 1 if male, 0 if female. Db is diabetes status, 1 if the patient has diabetes, 0 if the patient does not. Sm is the patient's smoker status, 1 if the patient is a smoker, 0 if the patient is not. Smoker status is self-reported. Note this flow increase is not strictly CFR as CFR takes into account any epicardial obstructions as well as microvascular vasodilation. However, for unobstructed arteries, this is effectively equal to CFR.

Taking into account uncertainties expressed with standard error, using uncertainty propagation:

$$\sigma_f^2 = \sum_i^n \sigma_i^2 \quad (23)$$

$$\sigma_{CFR}^2 = \sigma_{Average}^2 + \sigma_{Sx}^2 + \sigma_{Db}^2 + \sigma_{Sm}^2 \quad (24)$$

$$\sigma_{CFR}^2 = (0.25)^2 + (0.09)^2 + (0.11)^2 + (0.10)^2 \quad (25)$$

$$\sigma_{CFR} = 0.31 \quad (26)$$

Using the above equations and the patient cases, a patient specific CFR estimate can be produced.

Table 6-5 Patient specific predicted CFR based on patient metrics compared to measured CFR

Patient	Sex (1 = Male)	Diabetes Status (1 = Positive)	Smoker Status (1 = Positive)	Predicted CFR	Measured CFR (Global)
1	1	1	0	1.86±0.31	1.28
2	1	0	0	2.17±0.31	1.51
3	1	0	1	2.44±0.31	1.72
4	1	0	1	2.44±0.31	2.05
5	1	0	1	2.44±0.31	2.04
6	1	0	1	2.44±0.31	2.31
7	1	0	1	2.44±0.31	3.31
8	1	1	1	2.13±0.31	2.83
9	1	0	1	2.44±0.31	2.03
10	1	0	1	2.44±0.31	2.46

Table 6-6 The various CFR/hyperaemic flow response values used in FFRCT simulations.

Patient	Hyperaemic flow response (as a multiplier to resting flow)					
	Patient population average	General population average (assumption used in Conventional FFRCT)	Patient specific estimate	Patient specific (Measured) Global	Patient specific (Measured) Regional	Patient specific (Measured) Branch wise
1	2.14	3.50	1.86±0.31	1.28	0.97	0.82
2	""	""	2.17±0.31	1.83	1.64	1.25
3	""	""	2.44±0.31	2.32	1.91	1.71
4	""	""	2.44±0.31	2.61	2.27	2.01
5	""	""	2.44±0.31	2.49	2.15	1.23
6	""	""	2.44±0.31	2.31	2.28	2.10
7	""	""	2.44±0.31	3.31	3.19	3.13
8	""	""	2.13±0.31	2.83	2.72	2.31
9	""	""	2.44±0.31	2.03	2.06	1.95
10-1	""	""	2.44±0.31	2.46	1.81	1.07
10-2	""	""	1.86±0.31	2.46	2.12	1.29

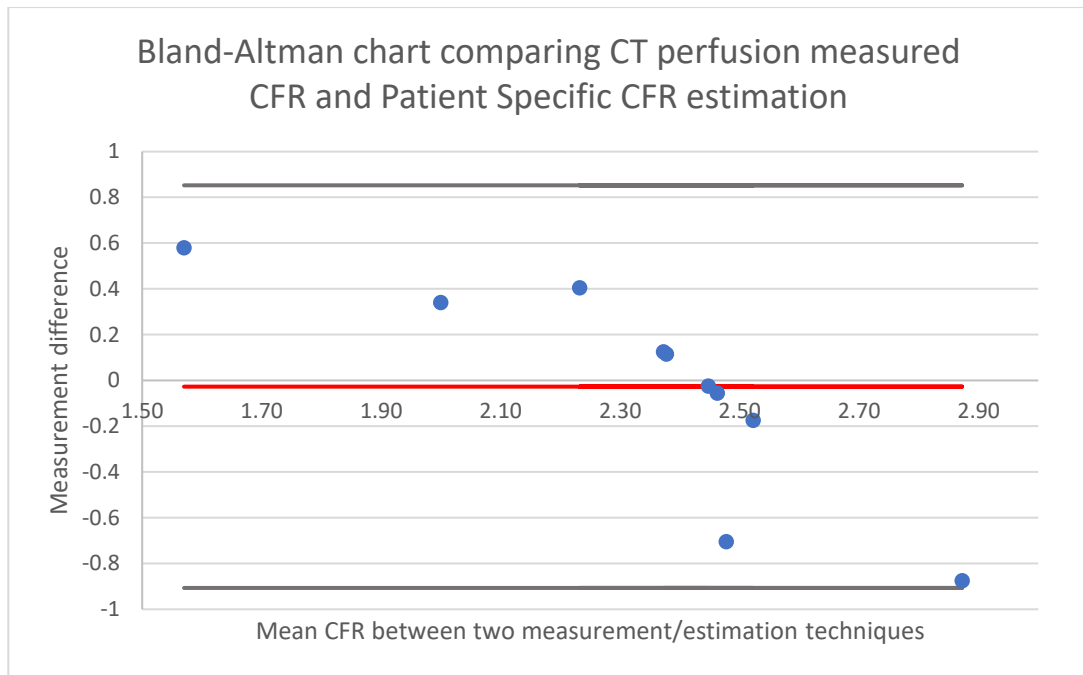


Figure 6-9 Bland Altman plot showing the performance of Patient specific CFR estimation versus CFR obtained from directly measured CT perfusion.

6.3. Results

There is a wide variety of patient disease levels present in this selection when looking at the invasive FFR values, see **Table 6-7**. For five out of the eleven vessels analysed, FFR was predicted between FFR = 0.75 and 0.85, close to the FFR = 0.8 cut-off,. Among those, FFR for Patients 4 and 6 was 0.77, which resides in the commonly denoted “Gray Zone” of FFR (FFR = 0.75 – 0.80). Patients in the gray zone usually require the physician to consider additional testing for further information. There are two patients in the more severe category, with FFR of 0.67 and 0.53 respectively, the latter would usually be diagnosed at the CTCA stage without requiring FFR to confirm a functionally significant stenosis. And Patient 10 in particular is an example of a patient with multivessel disease, with both LAD and LCX containing functionally significant stenoses that require intervention.

The CT perfusion imaging scanner also comes with its proprietary FFR mechanism (Siemens cFFR) that uses purely imaging data, without CFD, to estimate FFR values in a short amount of time in post processing.

Table 6-8 shows the relative sensitivity, specificity, and accuracy of the various simulated FFR regimes. Balanced Accuracy (BA or B-Acc) is included here as the patient dataset was skewed towards more positive cases than negative. In this context, a positive case is a FFR of <0.80 and a negative case is an FFR ≥ 0.80 . Note that in a clinical scenario, most cases between 0.75 and 0.80, the “gray zone” will not be blindly adhered to, but rather additional testing or consideration before committing to a treatment course.

Table 6-7 FFR values obtained by various hyperaemic flow response values applied to the downstream outlet boundary condition. The increase in flow is shown unless it is patient specific (they are shown in Table 6-6)

Patient	Invasive FFR	cFFR	FFRCT techniques (except iFR)										Measured Perfusion		
			Conventional	Patient Population Average			iFR	Patient specific Estimate			Branch-wise	Regional	Global		
				3.5x	2.68x	2.14x		1.6x	1.0x	low				mid	high
1(LCX)	0.84	0.64	0.75	0.79	0.83	0.87	0.92	0.88	0.85	0.83	0.93	0.92	0.90		
2(LAD)	0.73	0.81	0.64	0.70	0.76	0.81	0.89	0.79	0.76	0.72	0.86	0.82	0.79		
3(LAD)	0.72	0.85	0.67	0.73	0.78	0.83	0.90	0.78	0.75	0.72	0.82	0.80	0.76		
4(LAD)	0.77	0.77	0.72	0.76	0.81	0.85	0.91	0.81	0.78	0.76	0.82	0.80	0.77		
5(RCA)	0.67	0.77	0.57	0.64	0.71	0.77	0.86	0.71	0.67	0.63	0.83	0.71	0.66		
6(LAD)	0.77	0.49	0.69	0.74	0.79	0.84	0.90	0.79	0.76	0.73	0.78	0.78	0.77		
7(LCX)	0.88	0.53	0.84	0.86	0.89	0.91	0.95	0.89	0.87	0.86	0.84	0.84	0.83		
8(LAD)	0.83	0.66	0.81	0.84	0.87	0.90	0.94	0.89	0.87	0.85	0.92	0.83	0.83		
9(LAD)	0.82	0.7	0.70	0.75	0.80	0.84	0.91	0.80	0.77	0.74	0.81	0.81	0.81		
10(LAD)	0.53	0.51	0.43	0.53	0.62	0.70	0.82	0.62	0.57	0.51	0.81	0.68	0.56		
10(LCX)	0.72	0.79	0.67	0.73	0.78	0.83	0.90	0.78	0.75	0.72	0.87	0.78	0.75		

Positive Cases FFR ≤ 0.80 (iFR ≤ 0.90)

Negative Cases FFR > 0.80 (iFR > 0.90)

Table 6-8 Sensitivity, Specificity, Positive Predictive value, Negative Predictive value, Accuracy and Balanced Accuracy for various FFRCT methods compared to the Invasive FFR method. Note that this is referring to diagnostic accuracy.

FFR method	Hyperaemic flow condition	Sensitivity	Specificity	PPV	NPV	Acc	BACC
Invasive FFR	-	-	-	-	-	-	-
Siemens - cFFR	-	71%	0%	56%	0%	42%	28%
Conventional "estimate FFRCT	3.5x	100%	50%	78%	100%	82%	89%
Patient population upper bound (+1S.D) estimate FFRCT	2.68x	100%	50%	78%	100%	82%	89%
Patient population mean estimate FFRCT	2.14x	86%	100%	100%	80%	91%	90%
Patient population lower bound (-1S.D) estimate FFRCT	1.6x	29%	100%	100%	44%	55%	72%
Perfusion imaging based flow response	Patient specific measured	100%	100%	100%	100%	100%	100%

FFRCT - global							
Perfusion imaging based flow response FFRCT - regional	Patient specific measured	71%	100%	100%	67%	82%	83%
Perfusion imaging based flow response FFRCT – branch-wise	Patient specific measured	14%	100%	100%	40%	45%	70%
Patient specific flow response estimate FFRCT – lower bound (-1S.D)	Patient specific estimate	86%	100%	100%	80%	91%	90%
Patient specific flow response estimate FFRCT - mean	Patient specific estimate	100%	75%	88%	100%	91%	94%
Patient specific flow response estimate FFRCT (+1S.D)	Patient specific estimate	100%	75%	88%	100%	91%	94%

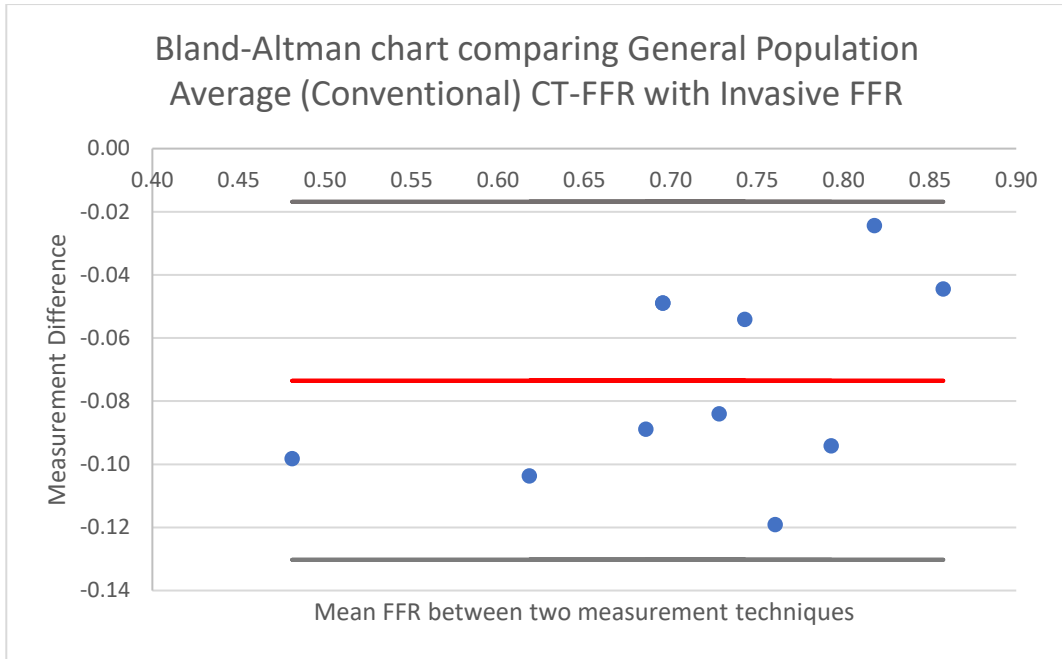


Figure 6-10 Bland-Altman plot comparing the conventional FFRCT method with Invasive FFR. Note the particularly strong negative bias of the conventional method, i.e., FFR values are lower in the conventional FFRCT than that measured invasively

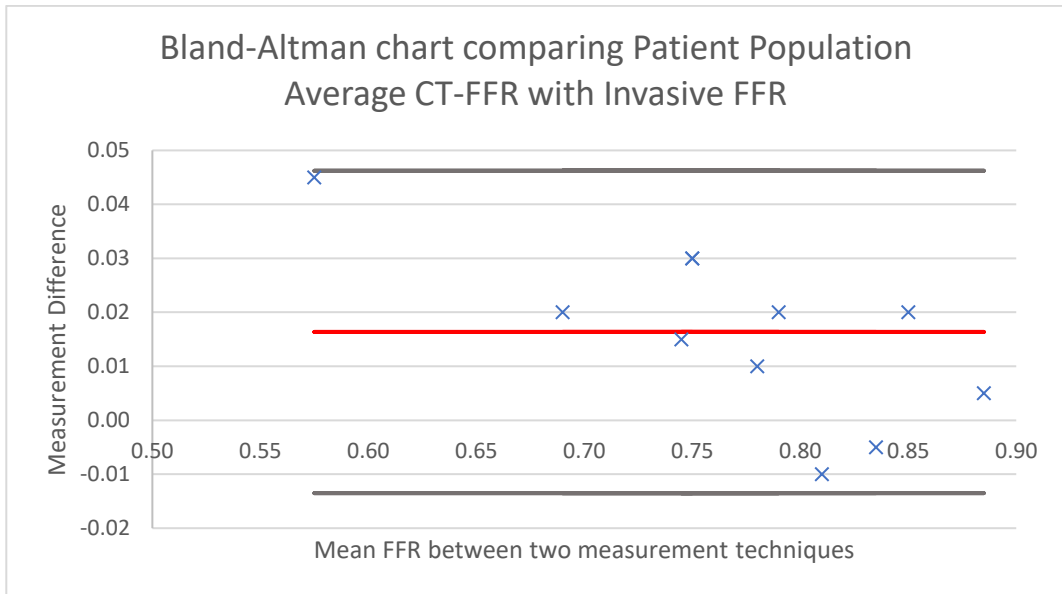


Figure 6-11 Bland-Altman chart comparing the patient population average assumption FFRCT with Invasive FFR. Note the slight positive bias of this method, i.e., this FFRCT method produces slightly higher FFR values on average.

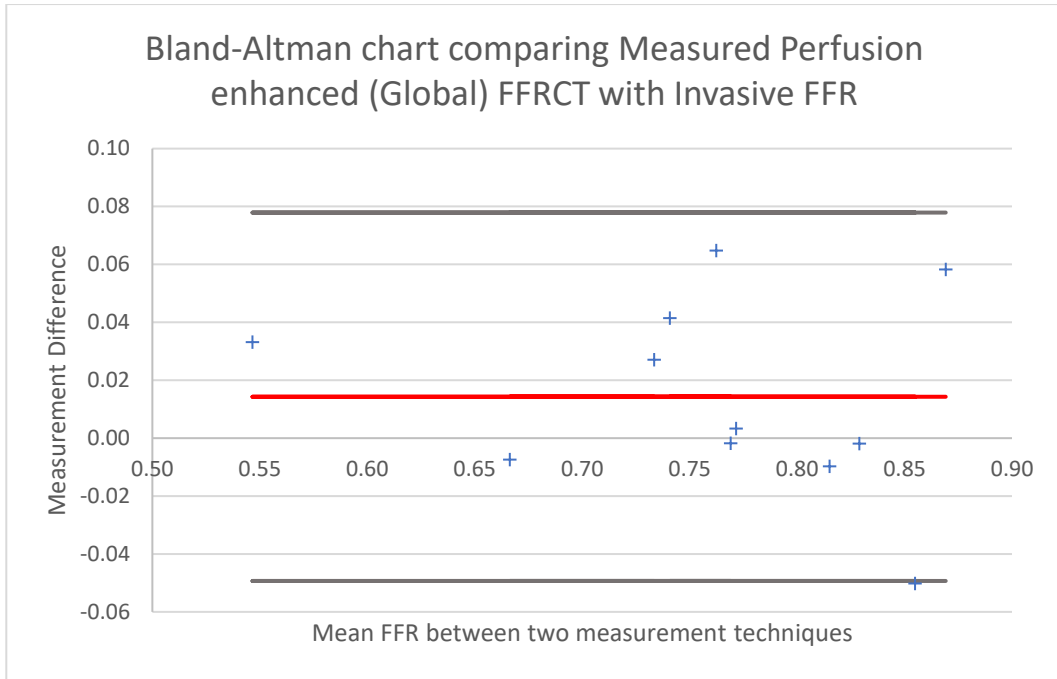


Figure 6-12 Bland-Altman chart comparing the FFRCT using a directly measured CFR value with Invasive FFR.

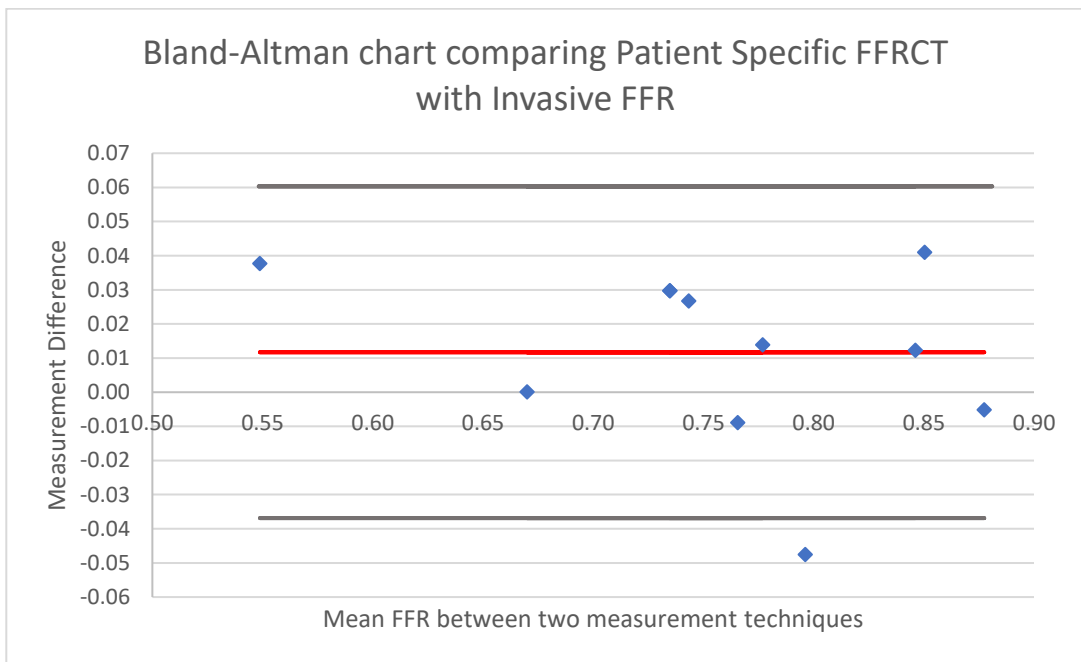


Figure 6-13 Bland-Altman chart comparing the FFRCT using an estimated CFR assumption based on patient specific metrics, with Invasive FFR.

Table 6-9 Mean error in FFR measurement of various methods relative to the invasive FFR measurement. *Note that Invasive FFR itself has a retest variability and has been included here for reference.

	Mean Error (FFR)
Invasive FFR (retest variability)	0.019*
Siemens CFFR	0.138
Conventional “general healthy population mean ” estimate FFRCT	0.073
Patient population lower bound (-1S.D) estimate FFRCT	0.079
Patient population mean estimate FFRCT	0.038
Patient population upper bound (+1S.D) estimate FFRCT	0.020
Perfusion imaging based flow response FFRCT - global	0.027
Perfusion imaging based flow response FFRCT - regional	0.054
Perfusion imaging based flow response FFRCT – target branch	0.113
Patient specific flow response estimate FFRCT – lower bound (-1S.D)	0.045
Patient specific flow response estimate FFRCT - mean	0.023
Patient specific flow response estimate FFRCT (+1S.D)	0.070

Table 6-10 The probability that a FFRCT result disagrees (misdiagnoses) with the diagnostic result of the Invasive FFR measurement based on the distribution of CFR values for each patient (or average over all patients).

Patient	Invasive FFR	Percentage probability of misdiagnosis (FFR cut-off = 0.80)	
		Patient population Average	Patient specific estimate
1	0.84	27%	14%
2	0.73	28%	26%
3	0.72	47%	21%
4	0.77	43%	38%
5	0.67	14%	6%
6	0.77	43%	25%
7	0.88	4%	0.9%
8	0.83	13%	3%
9	0.82	49%	31%
10	0.53	5%	1.6%
10	0.72	42%	21%

The CT perfusion imaging scanner also comes with its proprietary FFR mechanism (Siemens cFFR) that uses purely imaging data, without CFD, to estimate FFR values in a short amount of time in post processing.

Table 6-8 shows the relative sensitivity, specificity, and accuracy of the various simulated FFR regimes. Balanced Accuracy (BA or B-Acc) is included here as the patient dataset was skewed towards more positive cases than negative. Balanced Accuracy is the mean average of the True Positive Rate and the True Negative rate, it is often used in assessing binary classifiers when the proportion of positive and negative cases are skewed. In this context, a positive case is a FFR of <0.80 and a negative case is an FFR ≥ 0.80 . Note that in a clinical scenario, most cases between 0.75 and 0.80, the “gray zone” will not be blindly adhered to, but rather additional testing or consideration before committing to a treatment course.

Figures 6-9 to 6-13 show the Bland-Altman plots comparing various FFRCT regimes.

The Siemens cFFR had the lowest accuracy and its specificity was 0, misdiagnosing four negative cases as positive. This is perhaps not surprising as its mechanism relies purely on geometry, similarly to that of CTCA which also has a relatively high sensitivity and low specificity, where stenosed vessels are essentially over-diagnosed as having functionally significant disease, refer to **Table 2-1**. Note that cFFR is still in its research phase and it is intended as a fast (almost real time) non-invasive FFR solution. Conventional FFRCT, where the assumption is that the patient does not have any microvascular disease also faces this problem to an extent. Whilst FFRCT does use CFD to simulate blood flow through the stenosed vessel to calculate FFR and therefore assesses functional severity. By applying idealised and generalised assumptions on the microvascular flow response during hyperaemia (where flow increases by 3.5x), it inevitably produces the effect that the anatomy and vessel geometry becomes the sole determinant of FFR. This high sensitivity and moderate specificity are consistent in multiple studies including clinical trials [172,173].

Assessing the flow response based on the direct measurement from perfusion imaging **Table 6-7**, whilst the results do not match the invasive FFR values exactly, it managed to attain 100% diagnostic accuracy, i.e., the diagnostic result from a simulated FFR using directly measured flow responses matches the gold standard invasive FFR.

6.3.1. Response to hyperaemia population estimates

One of the crucial elements being tested in this chapter is the hyperaemic flow response, this is used to set the amount of reduction in coronary microvascular downstream resistance due to vasodilatory effects of hyperaemia.

In the ideal young and healthy patient, this increase in maximal flow is established to be between approximately 3.5-4.0, with a flow defect often being diagnosed when this value is less than 2.0 [174]. In this chapter, the

two available patient datasets – PET and CTP – both show that the patient population generally have a flow response lower than 3.5 (**Table 6-6**). With the large PET dataset (n=101) showing an average CFR of 1.89 (SD 0.48), measured using the software platform that was developed by the scanner manufacturer, Siemens Syngo.PET. In the separate and smaller CT perfusion dataset (n=10) used for simulations in this chapter, it was crucial to observe whether this lowered flow response is also observed.

The directly measured flow response for the 10 patients is shown in **Table 6-6**. On average, the measured CFR value average is 2.36 ± 0.52 , this is consistent with the PET dataset (n=101) with an average CFR of 1.89 ± 0.48 , which is also significantly lower than the healthy assumption of 3.5. Part of the discrepancy between the CTP dataset (n=10) and the PET dataset (n=101) is likely due to sex, the CTP dataset has only male patients. Note that these flow response values ignore the flow response of the suspected diseased vessel, therefore capture more accurately the overall microvascular dilatory response independent of an epicardial stenosis.

As microvascular disease tends to be systemic rather than localised , i.e., it is highly unlikely for a single branch of an artery to have significant microvascular defect and healthy microvascular vasodilatory function in other branches. This suggests that the measured flow response to hyperaemia of the region supplied by a suspected diseased branch, and comparison of that to other branches, could identify obstructions upstream. It should be reiterated here that CFR captures the totality of flow defects both in the main epicardial artery section and the microvasculature. For example, Patient 10 who has two diseased vessels, one moderate and one severe (in terms of FFR) has otherwise a relatively healthy flow response overall of 2.46. When looking at the regions directly supplied by the suspected diseased branches, the flow response in those regions of interest is significantly lower indicating that microvascular defects are unlikely the cause, but rather an obstruction in artery such as in patients 2,5, 10 in Table 6-6.

For the patients with a negative diagnosis, i.e., $FFR \geq 0.8$, therefore no significant obstruction in the arterial portion of the coronary tree, the flow response of the branches excluding the suspected diseased branch has a very similar value to the suspected diseased branch, such as in Patients 7, 8, 9 in Table 6-6. This suggests, in the case of mild or no obstruction, flow response to hyperaemia is primarily dictated by the microvascular response, and that response is approximately consistent across branches of the coronary tree.

Exploring this further, a regional flow response was measured, this counts the flow response of all branches of a particular artery, such as the LAD, but excludes the outlet(s) that are in the downstream of the suspected lesion. This is to identify the possibility that the flow response of a particular artery and its supplied region may be distinct from that of other arteries/supplied regions, however this does not appear to be the case. In general, these values are lower than the flow response of the system in general (excluding the suspected branch). The reason why this is lower most of the time is that for an artery with some level of obstruction, even mild, there is likely a lowered perfusion in the myocardium being measured.

Judging from both the absolute difference in FFR values and the difference in diagnostic result ($FFR \geq 0.8$ or $FFR < 0.8$) *Table 6-7*, it appears that the most reliable hyperaemic condition applied to the downstream resistance boundary condition is the measured flow response that takes into account all the branches (excluding the suspected diseased branch).

Lastly, using the flow response of the branch(es) downstream of the stenosis to set the boundary condition for those branch(es) produces poor results, specifically a very low sensitivity (14%) and low negative predictive value (40%). This is not surprising because the branches that are downstream of a suspected lesion are likely to have a lowered flow response shown in perfusion imaging, by setting that as the boundary condition which in essence is the microvascular response rather than overall flow response, it is essentially counting the flow limiting effects of a stenosis twice, i.e. the overall flow resistance of that branch segment: the

downstream boundary and the segment downstream of the stenosis, will be substantially higher than reality, driving a much lower flow to that branch. A lower flow, as shown previously, will produce a higher FFR value, therefore present a “healthy” or “healthier” diagnosis than the actual disease condition: a false negative.

6.3.2. Efficacy of demographically derived perfusion model of FFR prediction

The next step is to see whether it is possible to devise a method to estimate the downstream flow response to apply to the boundary conditions without the use of any perfusion imaging, as this is the most realistic clinical use case. Conventional FFRCT[108,148] which uses only CTCA images to produce its simulation assumes the case that the patient has ideal microvascular health and therefore microvascular flow will increase by 3.5 times. The caveat is that patients with microvascular defects are likely to be misdiagnosed when they have a significant obstructive stenosis, which was mentioned in their paper [108,148]. As evident in the direct comparison with the measured flow response of the patients in our dataset, the conventional assumption is a significant overestimation with only the CFR for Patient 7 coming close at 3.31.

Consistent with clinical studies[172,173] of conventional FFRCT schemes, our analyses using the conventional scheme show a high sensitivity and negative predictive value, i.e. positive cases are almost always detected, but low specificity and positive predictive value, 2 out of 4 “healthy” cases are misdiagnosed as severe or requiring treatment (**Table 6-7**). In this small sample, the 3.5x flow response boundary condition achieved 100% sensitivity and 50% specificity, an overall accuracy of 82, consistent with the studies on the diagnostic accuracy of these techniques[172,173].

In this investigation, a more moderate value was observed to better represent the patient population as opposed to the general healthy population. Here, a “training” dataset of 101 patients with possible CAD was used to derive the average flow response to hyperaemia: 2.14 ± 0.54 ,

directly from PET perfusion imaging., which then became the basis of our demography-based estimate model of CFR that was applied to the “test” data set of 10 patients who underwent CTP (CT Myocardial perfusion imaging). The PET-based CFR value is much closer to the average of vasodilatory response in the dataset used for FFRCT (measured directly from CTP), with 7 out of the 10 patients within one standard deviation of this estimate. Once applied to estimate FFR, this model shows a much higher specificity, achieving 100% in this case, but a slightly lowered sensitivity of 86%. But overall this is an increased diagnostic accuracy of 91% [172][173].

It needs to be said that whilst a higher accuracy is desirable, in specific diagnostic settings depending on disease and treatment that follows a diagnosis, it may be more desirable to have a higher sensitivity even if specificity (and overall accuracy) suffers or vice versa. An extreme example of this would be a disease that has a near certainty of death if untreated, while the treatment itself has relatively minor side/negative effects. In this example it would be crucial to identify every possible Positive case even if negative cases get misidentified as positive.

For the positive case that this method missed: Patient 4 with an invasive measurement of 0.77, it would be considered a borderline case well within what is considered the “gray zone” (0.75-0.80) where it would often be supplemented with additional testing or further consideration of other health metrics. The conventional method in this case shows FFR=0.72, a more confident positive result, which could push the clinical diagnosis towards a higher level of certainty.

6.3.3. Effect of uncertainty in flow response estimate based on demographic parameters

Since the patient-specific prediction of CFR has its uncertainty the impact of this was further investigated by incorporating upper and lower bounds based on 1 standard deviation in flow response above and below the mean, therefore the flow response to hyperaemia would be 1.57 and 2.65.

The lower bound boundary conditions produced poor sensitivity of 29% and a high specificity of 100%, overall, a low accuracy of 55% and would be completely undesirable in a clinical setting as a significant number of positive cases are being missed. This is expected, physically speaking, as limiting flow downstream will inevitably increase FFR (i.e., indicate less severe obstruction), a flow response of 1.57 as an average across all branches is also well below the CFR threshold of 2.0, which would suggest a likelihood of severe microvascular disease that would likely be detected during consultation and preliminary testing.

The upper bound flow response of 2.65x on the other hand performed identically in diagnostic performance with the conventional 3.5x hyperaemic flow assumption, capturing the same positive and negative cases. Often in FFRCT protocols, clinicians are advised to defer results in the gray zone to invasive testing, therefore when the cases between 0.75 and 0.85 (measured via the FFRCT protocol) are excluded from consideration [143]. The 2.65x boundary condition achieves a 100% diagnostic accuracy and the conventional 3.5x condition achieves a 90% diagnostic accuracy, consistent with their findings of 91%[122]. However, in the 2.65x case, it so happens those 3 cases are in the gray zone and excluded, whereas the 3.5x case had only 1 case excluded, therefore it is not a completely fair comparison.

It appears that the optimal value exists somewhere between 2.11 and 2.65 and using the analysis of patient metrics and their influence on hyperaemic flow response, it is clear why this is the case despite 2.14 being the average overall. The CT perfusion dataset of 10 patients is exclusively male, and it has been shown that sex has a statistically significant positive effect on the flow response **Table 6-4**, an increase of 0.24 ± 0.10 , bringing the value well within those bounds: 2.38, which is very close to the perfusion imaging measured average of 2.36. However, with this new flow response, Patient 9 which is already a borderline case would have an FFRCT < 0.80, creating a false positive case, whilst Patient 4 who was a previously false negative case is correctly categorised as a positive case. Overall, the patient-specific predictive model of flow response could produce a better

performing FFRCT protocol, with 100% sensitivity and 75% specificity which in this case has an identical diagnostic accuracy of 91% but higher balanced accuracy of 94% versus 90% using the 2.14x assumption.

Considering that previously correctly diagnosed cases are now misdiagnosed, it is apparent that one model does not fit all. Since the patient dataset in this circumstance is disproportionately male (100% male) versus the PET “training” dataset where the statistical patient population model was obtained (64% male), other metrics that play a role should be taken into account on a patient-specific basis. For practicality, these parameters need to be readily available in routine clinical practice and the metrics fall into this category are smoker status and diabetes. Applying the patient specific estimation formula (Equation 24), a patient-specific flow estimate can be obtained without any additional testing or perfusion imaging.

Using the patient specific estimates, the diagnostic performance is identical to that of the 2.38 estimate (2.14+0.24) that took into account the patient dataset was 100% male. When looking at the deviation from the measured flow response, the patient specific estimate taking into account diabetes and smoking slightly outperformed the 2.38 case, standard deviation of 0.45 vs 0.50, indicating the applicability of these additional metrics. Whilst the discrepancy is not significant, and in this limited dataset the diagnostic accuracy is identical, the extreme cases of CFR such as Patient 1, 2 and 7, are much closer to the patient specific estimates. Lastly as smoker’s paradox, where smokers tend to show better outcomes is a controversial finding with many suggested explanations, when smoker status is excluded from the equation, the standard deviation rises to 0.48, suggesting that the positive trend (CFR is correlated positively with smoking) is indeed applicable and consistent between the two datasets.

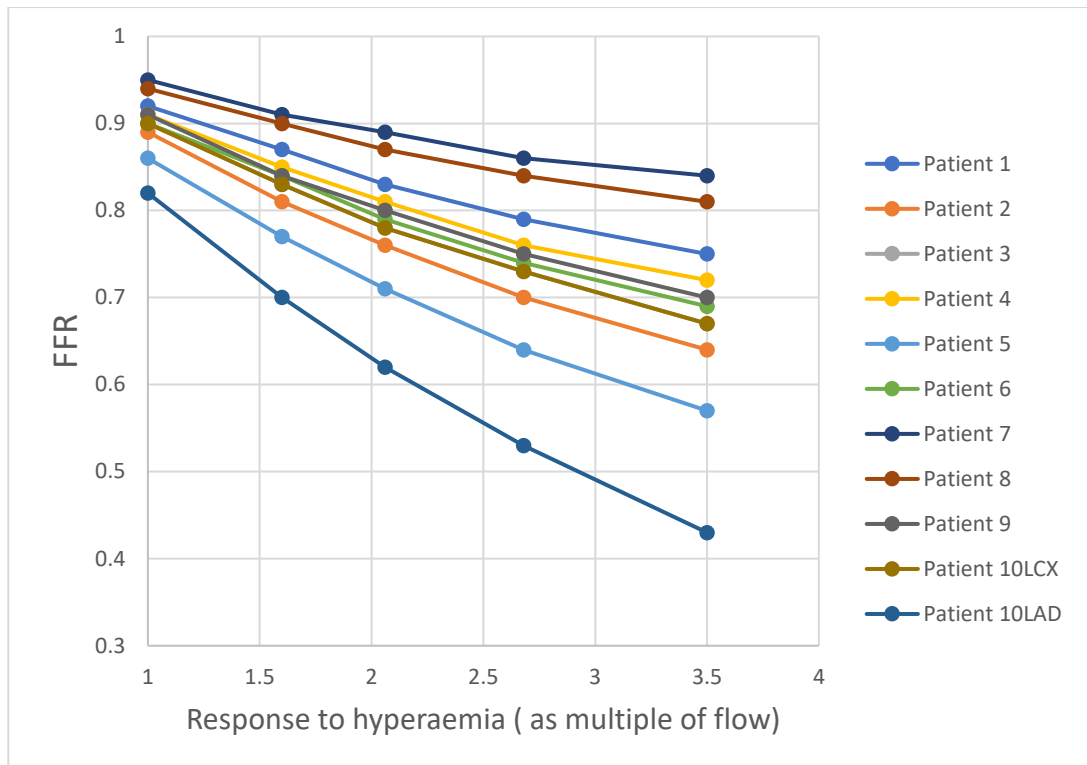


Figure 6-14 Relationship between FFR and Hyperaemic Response

6.3.4. Quantitative accuracy of the FFRCT calculation

As expected, FFRCT with the CT-perfusion-based flow response produced the most accurate FFR values overall, but there is still some degree of error. The mean error is 0.023, which is slightly higher than the Test-retest variability of invasive FFR testing of 0.019[175,176] but the difference was not significant enough to produce incorrect diagnostic results. In terms of the diagnostic categorisation (based on the threshold value of FFR=0.8), this method is as good as the invasive method however it is worth reiterating that perfusion imaging complimenting FFRCT simulation is not a clinically viable option. Generally speaking, perfusion imaging, whilst being costlier and often comes with a higher radiation dose, as well as potential side effects of the drugs and contrast agents, produces far more information for the clinician to make decisions on than FFRCT. If perfusion imaging is available and recommended, FFRCT is unlikely to be used in addition unless in the case of multi-vessel disease where the culprit vessel cannot be identified in the perfusion imaging. The utility here of testing the FFRCT computation, with various flow response models, against

invasive FFR gives confidence to how close the simulation is to predict the in vivo FFR, which should in theory be based on the ability of the model in replicating the conditions of the patient's coronary system, and in particular the quality of the anatomical model, the assumptions on cardiac output, blood pressure and downstream resistance, when the response to hyperaemia is known.

6.3.5. CT-based computational prediction of iFR (CT-iFR)

In Chapter 4, it was shown that steady flow simulations without hyperaemic flow adjustment tend to approximate iFR (instantaneous flow reserve) well. With a cut-off of <0.90 being a positive case, iFR measured in this dataset achieved an 86% sensitivity and 75% specificity, and an overall accuracy of 82% when compared to the diagnostic categorisation based on the invasive FFR measurements.

It should be noted that confidence in invasive iFR measurement is not as established as FFR, with simulation based iFR even less so. With cases between 0.86 and 0.93, the advice given to clinicians is to perform invasive FFR testing to verify the result[177]. But in cases lower than 0.86 and higher than 0.93, they are considered as reliable as FFR[178]. In our dataset a 100% diagnostic accuracy is achieved when excluding cases in this range, however that only leaves 3 cases outside IFR of 0.86 and 0.93.

6.3.6. Development of probabilistic model

As a spread for the flow response to hyperaemia can be determined, it would be possible to determine the uncertainty in the FFR prediction and the relationship between the potential breadth of predicted FFR and diagnostic categories per patient. For a case where the invasive FFR is below 0.80, what is the probability that the FFRCT scheme in question will produce an FFR value of above 0.80. This value can provide clinicians with a guide to the certainty of a FFRCT result and determine with more information whether additional testing is required before making treatment decisions.

In **Table 6-7**, it is apparent that for the cases where the distance from the cut-off (FFR = 0.8) is large, the probability that the FFRCT scheme would misdiagnose the patient is lower as the spread of FFRCT values becomes less likely to overlap with the cut-off.

It should be made clear that here a low percentage is not a measure of a high performing methodology of calculating FFRCT, but rather simply shows how close to the FFR cut-off the simulated result is and how likely it would produce the wrong diagnosis given the uncertainty in the flow response parameter. It should also be apparent that there is a strong correlation between the distance of the invasive FFR value from the cut-off with the percentage probability that the FFRCT method produces the wrong diagnostic result.

In the clinic, most cases between 0.75 and 0.80 (FFR gray zone), even for invasive FFR testing, would almost always necessitate further testing and considerations.

It is important to note that whilst invasive FFR is the gold standard measure for the functional significance of a coronary artery stenosis, it has its own reproducibility error of ~3-4% [51,72,176].

6.3.7. Relationship between hyperaemia and FFR.

In chapter 3, the electrical analog model was devised as a means to conceptualise the problem (see Figure 3-1). Equation 7 showed that in the electrical analog, the “FFR” is only dependent on the resistance of the epicardial artery and the microvasculature, and the microvascular vasodilatory response to hyperaemia.

Using the FFRCT results, Figure 6-14, obtained via varying responses to hyperaemia, it is apparent that the relationship between hyperaemic response and FFR matches closely with the electrical analog, see Figure 3-2. This has a couple ramifications; it suggests that perhaps FFR simulations for the most part can be further simplified. In previous chapters it was shown that flow pulsatility, whilst important for blood flow

simulations, doesn't seem to affect FFR values as much. In chapter 5, it was shown, consistent with the electrical analog assumptions, that in multi-vessel disease cases, neighbouring vessels do not affect each other's FFR's either. This provides a lot more validity to some of the novel FFRCT simulations that focus on per-vessel simulation and the faster more simplified 1D flow simulations [179].

Whilst estimating the resistance of a stenosis is a non-trivial problem, the relationship between FFR and the stenosis resistance, microvascular resistance and hyperaemic response may suggest that once an FFRCT simulation has been performed, it may be possible to estimate what the FFRCT value would be if the response to hyperaemia is varied for different patient demographics, as well as producing a similar probabilistic spread of values without the requirement of additional simulation runs that require further computational time. This is however purely theoretical and will require further investigation and validation to be clinically viable.

6.4. Concluding remarks

The CT Perfusion patient dataset with the invasively measured FFR was used to validate the findings of Chapter 5, showing that perfusion imaging data can augment FFR-CT boundary conditions to provide greater diagnostic performance. Clinically, perfusion imaging and FFR/FFRCT analysis are not commonly used in conjunction due to cost. Therefore, it was important in this chapter to devise a new approach to FFR-CT simulations that could improve upon some of the assumptions made in the conventional approaches without requiring additional imaging data or medical testing beyond the routine CTCA.

Using the 101 patient PET perfusion dataset to quantify the relationship of hyperaemic flow response (a key factor in setting boundary conditions) and patient metrics, a regression model was derived to produce an estimate of hyperaemic flow response without actual perfusion imaging. Using this estimate, a comprehensive analysis of the diagnostic performance of FFR-CT was completed and validated against invasive FFR

that is the gold standard. The novel hyperaemic response model based on patient metrics has strong association with smoking, diabetes and sex. When the model is used as part of FFR-CT prediction, a better diagnostic accuracy (94%) than the current conventional approaches (82%) was demonstrated.

In addition, as both the average response and its variability to hyperaemia is known in the patient population, it was possible to determine a spread of values of FFRCT, creating upper and lower bounds of confidence that a clinician can gain greater diagnostic information.

With further study and trials among a greater and more diverse patient sample, it has the potential to offer an improvement on existing FFRCT methods.

6.5. Limitations

6.5.1. Anatomical model reconstruction

In this chapter FFRCT was compared with the gold standard invasive FFR to assess how close the two values may be. One crucial limitation that may be difficult to assess is the impact of image segmentation and anatomical model reconstruction on the predicted FFRCT values. As FFRCT is determined by the flow across an obstruction and the anatomy of the coronary tree, image segmentation that accurately produces a realistic anatomical model plays a major role in determining the FFRCT value. Further investigation into the variability of FFR based solely on image segmentation can be performed by using multiple manual segmentation operators or in comparison to well established automated schemes, which there are currently only a few commercially available or open-source options. Sankaran et al [135] shown that manual segmentation of the minimum lumen diameter, i.e. the smallest cross section across the stenosis produces approximately 6-8% variability in FFRCT, approximately twice that of invasive FFR's reproducibility.

6.5.2. CFR measurement for CT perfusion dataset

In the PET perfusion dataset with 100+ patients, CFRs were measured using clinically tested software (Siemens Syngo.via). CT perfusion on the other hand, only raw perfusion data (regional myocardial blood flow) in the rest and stress state were available directly from the clinical software platform. CFR for the CT perfusion dataset was calculated manually by identifying appropriate ROI based on where coronary branches are, and the perfusion values of the stress and rest images were compared.

6.5.3. Patient metrics

For the purpose of setting patient specific microvascular response to hyperaemia, many of the metrics identified as having a statistically significant effect are binary label, such as diabetes and smoker status. It does not further describe for example how severe the diabetes is, how long the patient has had it for, etc. And for smoking, it does not take into account how long the patient has been smoking and the quantity or frequency of smoking. The model of the outlet boundary conditions based on these binary metrics may cause the flow response estimate to overshoot the “true value” such as in a situation where a patient is a mild diabetic or a very recent or infrequent smoker.

Ideally these metrics will be quantified in a more precise manner, which will not only allow further fine tuning of FFRCT simulations but identify the specific relationship between these variables and microvascular function and therefore accurately characterise the response to hyperaemia.

6.5.4. Implementation of new scheme

The proposed novel FFRCT scheme is mostly similar to the current clinical pathway where it is used to determine treatment for cases of coronary artery disease of uncertain functional significance. Whilst non-invasive functional testing is always preferred when available, such as PET, SPECT, perfusion MRI, and more recently CT perfusion, perfusion-based imaging is often in short supply and costly both in monetary and skilled

manpower terms. With the exception of MRI perfusion, the other imaging techniques also incur a radiation dose on the patient. In the current clinical pathway, especially in the USA and UK, CTCA is recommended as the first line of investigation for coronary artery disease and in most patient cases CTCA can identify severe lesions certainly requiring treatment with good accuracy [180], leaving only a proportion of moderate cases that require additional assessment. When CT-based FFR computation is applied for this subset of patients, since FFR is primarily a binary diagnostic tool, it is prone to a diagnostic accuracy problem for patients around the threshold, where even a slight error in calculation can produce a vastly different diagnostic result and therefore treatment decision. By implementing this new scheme of producing a likely range of FFR with a statistical percentage to show the likelihood of each diagnostic result, the clinicians could be better informed in assessing the diagnostic result in a more holistic manner.

Chapter 7. Conclusions

This chapter summarises and concludes the major findings of the thesis and addresses the questions posed at the start of this project in Chapter 1. The overarching aim of this project is to find ways to improve non-invasive diagnoses of coronary artery disease, especially the methodology surrounding FFRCT methods.

The fundamentals of FFRCT methods are laid out in Chapters 2 and 3. In those chapters, the current state-of-the-art conventional FFRCT such as HeartFlow technology which has FDA approval and approved for use in many nations worldwide, is described. Variants of simulation-based FFR such as iFR, dFFR have also been compared, with some examples of their application using real patient data shown in Chapters 4, 5 and 6.

As FFRCT is primarily a simulation-based method, many assumptions are inevitably needed to define parameters used in the computational method, in particular, boundary conditions for blood pressure, coronary inflow and flow pulsatility that crucially determine the flow characteristics. In this study, some of these parameters are shown to have a significant effect on the value of FFR which affects the diagnostic result even in the range of those parameters which is widely accepted.

Chapter 4 posed the question, how far the FFRCT simulation scheme can be simplified without significant variation in the FFR measurement. Specifically, it looked at inflow conditions, patient parameters such as heart rate, stroke volume (of the left ventricle), cardiac output and blood pressure were assessed as well as the comparison of pulsatile flow versus steady flow simulation. Cardiac output was found to play a significant role, as increased cardiac output led to increased coronary flow which ultimately lowers FFR in a stenosed artery. The pressure drop across a stenosis is shown to be directly proportional to the flow which in turn is almost proportional to the cardiac output, with variation based on how other branches redistribute flow when there exists one or multiple stenosed branches.

Chapter 5 examined the assumption of using an idealised response to hyperaemia, which has been identified as one of the limitations of current FFRCT methods, where a healthy population average response is assumed applicable to the patient population. As the response to hyperaemia is overestimated in the healthy response assumption, the FFRCT measurement is often lower than reality, i.e., more severe than it really is. The lower negative predictive value (NPV) of FFRCT relative to its positive predictive value (PPV), and relative to the NPV of other diagnostic methods is well observed in the literature, including by its proponents. Using myocardial perfusion imaging (MPI) data from PET and CTP, the results from Chapters 5 and 6 suggest that the response to hyperaemia assumption is an area to improve on due to the variability of this parameter and how it directly impacts the FFR.

Chapter 6 looked at the feasibility and efficacy to use patient specific metrics (e.g., sex, diabetes, smoking status) to estimate the response to hyperaemia in a more systematic way. This allows to incorporate patient-specific perfusion information in FFRCT computation without the need for perfusion imaging data. Using a large dataset of 101 patients with CFR measured clinically, a statistical relationship was derived between these metrics and the vasodilatory response of the microvasculature in hyperaemia. Applying this relationship to the FFRCT simulation produced FFRCT values that are closer to the invasively measured FFR values (the gold standard for validating any FFR techniques) in comparison to the conventional assumptions. The patient-specific estimate on hyperaemia helped to identify whether the flow defect is solely caused by an epicardial stenosis or a combination with a decreased microvascular vasodilatory response. The diagnostic performance of the novel model produced an accuracy of 91% versus the conventional model with an accuracy of 82%.

Furthermore, as the variability of CFR is known, the novel model can produce a spread of FFRCT values, potentially a way to inform a clinician of the probability that an FFRCT value is the correct diagnostic result, adding utility to the clinical workflow for CAD. Although this will require further validation in larger patient dataset, the work presented in this thesis

demonstrated the potential of a novel FFRCT method that incorporate patient-specific myocardial microvascular response without need of perfusion imaging.

7.1. Limitations

A limitation of this study is the relatively low number of patients (n=10) included in our validation where simulation based FFR is compared against invasive measurements. In order to avoid over-examination of patients, high quality patient data with both perfusion imaging and invasive FFR from clinical setting is not commonly available. The two diagnostic methods typically are not used in conjunction other than explicitly for comparison studies. Were this data available, a more representative relationship between the downstream perfusion, the boundary conditions and the resulting FFRCT measurement could have been derived and more thoroughly validated. That being said, the novel method of using patient parameters to inform the boundary conditions was tested and produced representative FFR values without the need for further perfusion imaging.

Another key limitation of this study is that the comparisons with conventional FFRCT techniques used commercially in the clinic is based on a reproduction of their methodology laid out in published literature rather than directly comparing their FFRCT protocol in a holistic manner, i.e., using a commercially available FFRCT service. There are possibilities of methodological discrepancies between what is defined as “conventional technique” in this thesis and what are used in the commercial service, for example anatomical model reconstruction method and quality, as well as precise parameter settings that may not be explicitly described in the literature. A good comparison study of any FFRCT variants or novel FFRCT methods with the conventional FFRCT protocols should consist of a large cohort of patients that have both invasive FFR and commercially available (and FDA/NICE approved) FFRCT measurements taken.

7.2. Future work and recommendations

The novel methodology proposed in this study and specifically in Chapter 6, shows that using patient specific parameters like sex, diabetes, and smoking status in the consideration of the response to hyperaemia can possibly improve conventional FFRCT which holds assumptions that does not take those variables into account. The relationship between these patient parameters and the response to hyperaemia was quantified using a moderately sized patient cohort (n=101) which had a diverse range of myocardial disease classifications based on clinically measured response to hyperaemia, which can be associated with demographic parameters of each patient. Further investigation should look at quantifying specifically how much each parameter individually contributes to the response to hyperaemia and explain these relationships at a biological and functional level.

Furthermore, the current study only looked at patient parameters that are commonly recorded, it is possible there are other parameters out there that could be included and can draw a significant relationship to the response to hyperaemia. For example, some clinicians use surveys that query a patient's ability to perform certain physical tasks, which produces a score that essentially provides an estimate to that patient's microvascular health. Considerations will be needed here to balance between the additional merit versus practicality of data collection.

Another unique aspect of the proposed methodology is to show a probabilistic spread of the likely diagnostic result, rather than relying on a purely binary result of disease or healthy. There is the "grey zone" currently defined for $0.75 < \text{FFR} < 0.80$ but it only suggests that other tests may be required and does not adequately inform the clinician in either direction the likely outcome for the patient is. There are multiple possible avenues to test the utility of the probabilistic FFR spread feature: 1) whether the most probable diagnostic outcome is the correct outcome, 2) at what degree of certainty does the method achieve a certain level of accuracy, 3) what decisions will a clinician make given a probabilistic diagnostic value versus

a strict binary diagnostic value, this may include decisions such as further tests, opting for medical therapy/intervention counter to the recommendation etc. These studies can be performed retrospectively with existing patient datasets, the only requirement is that they have invasive FFR measured, high quality CTCA images available for FFRCT and the patient metrics used currently.

Lastly as FFRCT gains wider acceptance and novel FFRCT methods are being tested, further research can look into the design of testing schemes, where depending on the severity of the patient's coronary disease, certain diagnostic tests can be skipped, or further diagnostic testing is required, or a hybrid approach using different tests when needed, such as FFRCT + MPI, that have complimentary information. This will help create a workflow that optimises cost, time, and accuracy of diagnosis. The probabilistic spread of values in this novel FFRCT method can also aid in the decision making for further tests.

References

- [1] Lo E, Menezes L, Torii R. Impact of Inflow Boundary Conditions on the Calculation of CT-Based FFR. *Fluids* 2019;4:60. doi:10.3390/fluids4020060.
- [2] Lo EW, Menezes LJ, Torii R. On outflow boundary conditions for CT-based computation of FFR: Examination using PET images. *Med Eng Phys* 2020;76:79–87. doi:10.1016/j.medengphy.2019.10.007.
- [3] Papamanolis L, Kim HJ, Jaquet C, Sinclair M, Schaap M, Danad I, et al. Myocardial Perfusion Simulation for Coronary Artery Disease: A Coupled Patient-Specific Multiscale Model. *Ann Biomed Eng* 2021;49:1432–47. doi:10.1007/s10439-020-02681-z.
- [4] Townsend N, Williams J, Bhatnagar P, Wickramasinghe K, Rayner M. *Cardiovascular disease statistics, 2014*. 2014.
- [5] Ambrose JA, Singh M. Pathophysiology of coronary artery disease leading to acute coronary syndromes. *F1000Prime Rep* 2015;7:08. doi:10.12703/P7-08.
- [6] Shah T, Geleris JD, Zhong M, Swaminathan R V., Kim LK, Feldman DN. Fractional flow reserve to guide surgical coronary revascularization. *J Thorac Dis* 2017;9:S317–26. doi:10.21037/jtd.2017.03.55.
- [7] Fractional Flow Reserve (FFR). Fractional Flow Reserve (FFR) is used... | by Apollo Gleneagles | Medium n.d. <https://medium.com/@aghlcorpcomm/fractional-flow-reserve-ffr-1b31a29dc6bc> (accessed April 20, 2021).
- [8] Coronary arteries anatomy n.d. <http://www.edoctoronline.com/medical-atlas.asp?c=4&id=22165> (accessed March 22, 2021).
- [9] Rafieian-Kopaei M, Setorki M, Douidi M, Baradaran A, Nasri H. Atherosclerosis: Process, indicators, risk factors and new hopes. *Int J*

Prev Med 2014;5:927–46.

- [10] Libby P, Buring JE, Badimon L, Hansson GK, Deanfield J, Bittencourt MS, et al. Atherosclerosis. *Nat Rev Dis Prim* 2019;5:1–18. doi:10.1038/s41572-019-0106-z.
- [11] Moss AJ, Williams MC, Newby DE, Nicol ED. The Updated NICE Guidelines: Cardiac CT as the First-Line Test for Coronary Artery Disease. *Curr Cardiovasc Imaging Rep* 2017;10. doi:10.1007/s12410-017-9412-6.
- [12] Alrifai A, Kabach M, Nieves J, Pino J, Chait R. Microvascular Coronary Artery Disease: Review Article. *US Cardiol Rev* 2017;1. doi:10.15420/usc.2017:27:1.
- [13] Berwick ZC, Payne GA, Lynch B, Dick GM, Sturek M, Tune JD. Contribution of Adenosine A2A and A2B Receptors to Ischemic Coronary Dilation: Role of KV and KATP Channels. *Microcirculation* 2010;17:600–7. doi:10.1111/j.1549-8719.2010.00054.x.
- [14] Goodwill AG, Dick GM, Kiel AM, Tune JD. Regulation of coronary blood flow. *Compr Physiol* 2017;7:321–82. doi:10.1002/cphy.c160016.
- [15] Asher A, Ghelani R, Thornton G, Rathod K, Jones D, Wragg A, et al. UK perspective on the changing landscape of non-invasive cardiac testing. *Open Hear* 2019;6:e001186. doi:10.1136/openhrt-2019-001186.
- [16] Montalescot G, Sechtem U, Achenbach S, Andreotti F, Arden C, Budaj A, et al. 2013 ESC guidelines on the management of stable coronary artery disease - addenda. *Eur Heart J* 2013;34:2949–3003. doi:10.1093/eurheartj/eh296.
- [17] Hachamovitch R, Hayes SW, Friedman JD, Cohen I, Berman DS. Comparison of the short-term survival benefit associated with revascularization compared with medical therapy in patients with no prior coronary artery disease undergoing stress myocardial perfusion single photon emission computed tomography. *Circulation*

2003;107:2900–6. doi:10.1161/01.CIR.0000072790.23090.41.

- [18] Kočka V. The coronary angiography - An old-timer in great shape. *Cor Vasa* 2015;57:e419–24. doi:10.1016/j.crvasa.2015.09.007.
- [19] Hulten EA, Carbonaro S, Petrillo SP, Mitchell JD, Villines TC. Prognostic value of cardiac computed tomography angiography: A systematic review and meta-analysis. *J Am Coll Cardiol* 2011;57:1237–47. doi:10.1016/j.jacc.2010.10.011.
- [20] Meijboom WB, Van Mieghem CAG, van Pelt N, Weustink A, Pugliese F, Mollet NR, et al. Comprehensive Assessment of Coronary Artery Stenoses. Computed Tomography Coronary Angiography Versus Conventional Coronary Angiography and Correlation With Fractional Flow Reserve in Patients With Stable Angina. *J Am Coll Cardiol* 2008;52:636–43. doi:10.1016/j.jacc.2008.05.024.
- [21] Adamson PD, Hunter A, Williams MC, Shah ASV, McAllister DA, Pawade TA, et al. Diagnostic and prognostic benefits of computed tomography coronary angiography using the 2016 National Institute for Health and Care Excellence guidance within a randomised trial. *Heart* 2018;104:207–14. doi:10.1136/heartjnl-2017-311508.
- [22] van den Boogert TPW, Vendrik J, Claessen BEPM, Baan J, Beijik MA, Limpens J, et al. CTCA for detection of significant coronary artery disease in routine TAVI work-up. *Netherlands Hear J* 2018;26:591–9. doi:10.1007/s12471-018-1149-6.
- [23] Hlatky MA, De Bruyne B, Pontone G, Patel MR, Norgaard BL, Byrne RA, et al. Quality-of-Life and Economic Outcomes of Assessing Fractional Flow Reserve with Computed Tomography Angiography: PLATFORM. *J Am Coll Cardiol* 2015;66:2315–23. doi:10.1016/j.jacc.2015.09.051.
- [24] Bamberg F, Sommer WH, Hoffmann V, Achenbach S, Nikolaou K, Conen D, et al. Meta-analysis and systematic review of the long-term predictive value of assessment of coronary atherosclerosis by contrast-enhanced coronary computed tomography angiography. *J*

- Am Coll Cardiol 2011;57:2426–36. doi:10.1016/j.jacc.2010.12.043.
- [25] Otton JM, Yu CY, McCrohon J, Sammel N, Feneley M. Accuracy and clinical outcomes of computed tomography coronary angiography in the presence of a high coronary calcium score. *Hear Lung Circ* 2013;22:980–6. doi:10.1016/j.hlc.2013.05.647.
- [26] Arbab-Zadeh A, Miller JM, Rochitte CE, Dewey M, Niinuma H, Gottlieb I, et al. Diagnostic accuracy of computed tomography coronary angiography according to pre-test probability of coronary artery disease and severity of coronary arterial calcification: The CORE-64 (Coronary Artery Evaluation Using 64-Row Multidetector Computed Tomography Angiography) international multicenter study. *J Am Coll Cardiol* 2012;59:379–87. doi:10.1016/j.jacc.2011.06.079.
- [27] Budoff MJ, Min JK. FFR Derived from Coronary CT Angiography Solving the Calcification Dilemma of Coronary CT Angiography. *JACC Cardiovasc Imaging* 2015;8:1056–8. doi:10.1016/j.jcmg.2015.06.004.
- [28] Choi JH, Min JK, Labounty TM, Lin FY, Mendoza DD, Shin DH, et al. Intracoronary transluminal attenuation gradient in coronary CT angiography for determining coronary artery stenosis. *JACC Cardiovasc Imaging* 2011;4:1149–57. doi:10.1016/j.jcmg.2011.09.006.
- [29] Achenbach S, Narula J. Coronary CT angiography: From sensitivity to specificity. *JACC Cardiovasc Imaging* 2011;4:1227–9. doi:10.1016/j.jcmg.2011.10.001.
- [30] Chow BJW, Kass M, Gagn O, Chen L, Yam Y, Dick A, et al. Can differences in corrected coronary opacification measured with computed tomography predict resting coronary artery flow? *J Am Coll Cardiol* 2011;57:1280–8. doi:10.1016/j.jacc.2010.09.072.
- [31] Choi J-H, Koo B-K, Yoon YE, Min JK, Song Y-B, Hahn J-Y, et al. Diagnostic performance of intracoronary gradient-based methods by coronary computed tomography angiography for the evaluation of physiologically significant coronary artery stenoses: a validation study

with fractional flow reserve. *Eur Heart J Cardiovasc Imaging* 2012;13:1001–7. doi:10.1093/ehjci/jes130.

- [32] De Feyter PJ. CT functional imaging using intracoronary gradient analysis: An indispensable boost for CT coronary angiography. *Eur Heart J Cardiovasc Imaging* 2012;13:971–2. doi:10.1093/ehjci/jes164.
- [33] Manda YR, Baradhi KM. *Cardiac Catheterization, Risks and Complications*. StatPearls Publishing; 2019.
- [34] Tesche C, De Cecco CN, Albrecht MH, Duguay TM, Bayer RR, Litwin SE, et al. Coronary CT Angiography–derived Fractional Flow Reserve. *Radiology* 2017;285:17–33. doi:10.1148/radiol.2017162641.
- [35] Hopkins Medicine. Angioplasty and Stent Placement for the Heart 2001:68–70. <https://www.hopkinsmedicine.org/health/treatment-tests-and-therapies/angioplasty-and-stent-placement-for-the-heart>.
- [36] Meijboom WB, Meijs MFL, Schuijf JD, Cramer MJ, Mollet NR, van Mieghem CAG, et al. Diagnostic Accuracy of 64-Slice Computed Tomography Coronary Angiography. A Prospective, Multicenter, Multivendor Study. *J Am Coll Cardiol* 2008;52:2135–44. doi:10.1016/j.jacc.2008.08.058.
- [37] Fearon WF, Achenbach S, Engstrom T, Assali A, Shlofmitz R, Jeremias A, et al. Accuracy of Fractional Flow Reserve Derived from Coronary Angiography. *Circulation* 2019;139:477–84. doi:10.1161/CIRCULATIONAHA.118.037350.
- [38] Kajander S, Joutsiniemi E, Saraste M, Pietilä M, Ukkonen H, Saraste A, et al. Cardiac positron emission tomography/computed tomography imaging accurately detects anatomically and functionally significant coronary artery disease. *Circulation* 2010;122:603–13. doi:10.1161/CIRCULATIONAHA.109.915009.
- [39] Koo BK, Erglis A, Doh JH, Daniels D V., Jegere S, Kim HS, et al. Diagnosis of ischemia-causing coronary stenoses by noninvasive fractional flow reserve computed from coronary computed

tomographic angiograms: Results from the prospective multicenter DISCOVER-FLOW (Diagnosis of Ischemia-Causing Stenoses Obtained Via Noni. *J Am Coll Cardiol* 2011;58:1989–97. doi:10.1016/j.jacc.2011.06.066.

- [40] Förster S, Rieber J, Übleis C, Weiss M, Bartenstein P, Cumming P, et al. Tc-99m sestamibi single photon emission computed tomography for guiding percutaneous coronary intervention in patients with multivessel disease: A comparison with quantitative coronary angiography and fractional flow reserve. *Int J Cardiovasc Imaging* 2010;26:203–13. doi:10.1007/s10554-009-9510-x.
- [41] Kirschbaum SW, Springeling T, Rossi A, Duckers E, Gutiérrez-Chico JL, Regar E, et al. Comparison of adenosine magnetic resonance perfusion imaging with invasive coronary flow reserve and fractional flow reserve in patients with suspected coronary artery disease. *Int J Cardiol* 2011;147:184–6. doi:10.1016/j.ijcard.2010.12.038.
- [42] Ko BS, Cameron JD, Meredith IT, Leung M, Antonis PR, Nasis A, et al. Computed tomography stress myocardial perfusion imaging in patients considered for revascularization: a comparison with fractional flow reserve. *Eur Heart J* 2012;33:67–77. doi:10.1093/eurheartj/ehr268.
- [43] Min JK, Leipsic J, Pencina MJ, Berman DS, Koo BK, Van Mieghem C, et al. Diagnostic accuracy of fractional flow reserve from anatomic CT angiography. *JAMA - J Am Med Assoc* 2012;308:1237–45. doi:10.1001/2012.jama.11274.
- [44] Taylor CA, Fonte TA, Min JK. Computational fluid dynamics applied to cardiac computed tomography for noninvasive quantification of fractional flow reserve: Scientific basis. *J Am Coll Cardiol* 2013;61:2233–41. doi:10.1016/j.jacc.2012.11.083.
- [45] Pijls NHJ, de Bruyne B, Peels K, van der Voort PH, Bonnier HJRM, Bartunek J, et al. Measurement of Fractional Flow Reserve to Assess the Functional Severity of Coronary-Artery Stenoses. *N Engl J Med*

1996;334:1703–8. doi:10.1056/NEJM199606273342604.

- [46] Erglis A, Jegere S, Runkule Z, Zvaigzne L, Sondore D, Kumsars I, et al. Non-invasive FFR Using Coronary CT Angiography 2013.
- [47] Tonino PAL, Fearon WF, De Bruyne B, Oldroyd KG, Leeser MA, Ver Lee PN, et al. Angiographic Versus Functional Severity of Coronary Artery Stenoses in the FAME Study. Fractional Flow Reserve Versus Angiography in Multivessel Evaluation. *J Am Coll Cardiol* 2010;55:2816–21. doi:10.1016/j.jacc.2009.11.096.
- [48] Van Nunen LX, Zimmermann FM, Tonino PAL, Barbato E, Baumbach A, Engstrøm T, et al. Fractional flow reserve versus angiography for guidance of PCI in patients with multivessel coronary artery disease (FAME): 5-year follow-up of a randomised controlled trial. *Lancet* 2015;386. doi:10.1016/S0140-6736(15)00057-4.
- [49] De Bruyne B, Pijls NHJ, Kalesan B, Barbato E, Tonino P a L, Piroth Z, et al. Fractional flow reserve-guided PCI versus medical therapy in stable coronary disease. *N Engl J Med* 2012;367:991–1001. doi:10.1056/NEJMoa1205361.
- [50] FFR in 2017: Current Status in PCI Management - American College of Cardiology n.d. <https://www.acc.org/latest-in-cardiology/articles/2017/05/25/08/34/ffr-in-2017-current-status-in-pci-management> (accessed April 20, 2021).
- [51] Corcoran D, Hennigan B, Berry C. Fractional flow reserve: a clinical perspective. *Int J Cardiovasc Imaging* 2017;33:961–74. doi:10.1007/s10554-017-1159-2.
- [52] McNabney CG, Sellers SL, Wilson RJA, Hart S, Rosenblatt SA, Murphy DT, et al. Prognosis of CT-derived Fractional Flow Reserve in the Prediction of Clinical Outcomes. *Radiol Cardiothorac Imaging* 2019;1:e190021. doi:10.1148/ryct.2019190021.
- [53] Fearon WF. FFR , IMR , CFR Discordance : Should We Abandon CFR ? n.d.

- [54] Fearon WF, Kobayashi Y. Invasive Assessment of the Coronary Microcirculation *. *JACC Cardiovasc Interv* 2016;9:802–4. doi:10.1016/j.jcin.2016.01.028.
- [55] Sen S, Escaned J, Malik IS, Mikhail GW, Foale RA, Mila R, et al. Development and validation of a new adenosine-independent index of stenosis severity from coronary waveintensity analysis: Results of the ADVISE (ADenosine Vasodilator Independent Stenosis Evaluation) study. *J Am Coll Cardiol* 2012;59:1392–402. doi:10.1016/j.jacc.2011.11.003.
- [56] Sen S, Ahmad Y, Dehbi HM, Howard JP, Iglesias JF, Al-Lamee R, et al. Clinical Events After Deferral of LAD Revascularization Following Physiological Coronary Assessment. *J Am Coll Cardiol* 2019;73. doi:10.1016/j.jacc.2018.10.070.
- [57] Leone AM, Porto I, De Caterina AR, Basile E, Aurelio A, Gardi A, et al. Maximal hyperemia in the assessment of fractional flow reserve: Intracoronary adenosine versus intracoronary sodium nitroprusside versus intravenous adenosine: The NASCI (nitroprussiato versus adenosina nelle stenosi coronariche intermedie) study. *JACC Cardiovasc Interv* 2012;5:402–8. doi:10.1016/j.jcin.2011.12.014.
- [58] De Bruyne B, Sarma J. Fractional flow reserve: a review. *Heart* 2008;94:949–59. doi:10.1136/hrt.2007.122838.
- [59] Oldroyd K, Mbc HB, Berry C, Mbc HB. *Adenosine* 2014;7. doi:10.1016/j.jcin.2014.02.009.
- [60] Wilson RF, Wyche K, Christensen B V, Zimmer S, Laxson DD. Clinical Investigation Effects of Adenosine on Human Coronary Arterial Circulation. *Circulation* 1990;82:1595–606. doi:10.1161/01.CIR.82.5.1595.
- [61] Padilla J, Harris RA, Fly AD, Rink LD, Wallace JP. A comparison between active- and reactive-hyperaemia-induced brachial artery vasodilation. *Clin Sci* 2006;110:387–92. doi:10.1042/CS20050328.

- [62] Nakazato R, Gransar H, Berman DS, Cheng VY, Lin FY, Achenbach S, et al. Statins use and coronary artery plaque composition: Results from the International Multicenter CONFIRM Registry. *Atherosclerosis* 2012;225:148–53. doi:10.1016/j.atherosclerosis.2012.08.002.
- [63] Garcia D, Harbaoui B, van de Hoef TP, Meuwissen M, Nijjer SS, Echavarría-Pinto M, et al. Relationship between FFR, CFR and coronary microvascular resistance - Practical implications for FFR-guided percutaneous coronary intervention. *PLoS One* 2019;14:e0208612. doi:10.1371/journal.pone.0208612.
- [64] Johnson NP, Gould KL. How Do PET Myocardial Blood Flow Reserve and FFR Differ? *Curr Cardiol Rep* 2020;22. doi:10.1007/s11886-020-1274-x.
- [65] Singh V, Di Carli MF. SPECT Versus PET Myocardial Perfusion Imaging in Patients with Equivocal CT. *Curr Cardiol Rep* 2020;22:1–10. doi:10.1007/s11886-020-01287-0.
- [66] Driessen RS, Raijmakers PG, Stuijzand WJ, Knaapen P. Myocardial perfusion imaging with PET. *Int J Cardiovasc Imaging* 2017;33:1021–31. doi:10.1007/s10554-017-1084-4.
- [67] Bateman TM. Advantages and disadvantages of PET and SPECT in a busy clinical practice. *J Nucl Cardiol* 2012;19:3–11. doi:10.1007/s12350-011-9490-9.
- [68] Kanthabalan A, Shah T, Arya M, Punwani S, Bomanji J, Haroon A, et al. The FORECAST study - Focal recurrent assessment and salvage treatment for radiorecurrent prostate cancer. *Contemp Clin Trials* 2015;44:175–86. doi:10.1016/j.cct.2015.07.004.
- [69] Thompson AG, Raju R, Blanke P, Yang T hyun, Mancini GBJ, Budoff MJ, et al. Diagnostic accuracy and discrimination of ischemia by fractional flow reserve CT using a clinical use rule: Results from the Determination of Fractional Flow Reserve by Anatomic Computed Tomographic Angiography study. *J Cardiovasc Comput Tomogr* 2015;9:120–8. doi:10.1016/j.jcct.2015.01.008.

- [70] Gaur S, Achenbach S, Leipsic J, Mauri L, Bezerra HG, Jensen JM, et al. Rationale and design of the HeartFlowNXT (HeartFlow analysis of coronary blood flow using CT angiography: NeXt sSteps) study. *J Cardiovasc Comput Tomogr* 2013;7:279–88. doi:10.1016/j.jcct.2013.09.003.
- [71] Morris PD, van de Vosse FN, Lawford P V., Hose DR, Gunn JP. “Virtual” (Computed) Fractional Flow Reserve. *JACC Cardiovasc Interv* 2015;8:1009–17. doi:10.1016/j.jcin.2015.04.006.
- [72] Gaur S, Achenbach S, Leipsic J, Mauri L, Bezerra HG, Jensen JM, et al. Rationale and design of the HeartFlowNXT (HeartFlow analysis of coronary blood flow using CT angiography: NeXt sSteps) study. *J Cardiovasc Comput Tomogr* 2013;7:279–88. doi:10.1016/j.jcct.2013.09.003.
- [73] Min JK, Koo BK, Erglis A, Doh JH, Daniels D V., Jegere S, et al. Effect of image quality on diagnostic accuracy of noninvasive fractional flow reserve: Results from the prospective multicenter international DISCOVER-FLOW study. *J Cardiovasc Comput Tomogr* 2012;6:191–9. doi:10.1016/j.jcct.2012.04.010.
- [74] Chilian WM, Dellsperger KC, Layne SM, Eastham CL, Armstrong MA, Marcus ML, et al. Effects of atherosclerosis on the coronary microcirculation. *Am J Physiol* 1990;258:H529–39.
- [75] Bruyne B De, Hersbach F, Pijls NHJ, Bartunek J, Bech J, Heyndrickx GR. Abnormal Epicardial Coronary Resistance in Patients With Diffuse Atherosclerosis but “ Normal ” Coronary Angiography 2001.
- [76] Oh KW, Lee K, Ahn B, Furlani EP. Design of pressure-driven microfluidic networks using electric circuit analogy. *Lab Chip* 2012;12:515–45. doi:10.1039/c2lc20799k.
- [77] Kinlay S, Grewal J, Manuelin D, Fang JC, Selwyn AP, Bittl JA, et al. Coronary flow velocity and disturbed flow predict adverse clinical outcome after coronary angioplasty. *Arterioscler Thromb Vasc Biol* 2002;22:1334–40. doi:10.1161/01.ATV.0000024569.80106.B4.

- [78] Peiro J, Sherwin S. Finite Difference, Finite Element and Finite Volume Methods for Partial Differential Equations. *Handb Mater Model* 2005;M:2415–46. doi:10.1007/978-1-4020-3286-8_127.
- [79] ANSYS CFX-Solver Theory Guide 2009;15317:724–46.
- [80] Vignon-clementel IE, Figueroa CA, Jansen KE, Taylor CA. Outflow boundary conditions for three-dimensional finite element modeling of blood flow and pressure in arteries 2006;195:3776–96. doi:10.1016/j.cma.2005.04.014.
- [81] Murray CD. The Physiological Principle of Minimum Work : I. The vascular system and the cost of blood volume. *Proc Natl Acad Sci U S A* 1926;12:207–14. doi:10.1085/jgp.9.6.835.
- [82] Murray C. The physiological principle of minimum work: II. Oxygen exchange in capillaries. ... *Natl Acad Sci United ...* 1926;18:439–55. doi:10.1073/pnas.12.3.207.
- [83] Olufsen MS, Peskin CS, Kim WY, Pedersen EM, Nadim A, Larsen J. Numerical simulation and experimental validation of blood flow in arteries with structured-tree outflow conditions. *Ann Biomed Eng* 2000;28:1281–99. doi:10.1114/1.1326031.
- [84] Iberall AS. Anatomy and steady flow characteristics of the arterial system with an introduction to its pulsatile characteristics. *Math Biosci* 1967;1:375–95. doi:10.1016/0025-5564(67)90009-0.
- [85] Suwa N, Niwa T, Fukasawa H, Sasaki Y. Estimation of Intravascular Blood Pressure Gradient by Mathematical Analysis of Arterial Casts. *Tohoku J Exp Med* 1963;79:168–98. doi:10.1620/tjem.79.168.
- [86] Sagawa K, Lie RK, Schaefer J. Translation of Otto frank’s paper “Die Grundform des arteriellen Pulses” *zeitschrift für biologie* 37: 483-526 (1899). *J Mol Cell Cardiol* 1990;22:253–4. doi:10.1016/0022-2828(90)91459-K.
- [87] Westerhof N, Lankhaar JW, Westerhof BE. The arterial windkessel. *Med Biol Eng Comput* 2009;47:131–41. doi:10.1007/s11517-008-

0359-2.

- [88] Mantero S, Pietrabissa R, Fumero R, Bioingegneria D. The coronary bed and its role in the cardiovascular system : a review and an introductory single-branch model 1992;14:109–16.
- [89] Francis SE. Continuous Estimation of Cardiac Output and Arterial Resistance from Arterial Blood Pressure using a Third-Order Windkessel Model. Massachusetts Institute of Technology, 2007.
- [90] Liu B, Dalin T. Influence of non-Newtonian properties of blood on the wall shear stress in human atherosclerotic right coronary arteries. *MCB Mol Cell Biomech* 2011;8:73–90. doi:10.3970/mcb.2011.008.073.
- [91] Abbasian M, Shams M, Valizadeh Z, Moshfegh A, Javadzadegan A, Cheng S. Effects of different non-Newtonian models on unsteady blood flow hemodynamics in patient-specific arterial models with in-vivo validation. *Comput Methods Programs Biomed* 2020;186:105185. doi:10.1016/j.cmpb.2019.105185.
- [92] Pollanen MS. Dimensional optimization at different levels of the arterial hierarchy. *J Theor Biol* 1992;159:267–70. doi:10.1016/S0022-5193(05)80706-4.
- [93] Olufsen MS. Structured tree outflow condition for blood flow in larger systemic arteries. *Am J Physiol Circ Physiol* 1999;276:H257–68. doi:10.1152/ajpheart.1999.276.1.H257.
- [94] N??rgaard BL, Leipsic J, Gaur S, Seneviratne S, Ko BS, Ito H, et al. Diagnostic performance of noninvasive fractional flow reserve derived from coronary computed tomography angiography in suspected coronary artery disease: The NXT trial (Analysis of Coronary Blood Flow Using CT Angiography: Next Steps). *J Am Coll Cardiol* 2014;63:1145–55. doi:10.1016/j.jacc.2013.11.043.
- [95] FDA Approves HeartFlow FFR-CT: Non-Invasive Method for Determining Coronary Ischemia n.d.

http://www.ptca.org/news/2014/1126_HEARTFLOW.html (accessed March 20, 2021).

- [96] HeartFlow FFRCT for estimating fractional flow reserve from coronary CT angiography | Guidance and guidelines | NICE n.d.
- [97] Boileau E, Pant S, Roobottom C, Sazonov I, Deng J, Xie X, et al. Estimating the accuracy of a reduced-order model for the calculation of fractional flow reserve (FFR). *Int j Numer Method Biomed Eng* 2018;34:e2908. doi:10.1002/cnm.2908.
- [98] Kim HJ, Vignon-Clementel IE, Coogan JS, Figueroa CA, Jansen KE, Taylor CA. Patient-specific modeling of blood flow and pressure in human coronary arteries. *Ann Biomed Eng* 2010;38:3195–209. doi:10.1007/s10439-010-0083-6.
- [99] Siogkas PK, Papafaklis MI, Sakellarios AI, Stefanou KA, Bourantas C V, Athanasiou LS, et al. Patient-Specific Simulation of Coronary Artery Pressure Measurements : An In Vivo Three-Dimensional Validation Study in Humans 2015;2015.
- [100] Morris PD, Silva Soto DA, Feher JFA, Rafiroiu D, Lungu A, Varma S, et al. Fast Virtual Fractional Flow Reserve Based Upon Steady-State Computational Fluid Dynamics Analysis: Results From the VIRTU-Fast Study. *JACC Basic to Transl Sci* 2017;2:434–46. doi:10.1016/j.jacbts.2017.04.003.
- [101] Achenbach S, Rudolph T, Rieber J, Eggebrecht H, Richardt G, Schmitz T, et al. Coronary Performing and Interpreting Fractional Flow Reserve Measurements in Clinical Practice : An Expert Consensus Document 2017:97–109. doi:10.15420/icr.2017.
- [102] Abe M, Tomiyama H, Yoshida H, Doba N. Diastolic fractional flow reserve to assess the functional severity of moderate coronary artery stenoses: Comparison with fractional flow reserve and coronary flow velocity reserve. *Circulation* 2000;102:2365–70. doi:10.1161/01.CIR.102.19.2365.

- [103] Chalyan DA, Zhang Z, Takarada S, Molloy S. End-diastolic fractional flow reserve comparison with conventional full-cardiac cycle fractional flow reserve. *Circ Cardiovasc Interv* 2014;7:28–34. doi:10.1161/CIRCINTERVENTIONS.113.000327.
- [104] Miyashita H. Clinical Assessment of Central Blood Pressure. *Curr Hypertens Rev* 2012;8:80–90. doi:10.2174/157340212800840708.
- [105] Williams B, Lacy PS, Thom SM, Cruickshank K, Stanton A, Collier D, et al. Differential impact of blood pressure-lowering drugs on central aortic pressure and clinical outcomes: Principal results of the Conduit Artery Function Evaluation (CAFE) study. *Circulation* 2006;113:1213–25. doi:10.1161/CIRCULATIONAHA.105.595496.
- [106] HAMLIN RL, LEVESQUE MJ, KITTLESON MD. Intramyocardial pressure and distribution of coronary blood flow during systole and diastole in the horse. *Cardiovasc Res* 1982;16:256–62. doi:10.1093/cvr/16.5.256.
- [107] Ramanathan T, Skinner H. Coronary blood flow. *Contin Educ Anaesthesia, Crit Care Pain* 2005;5:61–4. doi:10.1093/bjaceaccp/mki012.
- [108] Taylor CA, Fonte TA, Min JK. Computational Fluid Dynamics Applied to Cardiac Computed Tomography for Noninvasive Quantification of Fractional Flow Reserve: Scientific Basis. *J Am Coll Cardiol* 2013;61:2233–41. doi:10.1016/J.JACC.2012.11.083.
- [109] Uus A. Patient-Specific Blood Flow Modelling in Diagnosis of Coronary Artery Disease. (Unpublished Dr Thesis, City Univ London) 2016.
- [110] Zhang J-M, Zhong L, Luo T, Lomarda AM, Huo Y, Yap J, et al. Simplified Models of Non-Invasive Fractional Flow Reserve Based on CT Images. *PLoS One* 2016;11:e0153070. doi:10.1371/journal.pone.0153070.
- [111] Reyes E, Loong CY, Harbinson M, Donovan J, Ms C, Ath DIPRCP, et

al. High-Dose Adenosine Overcomes the Attenuation of Myocardial Perfusion Reserve Caused by Caffeine. *JAC* 2008;52:2008–16. doi:10.1016/j.jacc.2008.08.052.

- [112] Morgan JM, McCormack DG, Griffiths MJ, Morgan CJ, Barnes PJ, Evans TW. Adenosine as a vasodilator in primary pulmonary hypertension. *Circulation* 1991;84:1145–9. doi:10.1161/01.CIR.84.3.1145.
- [113] Reyes E, Loong CY, Harbinson M, Donovan J, Anagnostopoulos C, Underwood SR. High-Dose Adenosine Overcomes the Attenuation of Myocardial Perfusion Reserve Caused by Caffeine. *J Am Coll Cardiol* 2008;52:2008–16. doi:10.1016/j.jacc.2008.08.052.
- [114] Zhou B, Bentham J, Di Cesare M, Bixby H, Danaei G, Cowan MJ, et al. Worldwide trends in blood pressure from 1975 to 2015: a pooled analysis of 1479 population-based measurement studies with 19.1 million participants. *Lancet* 2017;389:37–55. doi:10.1016/S0140-6736(16)31919-5.
- [115] Wright JD, Hughes JP, Ostchega Y, Ph D. Mean Systolic and Diastolic Blood Pressure in Adults Aged 18 and Over in the United States , 2001 – 2008 2011:2001–8.
- [116] Bovendeerd PHM, Borsje P, Arts T, Van De Vosse FN. Dependence of intramyocardial pressure and coronary flow on ventricular loading and contractility: A model study. *Ann Biomed Eng* 2006;34:1833–45. doi:10.1007/s10439-006-9189-2.
- [117] Sun Y, Gewirtz H. Estimation of intramyocardial pressure and coronary blood flow distribution. *Am J Physiol - Hear Circ Physiol* 1988;255. doi:10.1152/ajpheart.1988.255.3.h664.
- [118] SALISBURY PF, CROSS CE, RIEBEN PA. Intramyocardial pressure and strength of left ventricular contraction. *Circ Res* 1962;10:608–23. doi:10.1161/01.RES.10.4.608.
- [119] Solecki M, Kruk M, Demkow M, Schoepf UJ, Reynolds MA, Wardziak

- Ł, et al. What is the optimal anatomic location for coronary artery pressure measurement at CT-derived FFR? *J Cardiovasc Comput Tomogr* 2017;11:397–403. doi:10.1016/j.jcct.2017.08.004.
- [120] HeartFlow FFRCT Analysis - Non-Invasive Cardiac Test | HeartFlow n.d. <https://www.heartflow.com/heartflow-ffrct-analysis/> (accessed April 25, 2021).
- [121] Achenbach S, Rudolph T, Rieber J, Eggebrecht H, Richardt G, Schmitz T, et al. Performing and interpreting fractional flow reserve measurements in clinical practice: An expert consensus document. *Interv Cardiol Rev* 2017;12:97–109. doi:10.15420/icr.2017:13:2.
- [122] Götberg M, Christiansen EH, Gudmundsdottir IJ, Sandhall L, Danielewicz M, Jakobsen L, et al. Instantaneous Wave-free Ratio versus Fractional Flow Reserve to Guide PCI. *N Engl J Med* 2017;376:1813–23. doi:10.1056/NEJMoa1616540.
- [123] Sen S, Petraco R, Mayet J, Davies J. Wave intensity analysis in the human coronary circulation in health and disease. *Curr Cardiol Rev* 2014;10:17–23. doi:10.2174/1573403X10999140226121300.
- [124] Heyndrickx GR, Tóth GG. The FAME trials: Impact on clinical decision making. *Interv Cardiol Rev* 2016;11:116–9. doi:10.15420/icr.2016:14:3.
- [125] Byrd BF, Wahr D, Wang YS, Bouchard A, Schiller NB. Left ventricular mass and volume/mass ratio determined by two-dimensional echocardiography in normal adults. *J Am Coll Cardiol* 1985;6:1021–5. doi:10.1016/S0735-1097(85)80304-1.
- [126] Taylor CA, Gaur S, Leipsic J, Achenbach S, Berman DS, Jensen JM, et al. Effect of the ratio of coronary arterial lumen volume to left ventricle myocardial mass derived from coronary CT angiography on fractional flow reserve. *J Cardiovasc Comput Tomogr* 2017;11:429–36. doi:10.1016/j.jcct.2017.08.001.
- [127] Tu S, Westra J, Yang J, von Birgelen C, Ferrara A, Pellicano M, et al.

Diagnostic Accuracy of Fast Computational Approaches to Derive Fractional Flow Reserve From Diagnostic Coronary Angiography: The International Multicenter FAVOR Pilot Study. *JACC Cardiovasc Interv* 2016;9:2024–35. doi:10.1016/j.jcin.2016.07.013.

- [128] Cattermole GN, Leung PYM, Ho GYL, Lau PWS, Chan CPY, Chan SSW, et al. The normal ranges of cardiovascular parameters measured using the ultrasonic cardiac output monitor. *Physiol Rep* 2017;5. doi:10.14814/phy2.13195.
- [129] JEGIER W, SEKELJ P, AULD PA, SIMPSON R, MCGREGOR M. the Relation Between Cardiac Output and Body Size. *Br Heart J* 1963;25:425–30. doi:10.1136/hrt.25.4.425.
- [130] Sdringola S, Johnson NP, Kirkeeide RL, Cid E, Gould KL. Impact of Unexpected Factors on Quantitative Myocardial Perfusion and Coronary Flow Reserve in Young, Asymptomatic Volunteers. *JACC Cardiovasc Imaging* 2011;4:402–12. doi:10.1016/J.JCMG.2011.02.008.
- [131] Zarins CK, Taylor CA, Min JK. Computed fractional flow reserve (FFTCT) derived from coronary CT angiography. *J Cardiovasc Transl Res* 2013;6:708–14. doi:10.1007/s12265-013-9498-4.
- [132] Lortie M, Beanlands RSB, Yoshinaga K, Klein R, DaSilva JN, deKemp RA. Quantification of myocardial blood flow with ⁸²Rb dynamic PET imaging. *Eur J Nucl Med Mol Imaging* 2007;34:1765–74. doi:10.1007/s00259-007-0478-2.
- [133] Kassab GS. Scaling laws of vascular trees: of form and function. *Am J Physiol Heart Circ Physiol* 2006;290:H894–903. doi:10.1152/ajpheart.00579.2005.
- [134] Sankaran S, Kim HJ, Choi G, Taylor CA. Uncertainty quantification in coronary blood flow simulations: Impact of geometry, boundary conditions and blood viscosity. *J Biomech* 2016;49:2540–7. doi:10.1016/j.jbiomech.2016.01.002.

- [135] Sankaran S, Kim HJ, Choi G, Taylor CA. Uncertainty quantification in coronary blood flow simulations: Impact of geometry, boundary conditions and blood viscosity. *J Biomech* 2016;49:2540–7. doi:10.1016/J.JBIOMECH.2016.01.002.
- [136] Melikian N, De Bruyne B, Fearon WF, MacCarthy PA. The Pathophysiology and Clinical Course of the Normal Coronary Angina Syndrome (Cardiac Syndrome X). *Prog Cardiovasc Dis* 2008;50:294–310. doi:10.1016/j.pcad.2007.01.003.
- [137] Ford TJ, Rocchiccioli P, Good R, McEntegart M, Eteiba H, Watkins S, et al. Systemic microvascular dysfunction in microvascular and vasospastic angina. *Eur Heart J* 2018;39:4086–97. doi:10.1093/eurheartj/ehy529.
- [138] Sorop O, Merkus D, De Beer VJ, Houweling B, Pistea A, McFalls EO, et al. Functional and structural adaptations of coronary microvessels distal to a chronic coronary artery stenosis. *Circ Res* 2008;102:795–803. doi:10.1161/CIRCRESAHA.108.172528.
- [139] Heijne M, Raijmakers PG, Harms HJ, Lubberink M, Halbmeijer R, Appelman YE. Coronary steal : Revealing the diagnosis with quantitative cardiac PET / CT n.d. doi:10.1007/s12350-010-9265-8.
- [140] Gould KL. Coronary steal. Is it clinically important? *Chest* 1989;96:227–9. doi:10.1378/chest.96.2.227.
- [141] Takx RAP, Blomberg BA, Aidi H El, Habets J, De Jong PA, Nagel E, et al. Diagnostic Accuracy of Stress Myocardial Perfusion Imaging Compared to Invasive Coronary Angiography With Fractional Flow Reserve Meta-Analysis 2015:1–7. doi:10.1161/CIRCIMAGING.114.002666.
- [142] Coenen A, Rossi A, Lubbers MM, Kurata A, Kono AK, Chelu RG, et al. Integrating CT Myocardial Perfusion and CT-FFR in the Work-Up of Coronary Artery Disease. *JACC Cardiovasc Imaging* 2017;10:760–70. doi:10.1016/j.jcmg.2016.09.028.

- [143] Petraco R, Sen S, Nijjer S, Echavarría-Pinto M, Escaned J, Francis DP, et al. Fractional Flow Reserve–Guided Revascularization: Practical Implications of a Diagnostic Gray Zone and Measurement Variability on Clinical Decisions. *JACC Cardiovasc Interv* 2013;6:222–5. doi:10.1016/J.JCIN.2012.10.014.
- [144] Gould KL, Johnson NP. Coronary Physiology Beyond Coronary Flow Reserve in Microvascular Angina: JACC State-of-the-Art Review. *J Am Coll Cardiol* 2018;72:2642–62. doi:10.1016/j.jacc.2018.07.106.
- [145] Williams MC, Mirsadraee S, Dweck MR, Weir NW, Fletcher A, Lucatelli C, et al. Computed tomography myocardial perfusion vs 15O-water positron emission tomography and fractional flow reserve. *Eur Radiol* 2017;27:1114–24. doi:10.1007/s00330-016-4404-5.
- [146] Oliveira JB, Sen YM, Wechalekar K. Intersoftware variability impacts classification of cardiac PET exams. *J Nucl Cardiol* 2019;26:2007–12. doi:10.1007/s12350-018-1444-z.
- [147] Gould KL, Johnson NP, Bateman TM, Beanlands RS, Bengel FM, Bober R, et al. Anatomic versus physiologic assessment of coronary artery disease: Role of coronary flow reserve, fractional flow reserve, and positron emission tomography imaging in revascularization decision-making. *J Am Coll Cardiol* 2013;62:1639–53. doi:10.1016/j.jacc.2013.07.076.
- [148] Min JK, Taylor CA, Achenbach S, Koo BK, Leipsic J, Nørgaard BL, et al. Noninvasive fractional flow reserve derived from coronary CT angiography clinical data and scientific principles. *JACC Cardiovasc Imaging* 2015;8:1209–22. doi:10.1016/j.jcmg.2015.08.006.
- [149] Danad I, Raijmakers PG, Driessen RS, Leipsic J, Raju R, Naoum C, et al. Comparison of coronary CT angiography, SPECT, PET, and hybrid imaging for diagnosis of ischemic heart disease determined by fractional flow reserve. *JAMA Cardiol* 2017;2:1100–7. doi:10.1001/jamacardio.2017.2471.
- [150] Fearon WF, Aarnoudse W, Pijls NHJ, De Bruyne B, Balsam LB,

Cooke DT, et al. Microvascular resistance is not influenced by epicardial coronary artery stenosis severity: Experimental validation. *Circulation* 2004;109:2269–72.
doi:10.1161/01.CIR.0000128669.99355.CB.

- [151] George RT, Silva C, Cordeiro MAS, DiPaula A, Thompson DR, McCarthy WF, et al. Multidetector Computed Tomography Myocardial Perfusion Imaging During Adenosine Stress. *J Am Coll Cardiol* 2006;48:153–60. doi:10.1016/j.jacc.2006.04.014.
- [152] Ko B, Cameron J, Munnur R, Wong DTL, Fujisawa Y, Sakaguchi T, et al. Noninvasive CT-Derived FFR Based on Structural and Fluid Analysis. *JACC Cardiovasc Imaging* 2016.
doi:10.1016/j.jcmg.2016.07.005.
- [153] Galderisi M, Rigo F, Gherardi S, Cortigiani L, Santoro C, Sicari R, et al. The impact of aging and atherosclerotic risk factors on transthoracic coronary flow reserve in subjects with normal coronary angiography. *Cardiovasc Ultrasound* 2012;10:20. doi:10.1186/1476-7120-10-20.
- [154] Mygind ND, Michelsen MM, Pena A, Frestad D, Dose N, Aziz A, et al. Coronary microvascular function and cardiovascular risk factors in women with angina pectoris and no obstructive coronary artery disease: The iPOWER study. *J Am Heart Assoc* 2015;5.
doi:10.1161/JAHA.115.003064.
- [155] Nitenberg A, Ledoux S, Valensi P, Sachs R, Attali JR, Antony I. Impairment of coronary microvascular dilation in response to cold pressor-induced sympathetic stimulation in type 2 diabetic patients with abnormal stress thallium imaging. *Diabetes* 2001;50:1180–5.
doi:10.2337/diabetes.50.5.1180.
- [156] Nitenberg A, Valensi P, Sachs R, Dali M, Aptekar E, Attali JR. Impairment of coronary vascular reserve and ACh-induced coronary vasodilation in diabetic patients with angiographically normal coronary arteries and normal left ventricular systolic function. *Diabetes*

1993;42:1017–25. doi:10.2337/diab.42.7.1017.

- [157] Giugliano D, Marfella R, Coppola L, Verrazzo G, Acampora R, Giunta R, et al. Vascular effects of acute hyperglycemia in humans are reversed by L- arginine: Evidence for reduced availability of nitric oxide during hyperglycemia. *Circulation* 1997;95:1783–90. doi:10.1161/01.CIR.95.7.1783.
- [158] Williams SB, Cusco JA, Roddy MA, Johnstone MT, Creager MA. Impaired nitric oxide-mediated vasodilation in patients with non-insulin-dependent diabetes mellitus. *J Am Coll Cardiol* 1996;27:567–74. doi:10.1016/0735-1097(95)00522-6.
- [159] Johnstone MT, Creager SJ, Scales KM, Cusco JA, Lee BK, Creager MA. Impaired endothelium-dependent vasodilation in patients with insulin- dependent diabetes mellitus. *Circulation* 1993;88:2510–6. doi:10.1161/01.CIR.88.6.2510.
- [160] Ting HH, Timimi FK, Boles KS, Creager SJ, Ganz P, Creager MA. Vitamin C improves endothelium-dependent vasodilation in patients with non-insulin-dependent diabetes mellitus. *J Clin Invest* 1996;97:22–8. doi:10.1172/JCI118394.
- [161] McVeigh GE, Brennan GM, Johnston GD, McDermott BJ, McGrath LT, Henry WR, et al. Impaired endothelium-dependent and independent vasodilation in patients with Type 2 (non-insulin-dependent) diabetes mellitus. *Diabetologia* 1992;35:771–6. doi:10.1007/BF00429099.
- [162] Calver A, Collier J, Vallance P. Inhibition and stimulation of nitric oxide synthesis in the human forearm arterial bed of patients with insulin-dependent diabetes. *J Clin Invest* 1992;90:2548–54. doi:10.1172/JCI116149.
- [163] Rooks C, Faber T, Votaw J, Veledar E, Goldberg J, Raggi P, et al. Effects of smoking on coronary microcirculatory function: A twin study. *Atherosclerosis* 2011;215:500–6. doi:10.1016/j.atherosclerosis.2011.01.012.

- [164] Aune E, Røislien J, Mathisen M, Thelle DS, Otterstad JE. The “smoker’s paradox” in patients with acute coronary syndrome: A systematic review. *BMC Med* 2011;9:97. doi:10.1186/1741-7015-9-97.
- [165] Gourlay SG, Rundle AC, Barron H V. Smoking and mortality following acute myocardial infarction: results from the National Registry of Myocardial Infarction 2 (NRM1 2). *Nicotine Tob Res* 2002;4:101–7. doi:10.1080/14622200110103205.
- [166] Kunz F, Pechlaner C, Hörtnagl H, Pfister R. The smoker’s paradox and the real risk of smoking. *Eur J Epidemiol* 2005;20:161–7. doi:10.1007/s10654-004-3004-x.
- [167] Barua RS, Ambrose JA. Mechanisms of coronary thrombosis in cigarette smoke exposure. *Arterioscler Thromb Vasc Biol* 2013;33:1460–7. doi:10.1161/ATVBAHA.112.300154.
- [168] Doi SA, Islam N, Sulaiman K, Alsheikh-Ali AA, Singh R, Al-Qahtani A, et al. Demystifying Smoker’s Paradox: A Propensity Score–Weighted Analysis in Patients Hospitalized With Acute Heart Failure. *J Am Heart Assoc* 2019;8. doi:10.1161/JAHA.119.013056.
- [169] Del Bo’ C, Campolo J, Porrini M, Fracassetti D, Parolini M, Klimis-Zacas D, et al. Acute cigarette smoking impairs microvascular function in young moderate smokers: A potential model for studying vasoactive properties of food bioactives. *PharmaNutrition* 2014;2:1–7. doi:10.1016/j.phanu.2013.07.001.
- [170] Gullu H, Caliskan M, Ciftci O, Erdogan D, Topcu S, Yildirim E, et al. Light cigarette smoking impairs coronary microvascular functions as severely as smoking regular cigarettes. *Heart* 2007;93:1274–7. doi:10.1136/hrt.2006.100255.
- [171] Galderisi M, de Simone G, Cicala S, Parisi M, D’Errico A, Innelli P, et al. Coronary Flow Reserve in Hypertensive Patients With Hypercholesterolemia and Without Coronary Heart Disease. *Am J Hypertens* 2007;20:177–83. doi:10.1016/j.amjhyper.2006.06.017.

- [172] Koo BK, Erglis A, Doh JH, Daniels D V., Jegere S, Kim HS, et al. Diagnosis of ischemia-causing coronary stenoses by noninvasive fractional flow reserve computed from coronary computed tomographic angiograms: Results from the prospective multicenter DISCOVER-FLOW (Diagnosis of Ischemia-Causing Stenoses Obtained Via Noninvasive Fractional Flow Reserve) study. *J Am Coll Cardiol* 2011;58:1989–97. doi:10.1016/j.jacc.2011.06.066.
- [173] Min JK, Leipsic J, Pencina MJ, Berman DS, Koo BK, Van Mieghem C, et al. Diagnostic accuracy of fractional flow reserve from anatomic CT angiography. *JAMA - J Am Med Assoc* 2012;308:1237–45. doi:10.1001/2012.jama.11274.
- [174] Gould KL. Does Coronary Flow Trump Coronary Anatomy? *JACC Cardiovasc Imaging* 2009;2:1009–23. doi:10.1016/J.JCMG.2009.06.004.
- [175] Berry C, van 't Veer M, Witt N, Kala P, Bocek O, Pyxaras SA, et al. VERIFY (VERification of Instantaneous Wave-Free Ratio and Fractional Flow Reserve for the Assessment of Coronary Artery Stenosis Severity in EverydaY Practice): A Multicenter Study in Consecutive Patients. *J Am Coll Cardiol* 2013;61:1421–7. doi:10.1016/J.JACC.2012.09.065.
- [176] Johnson NP, Johnson DT, Kirkeeide RL, Berry C, De Bruyne B, Fearon WF, et al. Repeatability of Fractional Flow Reserve Despite Variations in Systemic and Coronary Hemodynamics. *JACC Cardiovasc Interv* 2015;8:1018–27. doi:10.1016/j.jcin.2015.01.039.
- [177] Sen S, Nijjer S, Petraco R, Malik IS, Francis DP, Davies J. Instantaneous Wave-Free Ratio. *J Am Coll Cardiol* 2013;62:566. doi:10.1016/j.jacc.2013.03.076.
- [178] Nijjer SS, Dewaard GA, Sen S, Van De Hoef TP, Petraco R, Echavarría-Pinto M, et al. Coronary pressure and flow relationships in humans: Phasic analysis of normal and pathological vessels and the implications for stenosis assessment: A report from the Iberian-Dutch-

English (IDEAL) collaborators. *Eur Heart J* 2016;37.
doi:10.1093/eurheartj/ehv626.

- [179] Blanco PJ, Bulant CA, Müller LO, Talou GDM, Bezerra CG, Lemos PL, et al. Comparison of 1D and 3D Models for the Estimation of Fractional Flow Reserve. *Sci Rep* 2018;8:17275. doi:10.1038/s41598-018-35344-0.
- [180] Moss AJ, Williams MC, Newby DE, Nicol ED. The Updated NICE Guidelines: Cardiac CT as the First-Line Test for Coronary Artery Disease. *Curr Cardiovasc Imaging Rep* 2017;10. doi:10.1007/s12410-017-9412-6.
- [181] Pugliese F. MBF From Dynamic CT Perfusion Imaging - American College of Cardiology n.d. <https://www.acc.org/latest-in-cardiology/articles/2019/04/26/09/46/mbf-from-dynamic-ct-perfusion-imaging> (accessed June 8, 2021).